Nanostructure modelling for nanocomposite materials

By

Matthew Tolladay

A dissertation submitted to the University of Bristol in accordance with the requirements for award of the degree of Doctor of Philosophy in the Faculty of Engineering.

Word count: 41000 (Approx.)

Abstract

Calculating mechanical properties of structures at the nanoscale is a problematic task. Different methods exist for performing the calculations but there is always a trade off between speed and accuracy. This work explores a number of different methods for simulating nanostructures. First, it describes a novel extension to an atomistic finite element method to enable it to perform calculations of the piezoelectric properties of nanostructures. The results are then compared with those from molecular mechanics methods. Next it benchmarks various reactive molecular mechanics potentials and electronic structure methods as tools for predicting the tensile strengths and strains at failure of carbon-carbon bonds. The third-order density-functional tight-binding method (DFTB3) and the adaptive intermolecular reactive empirical bond order potential (AIREBO) are shown to offer the best accuracy while still being computationally cheap enough to model nanostructures. Finally, the two most successful methods from the previous section, DFTB3 and AIREBO, are applied to a selection of nanoribbons undergoing uniaxial tensile strain to the point of failure. The importance of the electronic structure to the mechanical properties is examined and a previously unseen relationship between the tensile modulus of armchair nanoribbons and their nanoribbon index is revealed. Additionally, calculations of the tensile properties of experimentally derived nanoribbons are performed that show cove-types nanoribbons to have excellent mechanical properties.

Dedication and Acknowledgements

I would like to acknowledge a number of people who helped with this work at one point or another: Neil Allan for providing guidance through the complicated world of computational chemistry. Fabrizio Scarpa for general advice, encouragement and help in getting all of this work done. Dmitry Ivanov for the very useful and insightful feedback on this work. Peter Bygrave for useful advice about coding techniques. Alex Buccheri for useful advice and discussions about non-orthogonal tight-binding methods and DFTB+. Alberto Pirrera for providing help with understanding the finite element method. Chris Tothill for providing useful tricks and tips for getting the most out the computational chemistry centre's clusters. I would also like to thank: Natalie Fey, Fred Manby, Paul Weaver, Rob Iredale, Alexis Kordolemis, Chrysoula Aza, Max Dixon, Rhys Tapper and Sarah Hallworth. I would also like to thank my family, particularly my mother and father for supporting me during my undergraduate years. Finally I would like to thank my partner Laura for providing endless patience, love and care throughout this process.

Author's declaration

I declare that the work in this dissertation was carried out in accordance with the requirements of the University's Regulations and Code of Practice for Research Degree Programmes and that it has not been submitted for any other academic award. Except where indicated by specific reference in the text, the work is the candidate's own work. Work done in collaboration with, or with the assistance of, others, is indicated as such. Any views expressed in the dissertation are those of the author.

SIGNED: ..... DATE:.....

Contents

List of Figures

List of Tables

Research output

Conference papers

Predicting piezoelectric effects in atomistic finite element simulations. Mat Tolladay, Fabrizio Scarpa, Dmitry Ivanov and Neil Allan, *24th International Congress of Theoretical and Applied Mechanics, ICTAM2016*, Montreal, August 22-26, 2016.
Atomistic modelling of hydrocarbon nanostructure failure. Mat Tolladay, Neil L. Allan, Dmitry Ivanov and Fabrizio Scarpa, *EUROMECH Colloquium 603: Dynamics of micro and nano systems*, Porto, Portugal, September 5-7, 2018.

Journal publications

Piezoelectric effects in boron nitride nanotubes predicted by atomistic finite element method and molecular mechanics. Mat Tolladay, Dmitry Ivanov, Neil Allan, and Fabrizio Scarpa, *Nanotechnology*, 28(35):355705, 2017.

Preface

This thesis examines various methods for modelling the mechanical behaviours of nanostructures. These methods have been developed by chemists and physicists for calculating various properties of small molecules or infinite crystals. However, as technology becomes smaller it is becoming feasible to design structures at the nanoscale which is drawing in engineers to this atomic scale world. At this lengthscale the traditional structural engineering approach of continuum mechanics is much harder to apply and in many instances it makes more sense to consider the discreet atoms directly. The interactions between atoms are responsible for many macroscopic material properties but are themselves caused by the interactions of sub-atomic particles. At the sub-atomic level it is necessary to consider the behaviour of electrons interacting with the positively charged atomic nuclei which requires the use of quantum mechanics. This thesis provides an overview of different methods for modelling matter at the atomic scale and applies these methods to various nanostructures.

The techniques used in this work have existed since the mid twentieth century and have been developed and used by chemists and physicists for investigating chemical processes and solid state electronics. These methods are a mature technology and are widely accepted within these communities but it is important to recognise that there is often an implicit understanding of their limitations. The work presented here provides insight into some of these issues and highlights how incorrect results can be obtained from calculation schemes which appear to be capable of modelling all the required physics. Chapter 3 introduces a method called atomistic finite element method and explains its similarities and differences from conventional molecular mechanics methods. The conclusion of that work questions whether the atomistic finite element method really provides anything of value over the conventional approach. In chapter 4 the ability of different calculation schemes to reliably investigate bond breaking events, which are relevant to understanding catastrophic failure at the atomic scale, are studied. The work shows that the complexity of such events makes it difficult to simulate even when including the quantum mechanical behaviour of electrons in the calculations. Chapter 5 shows that calculations of the tensile moduli, which is much easier to investigate theoretically than tensile strength, of carbon nanoribbons benefit from including quantum mechanics in the calculations. At that level of theory a pattern emerges in the moduli of the ribbons, when increasing the ribbon

width, which is not seen when using simpler models.
This thesis includes some of the mathematical theory that underlies the methods that it uses, but it may be worth considering reading some books for a more detailed understanding. The book "Quantum physics of atoms, molecules, solids, nuclei and particles" by Eisberg and Resnick [1] provides a useful introduction to quantum mechanics as does "Quantum Mechanics" by Rae [2]. The book "Modern Quantum Chemistry: introduction to advanced electronic structure theory" by Szabo and Ostlund [3] provides a detailed overview of how quantum mechanics can be applied to the problem of electrons in molecules and is highly recommended. For a more general overview of molecular modelling there is "Molecular Modelling: Principles and Applications" by Leach [4] and "Introduction to Computational Chemistry" by Jensen [5]. There are many more books that cover these topics but those listed above are strongly recommended by the author who found them extremely useful in producing this work.
The most important message this thesis can convey is the need for care when performing atomistic calculations. There are many different calculation schemes available which vary in complexity in both the underlying theory and the computational implementation. At one end these calculations can be rapidly performed on a desktop computer and at the other it can take days of walltime on a powerful cluster. It is always necessary to try to validate a method before using it, which can be very challenging, and to check to see if there is a more appropriate calculation method available. It is hoped that this document will help shine a light on some of these issues and make it easier for others to apply these methods to simulations of nanostructures.

Bibliography

[1] R. M. Eisberg, R. M. Eisberg, and R. M. Eisberg. *Quantum physics of atoms, molecules, solids, nuclei, and.* Wiley, New York, 1985.

[2] A. Rae. *Quantum mechanics.* Taylor & Francis Group, 2008.

[3] A. Szabo and N. S. Ostlund. *Modern Quantum Chemistry: introduction to advanced electronic structure theory.* Dover Publications, Inc., 1989.

[4] A. Leach. *Molecular Modelling: Principles and Applications.* Prentice Hall, 2001.

[5] F. Jensen. *Introduction to Computational Chemistry.* Wiley, 2016.

Chapter 1

Introduction

Computer simulations of materials allow the prediction of properties and behaviour that would otherwise be inaccessible. These tools have been developed over decades and across many disciplines in order to make predictions based on known physics. They are used across lengthscales to understand everything from the airflow around an aeroplane wing to chemical reactions in the human body. They can be used to determine the accuracy of theory compared with experimental results by numerically solving otherwise unsolvable equations. However, they are always limited by underlying assumptions and approximations. This work investigates simulation methods for probing the behaviour of nanostructures. The lengthscales of interest for this task are between those which can be comfortably modelled using most standard methods.

The development of nanostructures has seen significant growth over the last thirty years. In the 1980s much effort was applied to synthesising carbon nanostructures and succeeded with the production of Buckminster fullerenes [1]. In the early 1990s carbon nanotubes (CNTs) were produced [2], an intriguing form of carbon for which potential applications are still being investigated. During this period scientists starting looking for new structures to synthesise, including those made of elements other than carbon, but in many cases these materials were first investigated numerically using modelling techniques developed for theoretical chemistry. The search for new nanostructures has been led by theoretical predictions and many potential structures with interesting and useful properties have been investigated.

Despite the vast array of nanostructures that have been discovered and synthesised there are still few applications for these materials. One of the earliest suggested applications for CNTs was to use them as reinforcement in polymers to improve the polymer's mechanical properties. Carbon fibre reinforced polymers had demonstrated that it was possible to achieve considerable weight savings over metal alloys using carbon based composite materials. The greater strength and stiffness of carbon nanotubes compared to carbon fibres suggested that CNT reinforced polymers could prove to have even better performance. However, using CNTs for this purpose created new problems, limiting their usability in

composite materials. Carbon nanotubes propensity to stick to each other through van der Waals forces and to become entangled with each other makes it difficult to disperse them in a polymer resin or melt. This limits the concentration of CNTs that can be mixed into a polymer [3] which in turn limits the improvement in the mechanical properties compared with the pure polymer.

Research on the use of CNTs for composite materials continues but mostly to fulfil specific roles within carbon fibre reinforced polymers. One such role uses CNTs to improve the interlaminar shear strength of carbon fibre laminates by growing them directly on microscale fibres [4]. Another uses aligned CNTs between layers of carbon fibres to improve the interlaminar toughness [5]. Magnetically aligned functionalised CNTs may be used to provide aligned fibre repair patches on damaged carbon fibre structures [6]. There is still much work to be done for these applications to reach commercial viability and there are still efforts being made to improve CNT reinforced polymers.

The next big discovery in the field of nanomaterials was the synthesis of graphene, a two dimensional lattice of carbon atoms [7]. This material not only displays the high strength and stiffness associated with other carbon based materials but it also possesses interesting electrical properties. However, the major problem in using graphene in electrical components is its lack of a band gap. One method for inducing a band gap in graphene is to create narrow channels made of graphene either through additive functionalisation or by forming narrow graphene strips. The second of these options gave rise to another family of nanostructures referred to as nanoribbons. The properties and behaviour of graphene nanoribbons (GNRs) were examined theoretically prior to the first synthesis of graphene [8]. GNRs have been produced using bottom up synthesis methods [9] which has led to an increasing variety of GNRs, with different GNRs distinguished by their edge shapes. These nanostructures have considerable potential for use in nanocomposites.

The growing range of nanostructures have unique physical properties. It is the purpose of the work here to explore different methods for characterising such properties and to apply them to specific materials. This chapter starts by introducing some important theories relating to polycyclic aromatic hydrocarbons which are applicable to carbon nanotubes and graphene nanoribbons. It then introduces the main computational methods that have been used both historically and in the work presented here. Then there is a brief history of carbon nanotubes, boron nitride nanotubes and graphene nanoribbons and a review of experimental and theoretical investigations of these materials. Finally, there is a review of the development of nanocomposite materials, which are the motivation for the work presented here, and then conclusions and an overview of the structure of this thesis .

Figure 1.1: The two equivalent Kekulé structures of benzene. The structure of benzene was predicted to be a based on a mixture of these two equivalent diagrams.

1.1 Polycyclic aromatic hydrocarbon chemistry

Polycyclic aromatic hydrocarbons (PAHs) are molecules made of hydrogen and carbon atoms containing aromatic rings of carbon atoms. This family of materials include a wide variety of materials with very different behaviours. They can be small molecules such as anthracene or nanomaterials such as carbon nanotubes, graphene or graphene nanoribbons. The most basic aromatic hydrocarbon is benzene whose structure was of great interest to chemists in the nineteenth century (see figure 1.1). The arrangement of its bonds would be a matter of debate for some time and would help inspire one of the most well recognised chemical notations: Kekulé structures. These diagrams allow chemists to understand the structure and chemistry of PAHs and the broader family of organic chemicals containing carbon, nitrogen, oxygen and hydrogen. Kekulé suggested that benzene should be considered as a combination of two structures both containing six carbon atoms in a ring connected with alternating single and double bonds [10]. The explanation for this type of structure would require the development of quantum mechanical theories of molecular bonding and would give rise to the idea of aromatic bonding [11]. Hückel would build on this idea and use it to explain the underlying mechanism of the relative stability of benzene. Later attempts to expand Hückel's $4n+2$ rule from monocyclic benzene to polycyclic hydrocarbons would yield Clar's rule [12]. Clar's rule states that the structure that allows for the greatest number of π-sextet aromatic rings is the most stable electronic configuration. It is this structure that will determine the behaviour of the polycyclic aromatic hydrocarbon molecule.

The basic method for applying Clar's method for graphing a PAH is to draw the maximum number of circles, representing π-sextets, in all non-adjacent benzene rings so that any bonds not involved in these π-sextets can be modified to complete the Kekulé structure. The method for constructing these diagrams is shown in figure 1.2. This method allows the easy classification of different types of PAH structures based on the possible types of Clar diagrams. First there are fully benzenoid structures which only contain π-sextets or 'empty' rings, see figure 1.3(a). Second there are structures that are completed by adding one additional double bond to the Kekulé structure, see figure 1.3(b). Finally, there are structures that can only be completed by adding more than one double bond in which case multiple Clar diagrams can be drawn for the same molecule which all contain the same number of π-sextet rings, see figure 1.3(c).

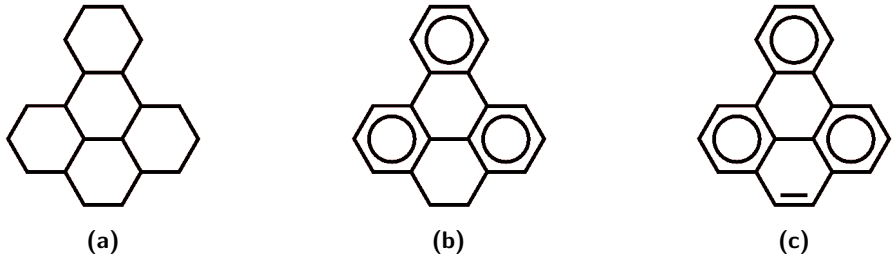

Figure 1.2: The three diagrams show the process of constructing Clar diagrams for PAHs. Figure (a) shows the basic structure of the molecule. Figure (b) shows the maximum number of non-adjacent π-sextet rings filled in and figure (c) shows the completed Kekulé strcuture containing one double bond.

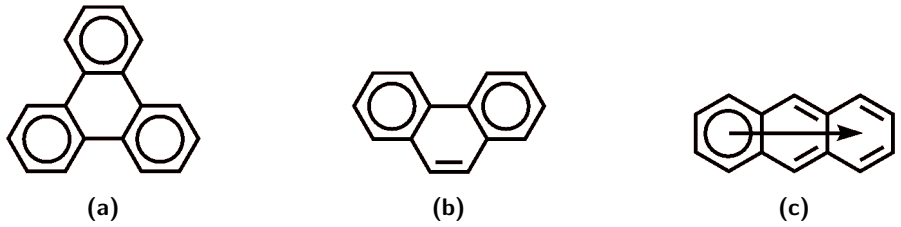

Figure 1.3: The three diagrams show the different types of Clar structures and rings. Figure (a) shows a fully benzenoid structure (triphenylene) with rings with circles indicating π-sextets and 'empty' rings. Figure (b) shows a structure completed by the addition of one double bond (phenanthrene) and (c) shows a molecule containing multiple double bonds and a migratory π-sextet ring (anthracene).

The chemical significance of these diagrams lies in the number and position of the double bonds. When the structure is fully benzenoid there are no double bonds and the chemical will possess an additional stability which leads to an almost inert character. The stability of fully benzenoid structures can be seen in the relatively large size of their molecular orbital gaps [13]. When a single double bond is present the sites at either end of that bond will be the most reactive. This preserves the highest possible number of π-sextets which ensures the greatest possible stability of the molecule. If more than one double bond is present any additive reaction with the molecule favours the sites that create a product with the maximum number of π-sextets.

Clar's rule is useful for determining the properties of both molecular and periodic structures. It has been used to explain the trends in band gaps of graphene nanoribbons [14] and finite length carbon nanotubes [15]. It has also been used to help design zig-zag nanoribbons with specific band gaps by altering their edge chemistry [16]. However, there are other useful methods for analysing PAH structures. One very simple graph theory is Lieb's theorem [17] which allows for the determination of the number of unpaired electrons in a PAH. Polycyclic aromatic hydrocarbon structures contain carbon atoms that can be thought of as lying on one of two interpenetrating equilateral triangular sublattices. This is shown graphically in figure 1.4. Lieb's theorem states that the

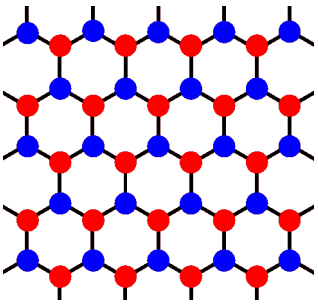

Figure 1.4: A section of graphene with the two interpenetrating triangular sublattices indicated by the blue and red circles.

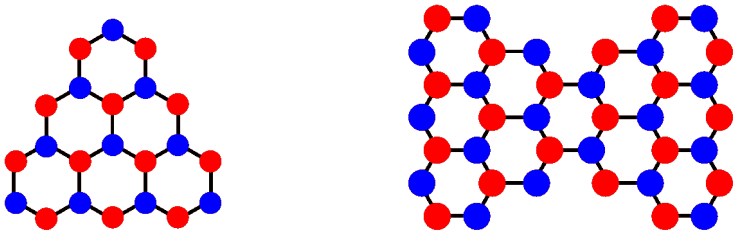

Figure 1.5: Figure (a) shows the structure of triangulene and (b) the structure of Clar's Goblet. The red and blue dots indicate whether the sub-lattice site belongs to sublattice A or sublattice B.

total unpaired spin for a PAH is

$$S = \frac{1}{2} \left| N_{\mathrm{A}} - N_{\mathrm{B}} \right|, \tag{1.1}$$

where N_{A} and N_{B} are the number of occupied lattice sites for sublattice A and B respectively. This very simple rule is extremely useful for determining whether a PAH possess a radical character or, when considering periodic structure, its magnetic properties.
Benzenoid graph theory was further extended by showing that the number of electron states at the Fermi level can be determined from the maximum number of disconnected atoms [18, 19]. This theory determines the number of states at the Fermi level using

$$\nu = 2\alpha - N, \tag{1.2}$$

where ν is the number of states at the Fermi level, α is the maximum number of disconnected lattice sites and N is the total number of sites. These two rules can be applied to all types of PAHs to determine their spin behaviour. Two useful examples of this are the so-called triangulene and Clar's goblet molecules shown in figure 1.5. For triangulene the difference of the number of sites belonging to the two sublattices is 2 which is also the number of states at the Fermi level. The triangular molecule possesses two spin-aligned unpaired electrons and a radical character. Clar's goblet however has the same number of sites belonging to both sublattices but the graph theory predicts two states at the Fermi

level. The only way to satisfy these two rules is for the molecule to be a diradical with the two electrons possesing anti-parallel spins [20]. These rules have been used as a simple tool for designing carbon based spintronic logic gates [21, 22] and magnetic materials [23]. However, these radical PAHs are highly unlikely to be seen experimentally as they are usually highly reactive.

1.2 Theoretical methods of investigation

Most properties of nanostructure are determined using theoretical models. It is extremely challenging to measure properties of structures that are only a few nanometres or even Angstroms wide experimentally. The first issue is finding a way to manipulate the structure without damaging or altering it prior to the experiment. The second issue is finding ways to interact with the structure in a controlled and measurable way.
Nevertheless, the availability of nanotubes of lengths in the region of millimetres has allowed for some experimental characterisation of their properties. The relatively long lengths make it somewhat easier to perform experiments where clamps or electrical contacts need to be applied to the nanotube. This has allowed investigations of their electrical [24] and mechanical [25] properties. Atomically precise nanoribbons have been developed but have only been available for less than eight years and have dimensions significantly smaller than nanotubes. Their lengths are generally only a few tens of nanometers, their widths a few Angstroms and they are only a single atom thick.
There are three main methods used for modelling nanostructures: molecular mechanics potentials, tight-binding methods and full electronic structure calculations. Molecular mechanics potentials are computationally cheapest and can therefore be used to model larger structures. They cannot be used to simulate the electronic and magnetic behaviour of nanostructures and the predictions of mechanical properties are somewhat approximate. Tight-binding methods have been very popular for carbon based nanostructures and can provide insight into electronic, magnetic and mechanical properties. They are more computationally demanding than molecular mechanics methods and the accuracy of such calculations vary depending on the method and parameters used. Full electronic structure calculations are *ab initio* and performed using a variety of different methods. These calculations can be used to provide the most accurate predictions of nanomaterial properties.
Molecular mechanics methods are a very common technique for investigating the mechanical properties of nanostructures. Their computational efficiency permits the simulation of structures designed for specific tasks such as graphene filter membranes [26, 27] or engineered kirigami structures [28] where it becomes necessary to model thousands of atoms. Most potentials for carbon and organic chemistry rely on the types and arrangement of the molecular bonds to be input by the user prior to the calculation being performed. This is so that specific parameters can be used for bonds connecting different types of

atom with different bond orders. It is common to use harmonic potentials to describe certain interactions but such potentials are only able to describe interactions close to equilibrium bond lengths and angles. The most popular family of molecular mechanics potentials for modelling carbon based structures is the Tersoff-Brenner reactive empirical bond order potentials [29, 30]. These were developed specifically for the purpose of simulating carbon structures and were developed from a potential designed to model solid state phase changes of materials. One benefit is that they can model bond scission and can therefore be used to simulate nanostructure failure and calculate the strengths of nanostructures. However, the behaviour and values predicted by these potentials are based on significant simplification of the underlying physics so may be inaccurate.

Tight-binding methods offer more insight into nanostructure behaviour. Most tight-binding methods limit interactions to nearest atomic neighbours, although this is not always the case [31], which keeps the computational cost low. This is the root of the term 'tight-binding' as the electrons are considered to remain tightly bound to their parent nuclei. The relationship between tight-binding and hydrocarbon molecules can be traced back to Hückel theory in the 1930's [32]. These methods rely on parameters, determined by experiment or more accurate calculation methods, to avoid having to compute various integrals that are required by most electronic structure calculations. This also helps keep computational costs low and allows structures containing several thousand atoms to be modelled efficiently. The method can be used to predict electronic structure properties such as band gaps and dispersion curves but they are known to be somewhat inaccurate.

Full electronic structure methods are capable of more accurate calculations of properties than tight-binding methods. They scale fairly poorly with system size such that the most efficient methods can only deal with systems containing a few hundred atoms. There are a variety of different calculation schemes available which can reliably predict properties of interest. However, computing accurate quantitative values for some properties can require methods that can only be applied to a dozen or so atoms. The most popular method is density-functional theory (DFT) which itself can be broken down into a number of sub-methods based on different exchange-correlation functionals and basis sets. This method has at best computational scaling of N^3, where N is the number of basis functions, and can reliably predict molecular geometries. It is generally reliable for predicting quantities such as energy barriers but will often underestimate electronic band gaps [33]. Despite its imperfections it is relied upon to provide at least qualitative descriptions of various trends and behaviours. It can also be readily extended to periodic systems making it very useful for calculations of bulk quantities. More computationally intensive methods such as Møller-Plesset perturbation theory [34], coupled-cluster theory [35], configuration interaction [36] and multiconfiguration methods [37] are capable of producing quantitatively accurate results in a reliable manner. However, these scale at N^5 and higher so are only applicable to small molecules.

Mechanical simulations of larger nanostructures are mostly performed with molecular

mechanics potentials but it is possible to apply tight-binding methods for some structures. Density functional theory is often used to calculate mechanical properties of periodic systems and is often used as a benchmark for comparing results from potential based methods. Electronic properties for larger structures can only be calculated using tight-binding methods but small periodic systems, again, can be studied with DFT.

1.3 Nanotubes

The discovery of Buckminster fullerenes [1], spherical carbon allotropes, in 1985 helped drive the search for new forms of carbon. The next major discovery would be carbon nanotubes (CNTs), a structure consisting of rolled up sheet of graphene with its edges connected together [2]. These cylindrical structures have been widely investigated for both their electronic and mechanical properties. Mechanically they have been shown to be stronger than conventional carbon fibres while at the same time highly flexible. Their high aspect ratios have made them extremely appealing for use in nanocomposites. They were initially produced using the arc discharge method [2]. This involves passing a direct current across a gap between two graphite electrodes in a suitably inert gas. The electric discharge method produces multi-walled CNTSs (MWCNTs) which consist of a series of nanotubes of decreasing radius concentrically packed inside the largest CNT shell. Addition of metal catalyst particles has been used to produced single-walled CNTs (SWCNTs) which consist of a single cylinder of carbon atoms [38]. Coiled carbon nanotubes have also been produced [39]. These structures consist of carbon nanotubes containing 5-7 ring defects which generate the curvature of the coil. Different methods for synthesising carbon nanotubes have since been developed allowing for aligned CNTs to be produced [40].

Nanotube geometries vary not just in the number of walls involved but also by the alignment of the hexagonal lattice to the nanotube axis. Possible nanotube geometries are described by two indices given in the form (m, n). These indices are multipliers for the primitive lattice vectors of the hexagonal lattice of the material. The vector described by this index indicates the cutting direction for the ends of the nanotube as shown in figure 1.6. The two most important directions occur in the $(m, 0)$ and (n, n) directions which describe the zig-zag and armchair directions in the lattice. The vectors for these directions are at 30° to each other and represent the bounds for mirror and rotational symmetry for the lattice. The electrical properties of the CNT vary according to this chirality with armchair CNTs possessing metallic behaviour but for other indicies metallic behaviour is only observed when

$$\frac{2m+n}{3} = N, \quad \text{where} \quad N = 1, 2, 3, \ldots. \tag{1.3}$$

The band gaps of CNTs decrease as a function of the inverse of the nanotube diameter.

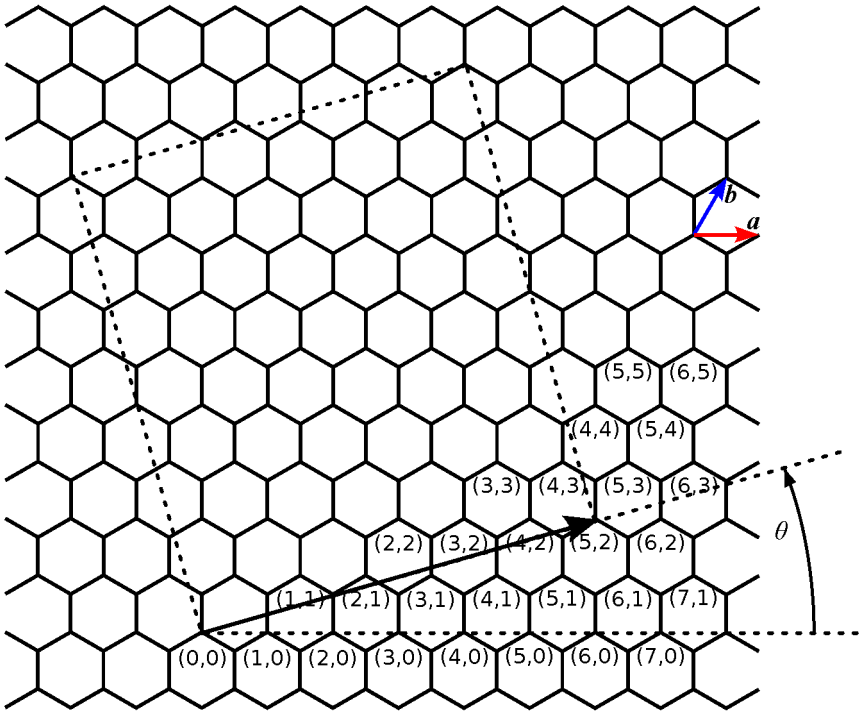

Figure 1.6: The figure shows the index system for nanotubes. The primitive lattice vectors are shown as the small red and blue arrows marked $\boldsymbol{a}$ and $\boldsymbol{b}$ respectively. The indices for different nanotubes are shown in brackets under the appropriate atoms. The cutting lines for a $(5, 2)$ nanotube are indicated and the resulting chiral angle theta is shown.

The behaviour of nanotubes should tend towards that of graphene as their diameter tends to infinity. The mechanical properties of nanotubes show no obvious dependence of the chirality [41] or radius [42].

Other materials

After the discovery of CNTs the possibility of nanotubes comprised of other materials was investigated. An obvious candidate was boron nitride [43] as it shares similar structures to carbon polymorphs, namely hexagonal-planar (graphite) and cubic forms (diamond). Multi-walled boron nitride nanotubes (BNNTs) were successfully synthesised shortly after this predication was made [44]. These nanotubes posses slightly different geometries to CNTs, forming a wrinkled instead of smooth tube wall, and they also possess a piezoelectric coupling. Nanotubes made of mixtures of boron nitride and carbon have also been reported [45, 46].

Another type of cylindircal nanostructure, which was synthesised prior to BNNTs, is tungsten disulphide nanotubes [47]. Tungsten disulphide also forms a hexagonal lattice but unlike graphite layers it is far from planar. A somewhat different approach has been used to produce silicon and titanium dioxide nanotubes [48, 49]. These have been prepared by coating a nanotube or nanofibre scaffold which is than removed chemically. A similar process has been reported for producing gallium nitride nanotubes using chemical

vapour deposition to coat zinc oxide nanowires which are then vaporised through the application of heat [50]. Molybdenum disulfide nanotubes have been synthesised using a catalysed transport method to grow the tubes onto a substrate [51]. This method is capable of producing single-walled molybdenum disulfide nanotubes. Phosphorene, a single layer of black phosphorous, has been proposed as has molybdenum ditelluride as potentially capable of forming nanotubes [52, 53] although they have not yet been synthesised.

The candidate materials for nanotube production all share a common trait with carbon in that they all possess a layered isomorph structure. Nanotubes can be considered as a single layer of material that has been rolled up so that its edges connect. The effect of increasing the tube diameter is to change from a nanotube geometry to a single planar layer of material. The discovery of carbon nanotubes served to accelerate efforts to isolate single layers of graphite.

Properties of nanotubes

The electrical and mechanical properties of nanotubes have been studied in depth over the last 25 years. Nanotubes can be formed with different chiralities and this leads to different electrical and mechanical properties. Tight-binding calculations have shown that armchair CNTs, with indices (n, n), are always metallic but zig-zag CNTs, with indices $(n, 0)$, are only metallic when n is a multiple of three [54]. Intermediate chiral CNTs, those with index (n, m), are metallic when $(3m + n)/3$ is integral. These results are for infinitely long nanotube models but when finite length is introduced different electrical behaviour occurs [15]. The finite lengths lengths used to investigate this effect were on the order of a few nanometres which is several orders of magnitude shorter than the length of commercially available nanotubes. The metallic nature of CNTs is seen as a benefit when using them as reinforcement in polymers because it improves the conductivity of the resulting composite compared with the pure polymer.

The mechanical properties of carbon nanotubes have also been the subject of investigations [55, 56, 57] that predicted the tensile axial modulus of CNTs to be about 1 TPa [55] and the bulk modulus to be about 9 GPa [57]. One issue with calculating such properties is the ill-defined nature of the nanotube wall thickness. In many cases, including the values cited above, this is taken as the interlaminar spacing of with graphite (3.35 Å) or the inter-wall spacing of MWCNTs (3.4 Å). In one study the wall thickness was calculated based on the extent of the π-electron orbitals of the carbon atoms leading to a value of 0.66 Å for the wall thickness and 5.5 TPa for the tensile modulus [58]. However, this value can be recalculated using a more common value for wall thickness and be shown to be in reasonable agreement with other calculated values, i.e. about 1 TPa. [55, 59, 42, 60, 41]. The calculated values are similar to the values determined through experiment [25, 61, 62]. Experimental values for the Young's modulus of nanotubes have been determined using atomic force microscopy (AFM) to measure the force and deflection of cantilevered

CNTs [62] or by investigating thermal vibrational properties using a transmission electron microscope [25, 61]. Measured quantities are then combined using standard cantilever beam models for hollow cylindrical beams to obtain values for the modulus. These results often show a considerable spread of values which is likely to be due to the quantity and distribution of defects in the nanotube structures [62].
Boron nitride nanotubes have also been subject to various theoretical and experimental studies. The first prediction of their properties, which occurred before they had been synthesised, was that they were insulators with a band gap greater than 2 eV [43]. Experimental determination of the Young's modulus of BNNTs was performed using the same techniques as described above for CNTs. Measurement of their thermally excited vibrations predicted Young's modulus values of 1.2 TPa, similar to those of CNTs [63]. Some results obtained using AFM have lower values than this, about 0.6 TPa [64], although other AFM studies have contradicted these results [65].
Theoretical values for the Young's modulus of BNNTs are between 0.7 TPa and 1 TPa. Tight-binding and density-functional theory calculations predict values in the range $0.76-0.91$ TPa [42, 66] which is in reasonable agreement with experiment. These are calculated using defect free structures for single-walled nanotubes. Higher values have been calculated using molecular mechanics force fields and are in the range $0.67-1.14$ TPa [67, 68]. However, the potentials and their parameters for these systems are not as widely accepted as those used for carbon based structures [69, 70].
Boron nitride nanotubes have an additional interesting feature that was first predicted through theoretical calculations: they are piezoelectric [71]. This property is dependent on the nanotube chirality and the type of applied loading [72]. The piezoelectric coefficient was found to be about 0.1 e/a_0 or about 0.7 C/m^2 in S.I. units, using a nanotube wall thickness of 3.4 Å [72, 73].

1.4 Nanoribbons

Graphene nanoribbons are single layers of graphene with a very high aspect ratio. Their properties have been studied theoretically since before the first reported isolation of graphene [8]. These studies have highlighted the importance of the edge shape and the effect of ribbon width on their electrical properties [74]. Attempts to construct graphene nanoribbons were made almost as soon as viable methods for the synthesis of graphene were found [75]. However, the theoretical electrical properties were dependent on the ribbons edge shape which was not possible to control using top-down nanoribbon production techniques.
Graphene nanoribbons (GNRs) adopt the same naming as CNTs with armchair and zigzag nanoribbons defined by the shape of the ribbon edges. An additional pair of edge shapes have been suggested. Klein edges consist of lone carbon atoms attached to a zigzag edge [76]. These Klein edges would be expected to occur either as dangling methyl

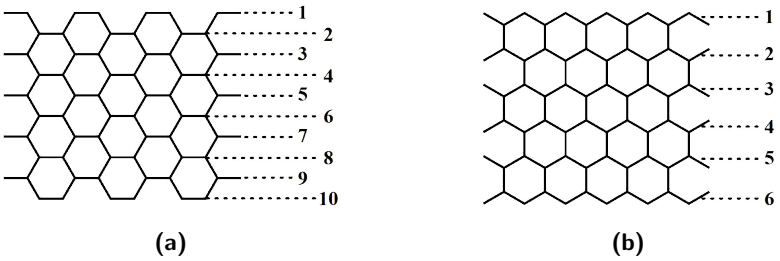

Figure 1.7: Figure (a) depicts an armchair nanoribbon with the numbers counting the dimer pairs to determine the nanoribbon index and figure (b) shows the same for zig-zag nanoriibons.

groups or as undercoordinated carbon atoms. The undercoordinated carbon atom edges can reconstruct to form 5-membered rings along the edge of the ribbon [77]. The zig-zag and armchair ribbons have been widely investigated but some effort has been made to investigate chiral ribbons [78, 79, 80]. Such ribbons have edges that consist of both zig-zag and armchair geometries. New edge shapes and nanoribbon geometries have been discovered experimentally in recent years [9, 81, 82].

Both zig-zag and armchair ribbons exhibit intriguing electrical properties due to their geometry. The structure of armchair ribbons can take two main forms, a staggered edge where each column of rings in the longitudinal direction contains the same number of rings or where each column has one more or one less than its immediate neighbours. Armchair nanoribbons can be differentiated by an index N based on the longitudinally aligned bonds, the first type has an even number and the second an odd number of these bonds. The method for determining the nanoribbon index is shown in figure 1.7(a). The band gaps of armchair GNRs (AGNRs) follow two distinct patterns. Firstly, the band gaps reduce as the ribbon width is increased, as would be expected so that at large widths the ribbon possess the zero band gap found in graphene. Secondly, the band gaps vary as a function of their index in steps of three. When $N = 3m + 2$, where m is some integer, ribbons have the smallest band gap. For $N = 3m$ the band gaps are larger and for $N = 3m + 1$ the gaps are larger again. Zig-zag ribbons possess an interesting electronic structure involving unpaired electrons that occupy orbitals localised along the edges of the ribbon. The ground state configuration for these electrons is ferromagnetic coupling longitudinally but antiferromagnetic coupling across the width. Early theoretical predictions suggested a zero band gap [83] but later spin-resolved calculations showed that the ribbons were semi-conductors [84]. The band gap can be manipulated through the application of an external electric field which shifts the bands for different spins causing the band gap to disappear for a specific spin [84]. This half-metallic behaviour, where the ribbon conducts electrons of a single spin, is of great interest for use in spintronic devices [21].

Graphene nanoribbons inherit many of the impressive mechanical properties of graphene. They show high tensile strength ($\approx$ 100 GPa) and stiffness ($\approx$ 1 TPa) which make

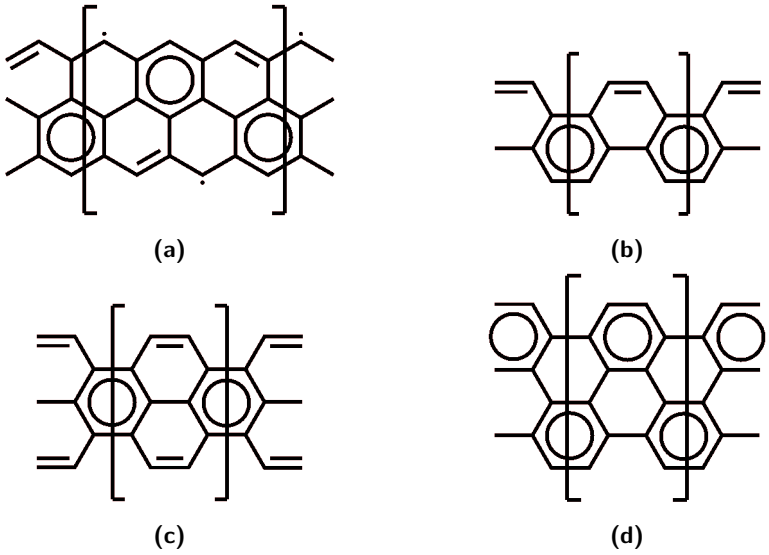

Figure 1.8: Clar structures for (a) PAA, (b) PP, (c) polyperylene and (d) PPhB.

them ideal for use as reinforcing fillers for polymers. These values are calculated using simulations of atomically perfect structures. Such structures have been produced using a bottom-up approach involving self-arrangement of monomer precursors on metallic surfaces followed by a dehydrogenation process that polymerises the ribbons [9, 85, 86, 87]. So far this process has been successfully used to generate a range of very narrow AGNRs [9, 85, 88] and a single ZGNR structure [87]. This process has also generated a number of novel GNR structures that had never been considered theoretically [9, 81, 82]. The first novel-type ribbon to be reported was chevron-type GNRs (CTGNRs) [9], so called due to their shape. Two other nanoribbon forms have also been synthesised, cove-type [81] and para-armchair [82] GNRs, and there may be many more yet to be discovered. The length of these synthesised ribbons tends to be limited to a few tens of nanometres but cove-type ribbons up to several hundred nanometres long have been reported [81].

Properties of nanoribbons

The earliest investigations of nanoribbons date from the early to mid 1980s. A Japanese team searching for conductive polymers investigated materials constructed of connected carbon rings. The structures investigated were polyacenacene (PAA) [8], polyphenanthrene (PP) [89], polyperylene [90] and polyphenanthrophenanthrene (PPhB) [91], shown in figure 1.8. Polyacenacene is a hydrogen terminated zig-zag nanoribbon and polyperylene, polyphenanthrene and polyphenanthrophenanthrene are the same as hydrogen terminated armchair nanoribbons. Polyperylene is now referred to as AGNR5 and polyphenanthrophenanthrene AGNR6. These structures were investigated using the tight-binding self-consistent-field method (CNDO/2) employing the complete neglect of

differential overlap. Although this method has long been surpassed it was able to determine some of the features of the electronic structure. The results for the PP/PPhB structures, AGNR4 and AGNR6 respectively, were that they possess a significant band gap [89, 91, 83]. The results for the polyperylene structure, AGNR5, showed a small band gap which the authors suggested could just be an artifact of the method [90]. Their suggestion that the structure could be metallic would be repeated years later [74] but it was shown that there are families of ribbons, based on their indices, with the same behaviour. Later studies utilising DFT would show that all narrow CNTs possess a non-zero band gap but agrees with the earlier prediction about variation of band gap with index [78, 92]. This in turn would be questioned by calculations performed using the many-electron Green's function approach which suggest that the band gaps are over twice the size of those predicted using local density approximation based DFT [93].

The investigation of PAA, a zig-zag nanoribbon, showed it to be metallic [8] with the lowest unoccupied and highest occupied states localised at the edges of the ribbon [83]. Later, it was suggested that the localised edge states of such structures might be spin polarised [76]. When this theory was tested using Hückel based unrestricted Hartree-Fock calculations the ribbon was shown to possess antiferromagnetically aligned edge states [94]. A decade later, zig-zag ribbons would be shown to be capable of half-metallic behaviour in the presence of a suitably aligned electric field [84].

The early interest in GNRs was due to their electrical properties, either for conductive polymers or for inducing a band gap in graphene, which have been investigated since the 1980s but the earliest investigations of their mechanical properties date from 2009 [95]. Some work had investigated the effect of strain on the electrical properties of GNRs [96] and shown that the band gap of AGNRs could be manipulated through tensile stain. Theoretical studies of ZGNRs performed using periodic DFT show the modulus of the ribbons has an inverse relationship with the ribbon width and tends to the value of bulk graphene for large widths [95]. Armchair ribbons simulated using a molecular mechanics potential in a dynamical simulation performed at 300 K found that narrow AGNRs had lower moduli compared to bulk graphene [97]. The moduli of the AGNRs increased to the bulk value as the width was increased. Semi-empirical Hartree-Fock studies involving short, low aspect ratio, ribbons conducted using both zig-zag and armchair GNRs predicted the modulus for ZGNRs is lower than that of AGNRs with comparable widths [98]. The predicted modulus for ZGNRs in that study was approximately half of what had been predicted using periodic DFT. However, due to the short finite lengths of ribbon used in the study it is difficult to make direct comparisons with those performed using high aspect ratios or periodic boundary conditions. Another quasi-static molecular mechanics study disagreed with the above result with ZGNRs possessing a higher modulus than AGNRs [99] and that the AGNR moduli were lower than that of bulk graphene. One study comparing the mechanical properties of the chevron-type GNR with those of AGNR9 as calculated using DFT disagree with earlier molecular mechanics

results. The AGNR9 was found to have a greater, rather than smaller, tensile modulus than bulk graphene. The CTGNR was found found to have a lower stiffness and strength compared to the AGNR9 which is expected as the CTGNR geometry can be viewed as a defect-containing armchair nanoribbon.

The potential for improving the properties of GNRs by altering their edge chemistry and creating more chemically stable edges has also been investigated. The magnetic edges of the singly hydrogenated zig-zag ribbons encourage functionalisation [100, 101] and studies have been performed to see if more stable edges could be found [102]. Unpaired electron states at the edges reduce the stablity, essentially imbuing the ribbons with a partial radical character [103]. Although single hydrogen terminated zig-zag GNR edges may exist they are predicted to be stable only at extremely low environmental H_2 concentrations [101]. This thinking has been extended to other environmental conditions such as the pressence of other gases such as oxygen, carbon dioxide, water, and ammonia [104, 105]. The calculations used for these studies ignore the kinetics of any functionalisation reactions but do highlight the vast array of possible edge terminations that can form on GNRs. Stabilisation of edges results in the loss of the localised unpaired spin orbitals which give rise to the semi-metallic properties of interest for the development of spintronic devices. The ability to produce specific edge structures would, however, be of great use when trying to employ graphene and GNRs for other purposes. Work investigating the use of nanoporous graphene for desalination requires the pore edges to be modified in such a way as to avoid clogging [106]. Edge functionalisation of GNRs would be very useful for incorporating GNRs in nanocomposite materials [107]. Such functionalisation could be utilised to improve both their dispersablity and degree of covalent bonding into a polymer network.

1.5 Nanocomposites

The term nanocomposites is used to cover a large array of different materials that have been developed for a variety of purposes. For this work only structural nanocomposite materials are of interest. This type of material seeks to improve the mechanical properties of one of its constituents by including some type of nanoparticles. Many standard structural composite materials are in use today, most of which are fibre reinforced polymers. In these materials, fibres with diameters of a few microns are combined with plastics to improve their mechanical performance. These materials have been in use for decades and their production, design and use have been studied in depth. Arguably the most well known of these is carbon fibre reinforced polymer due to its exceptional strength to weight ratio and specific stiffness [108]. These attributes make it very useful for producing structures whose weight must be kept to a minimum. Light weight structures are essential for aerospace applications but are increasingly relevant to the automotive sector. To meet the demands of such applications it is important that the

best possible composite is formed which is generally aligned carbon fibres embedded in an epoxy. The best possible weight to strength and weight to stiffness ratios for most polymer composites are only possible if the volume fraction of the fibres is maximised. This is achieved by producing aligned fibre mats and tapes which allow for the highest possible concentration of fibres in a given volume. Furthermore, the design of the material can be optimised by aligning the fibres with the principle load directions. As such carbon fibre reinforced polymers are normally laminates made of layers of highly aligned carbon fibres embedded in a polymer resin. This lamination process is generally used to create plate-like structures whose in-plane properties are determined by the fibre alignment. However, the interlaminar mechanical properties are determined solely by the mechanical properties of the polymer. It is this through-thickness behaviour that is the cause of many of the weaknesses of composite materials and serves as a motivation for the development of nanocomposites. By improving the properties of the polymer through nanoreinforcement it is possible to improve the interlaminar properties of carbon fibre based composite laminates.
It should be stated that the most common fibre reinforced polymers are based on glass fibres. These materials do not offer the weight savings that are possible with carbon fibre but they are much cheaper. Glass fibres offer a cost effective way to improve polymers and are regularly used in the form of short, chopped, randomly orientated fibres that can be mixed with polymer melts for use in injection moulding. The lack of fibre alignment lowers the amount of fibre content in the composite but does produce isotropic material properties. This approach is seldom used with carbon fibres as the resulting materials will not generate the weight savings, at least compared with metal alloys, necessary to justify their cost.

Polymer CNT nanocomposites

It took barely half a year from the discovery carbon nanotubes for the idea of producing a CNT reinforced nanocomposite material to be suggested [109]. The first polymer nanocomposite was reported two years later [110] but this was created to provide a means for handling and testing CNTs for use in experiments. It took some years before structural CNT based nanocomposites could be produced and tested as this would require CNT production to be capable of generating sufficient quantities of nanotubes at low cost. The first reported mechanical properties for such materials was in 1998 for a CNT/epoxy composite [111]. The material contained 5% multi-walled nanotubes by weight that were ultrasonically dispersed into the resin before curing. Results for the tensile modulus showed an increase of about 20% over neat epoxy but an increase of 25% for the compressive modulus. This difference was put down to the multi-walled structure of nanotubes whereby only the outer-most tube would respond to tensile deformation but all the layers of the MWCNT would respond in compression. Thin film testing of MWCNTs in a urethane/diacrylate mixture suggested that the stress transfer between

the nanotubes and the polymer matrix was an order of magnitude greater than that between conventional carbon fibres and polymers [112]. However, both of these works considered the fibre/matrix interactions using composite theory developed for microscale reinforcement. Application of these ideas to a CNT/PVA composite predicted a modulus for the nanotubes of only 150 MPa, four order of magnitude less than theoretical predictions, and could only be explained if the conventional micro composite shear-lag model did not apply at the nanoscale [113].
A considerably amount of work has been done on this type of polymer nanocomposite. The importance of the dispersion and functionalisation of nanotubes and the effect of the interphase region where the CNTs interact with the polymer matrix have been thoroughly investigated. There are many good review papers covering all of these aspects and much more [114, 115, 116, 117, 118].

Nanoparticle alignment

One of the issues with CNT based nanocomposite materials is the lack of alignment of the nanotubes. Fibre alignment in microscale composities is achieved by aligning tows of individual long continuous fibres. The alignment allows for the efficient packing of fibres increasing the fibre volume fraction of the resulting composite which improves the composite's mechanical properties. By aligning the fibres to the directions of the loads to which a structure is subjected it is possible to reduce the weight of structure at the design stage. The relatively short lengths of nanotubes, normally measured in microns, makes alignment for either purpose a much more challenging task.
One of the ideas to achieve alignment of nanotubes involves using the shear flow of liquid resin to align CNTs [119]. This method has the obvious drawback of needing to control the fluid dynamics of the resin. This is not achievable when dealing with complex multiscale materials such as fibre reinforced polymer composites. An alternative option involves combining the reinforcing particles with magnetic particles or coatings so that the reinforcement can be aligned to external magnetic fields. It can be achieved without introducing ferromagnetic coatings but it requires very large magnetic fields ($5 - 10$ T) in order to effect the diamagnetic nanotubes [120]. With the application of suitable magnetic nanoparticles, typically iron oxide, it is possible to reduce the required field strength down to managable levels ≈ 100 mT [121]. It has also been shown that careful positioning of the magnetic particles can help further reduce the required field strength [122]. This has been proposed as a method for creating composite repair patches for carbon fibre reinforced polymers [6].

CNT nanocomposite fibres and sheets

Another route towards nanocomposites is the production of nanocomposite fibres and sheets. Nanocomposite fibres are produced by mixing nanoparticles with polymers before

extruding or spinning a fine fibre [123, 124]. It is also possible to spin CNTs and use weak polymer solutions to provide a binder to hold the resulting thread together [125, 126]. The processes used for generating the threads align the nanotubes with the fibre axis which gives the fibre a high tensile strength and stiffness.
Nanocomposite sheets are produced from impregnating 'buckypaper' with a polymer resin [127]. The buckypaper consists of randomly aligned CNTs arranged in a planar format. By penetrating this precursor with polymer resin it is possible to create a laminar nanocomposite material.

Multiscale composite materials

Carbon nanotubes have been considered as a potential interlaminar reinforcement layer for improving the interlaminar toughness of composite materials. The CNTs are introduced between conventional carbon fibre textile sheets using one of several methods. One method is to paint CNTs dispersed in a liquid medium over the surface of the CFRP layer while manufacturing the composite laminate [128, 129]. An alternative to this is to create thin films of CNT containing polymer resin which can be placed between layers during the lamination process [130, 131]. These methods have been shown to improve interlaminar properties of carbon fibre reinforced polymers without introducing any detrimental effects to the mechanical properties of the composite. In these methods the nanotubes are randomly aligned which limits their effectiveness at improving the interlaminar properties. To achieve better results the CNTs need to be aligned to the through thickness direction of the laminate. Methods for achieving this have been investigated [5, 132] and commercially available products developed [133, 134].

Fuzzy fibres

The methods described above have provided a means to incorporate CNTs into a laminate to improve the interlaminar toughness but there is an alternative method for achieving this known as 'fuzzy fibres.' In this approach the CNTs are grown directly on the surface of fibres using chemical vapour deposition [4]. Composite laminates produced using these materials have been shown to have improved interlaminar toughness and strength [135]. However, the processes used to grow the CNTs on the carbon fibres is known to degrade the mechanical properties of the fibres [136]. Attempts to mitigate the degradation have been developed but they are not capable of totally eradicating the effect [137].

GNR polymer composites

A large amount of work has been conducted on CNT based nanocomposites, and it is still a very active research area, compared to work on graphene nanoribbon based composites. This is to be expected as CNTs were produced over a decade prior to nanoribbons. The first attempts at producing nanoribbons used lithographic methods to cut ribbons from

graphene. Such methods are unlikely to be scalable to the levels of production needed for bulk manufacture of nanocomposites so there was little impetus to research these materials. However, scalable nanoribbon production methods have since been developed which do open the door for research on GNR based nanocomposites.
The most common method for GNR synthesis involves 'unzipping' carbon nanotubes. This process normally uses oxidating chemicals to break the nanotube causing it to unroll. The resulting nanostructures have been shown to work better as a reinforcement particle than the CNTs from which they are derived [138]. In one of the earliest papers reporting this method an increase of 30% in tensile modulus and 22% in tensile strength of the resulting epoxy-based composite was reported in comparison to using the multi-walled CNTs from which the $50 - 100$ nm wide nanoribbons were derived [138]. The authors of this work took great care to thermally reduce the oxidised unzipped ribbons. This improves the properties of the ribbons but does require very high temperatures (1300 K). The properties of the composite are less impressive if oxidised ribbons are used but they still show improvements compared to unreinforced polymers [139, 140]. Non-oxidative methods have also been researched [141]. When unzipping the nanotubes the newly created edges are highly reactive and new functional groups form along these edges. These groups have a significant impact on the final composites properties [142] and can be used to improve nanoribbon dispersion [107].
Unzipping nanotubes is still the easiest method for producing large numbers of nanoribbons but it does have its drawbacks. The nanoribbons generated in this manner are relatively wide (≈ 100 nm) and the edges of the ribbon are unlikely to possess any uniformity. A newer method for producing nanoribbons involving a bottom-up assembly of monomers has the potential to change this situation [9]. This method has been able to produce a variety of different nanoribbon structures with regular edges and controlled geometry. The widths of the ribbons produced by this technique are less than 10 nm and theoretical studies suggest their tensile mechanical properties are greater than those of graphene [95]. This method of production may offer a way to mass produce highly regular, high aspect ratio, edge functionalised nanoribbons ideal for use in nanocomposites [81]. However, as fas as the author is aware there are no reports of the production of such nanocomposite materials at this time.

1.6 Conclusion

This chapter has introduced some of the core concepts of the following work. It has outlined the motivation for the work included in this thesis and provided an overview of the relevant concepts. Nanotubes and nanoribbons have been discussed and methods for describing them have been defined. The mechanical properties of these structures have been examined and the theoretical methods used for determining such properties have been introduced. Fibre reinforced composites and nanocomposites have been described

and some of the important features of these technologies explained.
The next chapter of this work is a more in-depth description of the computational methods used for the calculations in this thesis. In chapter 3 there is a description of work undertaken using the atomistic finite element method. This method is applied to boron-nitride nanotubes to calculate their piezoelectric properties which are then compared with results obtained from molecular mechanics. Chapter 4 investigates the tensile strength of carbon-carbon bonds calculated by a variety of different computational methods. Relationships between the types of bond, bond dissociation energies and structural considerations and how they effect peak bond tension are examined. From these results suitable methods for calculating mechanical properties of nanostructures are determined. Chapter 5 applies these methods to a variety of carbon nanoribbon structures to determine their tensile mechanical properties. A new relationship between ribbon index and Young's modulus is investigated. The properties of nanoribbons that have been produced experimentally are calculated for the first time and a study of their failure mechanisms is conducted. Finally, the conclusions of this work are summarised and a description of future work is provided.

Bibliography

[1] H. W. Kroto, J. R. Heath, S. C. O'Brien, R. F. Curl, and R. E. Smalley. C60: Buckminsterfullerene. *Nature*, 318(6042):162–163, 1985.

[2] S. Iijima. Helical microtubules of graphitic carbon. *Nature*, 354(6348):56–58, 1991.

[3] M. L. Manchado, L. Valentini, J. Biagiotti, and J. Kenny. Thermal and mechanical properties of single-walled carbon nanotubes–polypropylene composites prepared by melt processing. *Carbon*, 43(7):1499–1505, 2005.

[4] E. T. Thostenson, W. Z. Li, D. Z. Wang, Z. F. Ren, and T. W. Chou. Carbon nanotube/carbon fiber hybrid multiscale composites. *Journal of Applied Physics*, 91(9):6034–6037, 2002.

[5] E. J. Garcia, B. L. Wardle, and A. John Hart. Joining prepreg composite interfaces with aligned carbon nanotubes. *Composites Part A: Applied Science and Manufacturing*, 39(6):1065–1070, 2008.

[6] G. Ariu, I. Hamerton, and D. Ivanov. Positioning and aligning CNTs by external magnetic field to assist localised epoxy cure. *Open Physics*, 14(1):508–516, 2016.

[7] K. S. Novoselov. Electric Field Effect in Atomically Thin Carbon Films. *Science*, 306(5696):666–669, 2004.

[8] T. Yamabe, K. Tanaka, K. Ohzeki, and S. Yata. Electronic structure of polyacenacene. A one-dimensional graphite. *Solid State Communications*, 44(6):823–825, 1982.

[9] J. Cai, P. Ruffieux, R. Jaafar, M. Bieri, T. Braun, S. Blankenburg, M. Muoth, A. P. Seitsonen, M. Saleh, X. Feng, K. Müllen, and R. Fasel. Atomically precise bottom-up fabrication of graphene nanoribbons. *Nature*, 466(7305):470–473, 2010.

[10] A. Kekulé. Untersuchungen über aromatische Verbindungen Ueber die Constitution der aromatischen Verbindungen. I. Ueber die Constitution der aromatischen Verbindungen. *Annalen der Chemie und Pharmacie*, 137(2):129–196, 1866.

[11] J. W. Armit and R. Robinson. CCXI.—Polynuclear heterocyclic aromatic types. Part II. Some anhydronium bases. *J. Chem. Soc., Trans.*, 127(1604):1604–1618, 1925.

[12] E. Clar. *The Armonatic Sextet.* John Wiley and Sons, 1972.

[13] T.-A. Chen and R.-S. Liu. Synthesis of Polyaromatic Hydrocarbons from Bis(biaryl)diynes: Large PAHs with Low Clar Sextets. *Chemistry - A European Journal*, 17(29):8023–8027, 2011.

[14] T. Wassmann, A. P. Seitsonen, a. M. Saitta, M. Lazzeri, and F. Mauri. Clar's Theory, π-Electron Distribution, and Geometry of Graphene Nanoribbons. *Journal of the American Chemical Society*, 132(10):3440–3451, 2010.

[15] Y. Matsuo, K. Tahara, and E. Nakamura. Theoretical Studies on Structures and Aromaticity of Finite-Length Armchair Carbon Nanotubes. *Organic Letters*, 5(18):3181–3184, 2003.

[16] F. J. Martín-Martínez, S. Fias, B. Hajgató, G. Van Lier, F. De Proft, and P. Geerlings. Inducing aromaticity patterns and tuning the electronic transport of zigzag graphene nanoribbons via edge design. *Journal of Physical Chemistry C*, 117(49):26371–26384, 2013.

[17] E. Lieb and D. Mattis. Ordering energy levels of interacting spin systems. *Journal of Mathematical Physics*, 3(4):749–751, 1962.

[18] I. Gutman. Characteristic and matching polynomials of benzenoid hydrocarbons. *Journal of the Chemical Society, Faraday Transactions 2*, 79(3):337, 1983.

[19] S. Fajtlowicz, P. E. John, and H. Sachs. On Maximum Matchings and Eigenvalues of Benzenoid Graphs. *Croatica Chemica Acta*, 78(2):195–201, 2005.

[20] O. V. Yazyev. Emergence of magnetism in graphene materials and nanostructures. *Reports on Progress in Physics*, 73(5):056501, 2010.

[21] O. V. Yazyev and M. I. Katsnelson. Magnetic correlations at graphene edges: Basis for novel spintronics devices. *Physical Review Letters*, 100(4):1–4, 2008.

[22] W. L. Wang, O. V. Yazyev, S. Meng, and E. Kaxiras. Topological Frustration in Graphene Nanoflakes: Magnetic Order and Spin Logic Devices. *Physical Review Letters*, 102(15):157201, 2009.

[23] G. Trinquier, N. Suaud, and J.-P. Malrieu. Theoretical Design of High-Spin Polycyclic Hydrocarbons. *Chemistry - A European Journal*, 16(29):8762–8772, 2010.

[24] Z. Zhang and C. M. Lieber. Nanotube structure and electronic properties probed by scanning tunneling microscopy. *Applied Physics Letters*, 62(22):2792–2794, 1993.

[25] M. M. J. Treacy, T. W. Ebbesen, and J. M. Gibson. Exceptionally high Young's modulus observed for individual carbon nanotubes. *Nature*, 381(6584):678–680, 1996.

[26] S. P. Surwade, S. N. Smirnov, I. V. Vlassiouk, R. R. Unocic, G. M. Veith, S. Dai, and S. M. Mahurin. Water desalination using nanoporous single-layer graphene. *Nature nanotechnology*, 10(5):459–64, 2015.

[27] Y. Liu and X. Chen. Mechanical properties of nanoporous graphene membrane. *Journal of Applied Physics*, 115(3):034303, 2014.

[28] Z. Qi, D. K. Campbell, and H. S. Park. Atomistic simulations of tension-induced large deformation and stretchability in graphene kirigami. *Physical Review B*, 90(24):245437, 2014.

[29] J. Tersoff. New empirical approach for the structure and energy of covalent systems. *Physical Review B*, 37(12):6991–7000, 1988.

[30] D. W. Brenner. Empirical potential for hydrocarbons for use in simulating the chemical vapor deposition of diamond films. *Physical Review B*, 42(15):9458–9471, 1990.

[31] V.-T. Tran, J. Saint-Martin, P. Dollfus, and S. Volz. Third nearest neighbor parameterized tight binding model for graphene nano-ribbons. *AIP Advances*, 7(7):075212, 2017.

[32] E. Hückel. Quanstentheoretische Beiträge zum Benzolproblem. *Zeitschrift für Physik*, 72(5-6):310–337, 1931.

[33] J. Heyd, J. E. Peralta, G. E. Scuseria, and R. L. Martin. Energy band gaps and lattice parameters evaluated with the Heyd-Scuseria-Ernzerhof screened hybrid functional. *Journal of Chemical Physics*, 123(17), 2005.

[34] C. Møller and M. S. Plesset. Note on an Approximation Treatment for Many-Electron Systems. *Physical Review*, 46(7):618–622, 1934.

[35] F. Coester and H. Kümmel. Short-range correlations in nuclear wave functions. *Nuclear Physics*, 17(C):477–485, 1960.

[36] P.-O. Löwdin. Quantum Theory of Many-Particle Systems. I. Physical Interpretations by Means of Density Matrices, Natural Spin-Orbitals, and Convergence Problems in the Method of Configurational Interaction. *Physical Review*, 97(6):1474–1489, 1955.

[37] T. L. Gilbert. Optimum-Multiconfiguration Self-Consistent-Field Equations. *The Journal of Chemical Physics*, 43(10):S248–S251, 1965.

[38] S. Iijima and T. Ichihashi. Single-shell carbon nanotubes of 1-nm diameter. *Nature*, 363(6430):603–605, 1993.

[39] X. B. Zhang, X. F. Zhang, D. Bernaerts, G. van Tendeloo, S. Amelinckx, J. van Landuyt, V. Ivanov, J. B. Nagy, P. Lambin, and A. A. Lucas. The Texture of Catalytically Grown Coil-Shaped Carbon Nanotubules. *Europhysics Letters (EPL)*, 27(2):141–146, 1994.

[40] H. Dai. Carbon nanotubes: Synthesis, integration, and properties. *Accounts of Chemical Research*, 35(12):1035–1044, 2002.

[41] B. WenXing, Z. ChangChun, and C. WanZhao. Simulation of Young's modulus of single-walled carbon nanotubes by molecular dynamics. *Physica B: Condensed Matter*, 352(1-4):156–163, 2004.

[42] E. Hernández, C. Goze, P. Bernier, and A. Rubio. Elastic Properties of C and $B_xC_yN_z$ Composite Nanotubes. *Physical Review Letters*, 80(20):4502–4505, 1998.

[43] A. Rubio, J. L. Corkill, and M. L. Cohen. Theory of graphitic boron nitride nanotubes. *Physical Review B*, 49(7):5081–5084, 1994.

[44] N. G. Chopra, R. J. Luyken, K. Cherrey, V. H. Crespi, M. L. Cohen, S. G. Louie, and A. Zettl. Boron Nitride Nanotubes. *Science*, 269(5226):966–967, 1995.

[45] O. Stephan, P. M. Ajayan, C. Colliex, P. Redlich, J. M. Lambert, P. Bernier, and P. Lefin. Doping Graphitic and Carbon Nanotube Structures with Boron and Nitrogen. *Science*, 266(5191):1683–1685, 1994.

[46] P. Redlich, J. Loeffler, P. Ajayan, J. Bill, F. Aldinger, and M. Rühle. B-C-N nanotubes and boron doping of carbon nanotubes. *Chemical Physics Letters*, 260(3-4):465–470, 1996.

[47] R. Tenne, L. Margulis, M. Genut, and G. Hodes. Polyhedral and cylindrical structures of tungsten disulphide. *Nature*, 360(6403):444–446, 1992.

[48] J. Sha, J. Niu, X. Ma, J. Xu, X. Zhang, Q. Yang, and D. Yang. Silicon Nanotubes. *Advanced Materials*, 14(17):1219–1221, 2002.

[49] P. Hoyer. Formation of a Titanium Dioxide Nanotube Array. *Langmuir*, 12(6):1411–1413, 1996.

[50] J. Goldberger, R. He, Y. Zhang, S. Lee, H. Yan, H.-J. Choi, and P. Yang. Single-crystal gallium nitride nanotubes. *Nature*, 422(6932):599–602, 2003.

[51] M. Remskar, A. Mrzel, Z. Skraba, A. Jesih, M. Ceh, J. Demsar, P. Stadelmann, F. Levy, and D. Mihailovic. Self-Assembly of Subnanometer-Diameter Single-Wall MoS2 Nanotubes. *Science*, 292(5516):479–481, 2001.

[52] H. Guo, N. Lu, J. Dai, X. Wu, and X. C. Zeng. Phosphorene nanoribbons, phosphorus nanotubes, and van der Waals multilayers. *Journal of Physical Chemistry C*, 118(25):14051–14059, 2014.

[53] X. Wu, Z. Xu, and X. C. Zeng. Single-Walled MoTe 2 Nanotubes. *Nano Letters*, 7(10):2987, 2007.

[54] R. Saito, M. Fujita, G. Dresselhaus, and M. S. Dresselhaus. Electronic structure of chiral graphene tubules. *Applied Physics Letters*, 60(18):2204–2206, 1992.

[55] D. H. Robertson, D. W. Brenner, and J. W. Mintmire. Energetics of nanoscale graphitic tubules. *Physical Review B*, 45(21):12592–12595, 1992.

[56] A. Lucas, P. Lambin, and R. Smalley. On the energetics of tubular fullerenes. *Journal of Physics and Chemistry of Solids*, 54(5):587–593, 1993.

[57] J. Tersoff and R. S. Ruoff. Structural Properties of a Carbon-Nanotube Crystal. *Physical Review Letters*, 73(5):676–679, 1994.

[58] B. I. Yakobson, C. J. Brabec, and J. Bernholc. Nanomechanics of Carbon Tubes: Instabilities beyond Linear Response. *Physical Review Letters*, 76(14):2511–2514, 1996.

[59] C. Cornwell and L. Wille. Elastic properties of single-walled carbon nanotubes in compression. *Solid State Communications*, 101(8):555–558, 1997.

[60] G. Van Lier, C. Van Alsenoy, V. Van Doren, and P. Geerlings. Ab initio study of the elastic properties of single-walled carbon nanotubes and graphene. *Chemical Physics Letters*, 326(1-2):181–185, 2000.

[61] A. Krishnan, E. Dujardin, T. W. Ebbesen, P. N. Yianilos, and M. M. J. Treacy. Young's modulus of single-walled nanotubes. *Physical Review B*, 58(20):14013–14019, 1998.

[62] J.-P. Salvetat, A. J. Kulik, J.-M. Bonard, G. A. D. Briggs, T. Stöckli, K. Méténier, S. Bonnamy, F. Béguin, N. A. Burnham, and L. Forró. Elastic Modulus of Ordered and Disordered Multiwalled Carbon Nanotubes. *Advanced Materials*, 11(2):161–165, 1999.

[63] N. G. Chopra and A. Zettl. Measurement of the elastic modulus of a multi-wall boron nitride nanotube. *Solid State Communications*, 105(5):297–300, 1998.

[64] D. Golberg, P. M. F. J. Costa, O. Lourie, M. Mitome, X. Bai, K. Kurashima, C. Zhi, C. Tang, and Y. Bando. Direct Force Measurements and Kinking under Elastic Deformation of Individual Multiwalled Boron Nitride Nanotubes. *Nano Letters*, 7(7):2146–2151, 2007.

[65] X. Wei, M. S. Wang, Y. Bando, and D. Golberg. Tensile tests on individual multi-walled boron nitride nanotubes. *Advanced Materials*, 22(43):4895–4899, 2010.

[66] K. N. Kudin, G. E. Scuseria, and B. I. Yakobson. C_2F, BN, and C nanoshell elasticity from *ab initio* computations. *Physical Review B*, 64(23):235406, 2001.

[67] N. M. Anoop Krishnan and D. Ghosh. Chirality dependent elastic properties of single-walled boron nitride nanotubes under uniaxial and torsional loading. *Journal of Applied Physics*, 115(6):064303, 2014.

[68] V. Verma, V. K. Jindal, and K. Dharamvir. Elastic moduli of a boron nitride nanotube. *Nanotechnology*, 18(43):435711, 2007.

[69] E.-S. Oh. Elastic properties of boron-nitride nanotubes through the continuum lattice approach. *Materials Letters*, 64(7):859–862, 2010.

[70] R. Ansari, M. Mirnezhad, and S. Sahmani. Prediction of chirality- and size-dependent elastic properties of single-walled boron nitride nanotubes based on an accurate molecular mechanics model. *Superlattices and Microstructures*, 80:196–205, 2015.

[71] E. J. Mele and P. Král. Electric Polarization of Heteropolar Nanotubes as a Geometric Phase. *Physical Review Letters*, 88(5):056803, 2002.

[72] N. Sai and E. J. Mele. Microscopic theory for nanotube piezoelectricity. *Physical Review B*, 68(24):241405, 2003.

[73] I. Naumov, A. M. Bratkovsky, and V. Ranjan. Unusual Flexoelectric Effect in Two-Dimensional Noncentrosymmetric sp^{2}-Bonded Crystals. *Physical Review Letters*, 102(21):217601, 2009.

[74] K. Nakada, M. Fujita, G. Dresselhaus, and M. S. Dresselhaus. Edge state in graphene ribbons: Nanometer size effect and edge shape dependence. *Physical Review B*, 54(24):17954–17961, 1996.

[75] Z. Chen, Y.-M. Lin, M. J. Rooks, and P. Avouris. Graphene nano-ribbon electronics. *Physica E: Low-dimensional Systems and Nanostructures*, 40(2):228–232, 2007.

[76] D. J. Klein. Graphitic polymer strips with edge states. *Chemical Physics Letters*, 217(3):261–265, 1994.

[77] P. Wagner, V. V. Ivanovskaya, M. Melle-Franco, B. Humbert, J. J. Adjizian, P. R. Briddon, and C. P. Ewels. Stable hydrogenated graphene edge types: Normal and reconstructed Klein edges. *Physical Review B - Condensed Matter and Materials Physics*, 88(9):1–6, 2013.

[78] V. Barone, O. Hod, and G. E. Scuseria. Electronic Structure and Stability of Semiconducting Graphene Nanoribbons. *Nano Letters*, 6(12):2748–2754, 2006.

[79] H. Zhao, K. Min, and N. R. Aluru. Size and Chirality Dependent Elastic Properties of Graphene Nanoribbons under Uniaxial Tension. *Nano Letters*, 9(8):3012–3015, 2009.

[80] Y. Chu, T. Ragab, P. Gautreau, and C. Basaran. Mechanical Properties of Hydrogen Edge–Passivated Chiral Graphene Nanoribbons. *Journal of Nanomechanics and Micromechanics*, 5(4):04015001, 2015.

[81] A. Narita, X. Feng, Y. Hernandez, S. A. Jensen, M. Bonn, H. Yang, I. A. Verzhbitskiy, C. Casiraghi, M. R. Hansen, A. H. R. Koch, G. Fytas, O. Ivasenko, B. Li, K. S. Mali, T. Balandina, S. Mahesh, S. De Feyter, and K. Müllen. Synthesis of structurally well-defined and liquid-phase-processable graphene nanoribbons. *Nature Chemistry*, 6(2):126–132, 2014.

[82] Y. Huang, Y. Mai, U. Beser, J. Teyssandier, G. Velpula, H. Van Gorp, L. A. Straasø, M. R. Hansen, D. Rizzo, C. Casiraghi, R. Yang, G. Zhang, D. Wu, F. Zhang, D. Yan, S. De Feyter, K. Müllen, and X. Feng. Poly(ethylene oxide) Functionalized Graphene Nanoribbons with Excellent Solution Processability. *Journal of the American Chemical Society*, 138(32):10136–10139, 2016.

[83] K. Tanaka, S. Yamashita, H. Yamabe, and T. Yamabe. Electronic properties of one-dimensional graphite family. *Synthetic Metals*, 17(1-3):143–148, 1987.

[84] Y.-W. Son, M. L. Cohen, and S. G. Louie. Half-metallic graphene nanoribbons. *Nature*, 444(7117):347–349, 2006.

[85] Y.-C. Chen, D. G. de Oteyza, Z. Pedramrazi, C. Chen, F. R. Fischer, and M. F. Crommie. Tuning the Bandgap of Graphene Nanoribbons Synthesized from Molecular Precursors. *ACS Nano*, 7(7):6123–6128, 2013.

[86] T. H. Vo, M. Shekhirev, D. A. Kunkel, F. Orange, M. J.-F. Guinel, A. Enders, and A. Sinitskii. Bottom-up solution synthesis of narrow nitrogen-doped graphene nanoribbons. *Chem. Commun.*, 50(32):4172–4174, 2014.

[87] P. Ruffieux, S. Wang, B. Yang, C. Sánchez-Sánchez, J. Liu, T. Dienel, L. Talirz, P. Shinde, C. A. Pignedoli, D. Passerone, T. Dumslaff, X. Feng, K. Müllen, and R. Fasel. On-surface synthesis of graphene nanoribbons with zigzag edge topology. *Nature*, 531(7595):489–492, 2016.

[88] H. Zhang, H. Lin, K. Sun, L. Chen, Y. Zagranyarski, N. Aghdassi, S. Duhm, Q. Li, D. Zhong, Y. Li, K. Müllen, H. Fuchs, and L. Chi. On-Surface Synthesis of Rylene-Type Graphene Nanoribbons. *Journal of the American Chemical Society*, 137(12):4022–4025, 2015.

[89] K. Tanaka, K. Ohzeki, S. Nankai, T. Yamabe, and H. Shirakawa. The electronic structures of polyacene and polyphenanthrene. *Journal of Physics and Chemistry of Solids*, 44(11):1069–1075, 1983.

[90] K. Tanaka, K. Ueda, T. Koike, and T. Yamabe. Electronic structure of polyperylene. *Solid State Communications*, 51(12):943–945, 1984.

[91] K. Tanaka, T. Koike, K. Ueda, K. Ohzeki, T. Yamabe, and S. Yata. Electronic structures of polyacenacene and polyphenanthrophen anthrene. Design of one-dimensional graphite. *Synthetic Metals*, 11(2):61–73, 1985.

[92] Y. W. Son, M. L. Cohen, and S. G. Louie. Energy gaps in graphene nanoribbons. *Physical Review Letters*, 97(21):1–4, 2006.

[93] L. Yang, C.-H. Park, Y.-W. Son, M. L. Cohen, and S. G. Louie. Quasiparticle Energies and Band Gaps in Graphene Nanoribbons. *Physical Review Letters*, 99(18):186801, 2007.

[94] M. Fujita, K. Wakabayashi, K. Nakada, and K. Kusakabe. Peculiar Localized State at Zigzag Graphite Edge, 1996.

[95] R. Faccio, P. A. Denis, H. Pardo, C. Goyenola, and Á. W. Mombrú. Mechanical properties of graphene nanoribbons. *Journal of Physics: Condensed Matter*, 21(28):285304, 2009.

[96] L. Sun, Q. Li, H. Ren, H. Su, Q. W. Shi, and J. Yang. Strain effect on electronic structures of graphene nanoribbons: A first-principles study. *The Journal of Chemical Physics*, 129(7):074704, 2008.

[97] H. Bu, Y. Chen, M. Zou, H. Yi, K. Bi, and Z. Ni. Atomistic simulations of mechanical properties of graphene nanoribbons. *Physics Letters, Section A: General, Atomic and Solid State Physics*, 373(37):3359–3362, 2009.

[98] Y. Gao and P. Hao. Mechanical properties of monolayer graphene under tensile and compressive loading. *Physica E: Low-Dimensional Systems and Nanostructures*, 41(8):1561–1566, 2009.

[99] Q. Lu, W. Gao, and R. Huang. Atomistic simulation and continuum modeling of graphene nanoribbons under uniaxial tension. *Modelling and Simulation in Materials Science and Engineering*, 19(5):054006, 2011.

[100] D. E. Jiang, B. G. Sumpter, and S. Dai. How do aryl groups attach to a graphene sheet? *Journal of Physical Chemistry B*, 110(47):23628–23632, 2006.

[101] T. Wassmann, A. P. Seitsonen, A. M. Saitta, M. Lazzeri, and F. Mauri. Structure, Stability, Edge States, and Aromaticity of Graphene Ribbons. *Physical Review Letters*, 101(9):096402, 2008.

[102] O. Hod, V. Barone, J. E. Peralta, and G. E. Scuseria. Enhanced half-metallicity in edge-oxidized zigzag graphene nanoribbons. *Nano Letters*, 7(8):2295–2299, 2007.

[103] D. E. Jiang, B. G. Sumpter, and S. Dai. Unique chemical reactivity of a graphene nanoribbon's zigzag edge. *Journal of Chemical Physics*, 126(13), 2007.

[104] A. P. Seitsonen, A. M. Saitta, T. Wassmann, M. Lazzeri, and F. Mauri. Structure and stability of graphene nanoribbons in oxygen, carbon dioxide, water, and ammonia. *Physical Review B Condensed Matter*, 82(11):115425, 2010.

[105] G. Soldano, M. Juarez, B. Teo, and E. Santos. Structure and stability of graphene edges in O2 and H2 environments from ab initio thermodynamics. *Carbon*, 78:181–189, 2014.

[106] J. Lee, Z. Yang, W. Zhou, S. J. Pennycook, S. T. Pantelides, and M. F. Chisholm. Stabilization of graphene nanopore. *Proceedings of the National Academy of Sciences of the United States of America*, 111(21):7522–6, 2014.

[107] J. D. Saathoff and P. Clancy. Effect of edge-functionalization on the ease of graphene nanoribbon aggregation in solvent. *Carbon*, 115:154–161, 2017.

[108] D. Hull and T. Clyne. *An Introduction to Composite Materials*. Cambridge University Press, 1996.

[109] P. Calvert. Strength in disunity. *Nature*, 357(6377):365–366, 1992.

[110] P. M. Ajayan, O. Stephan, C. Colliex, and D. Trauth. Aligned Carbon Nanotube Arrays Formed by Cutting a Polymer Resin–Nanotube Composite. *Science*, 265(5176):1212–1214, 1994.

[111] L. S. Schadler, S. C. Giannaris, and P. M. Ajayan. Load transfer in carbon nanotube epoxy composites. *Applied Physics Letters*, 73(26):3842–3844, 1998.

[112] H. D. Wagner, O. Lourie, Y. Feldman, and R. Tenne. Stress-induced fragmentation of multiwall carbon nanotubes in a polymer matrix. *Applied Physics Letters*, 72(2):188–190, 1998.

[113] M. S. P. Shaffer and A. H. Windle. Fabrication and characterization of carbon nanotube/poly(vinyl alcohol) composites. *Advanced Materials*, 11(11):937–941, 1999.

[114] E. T. Thostenson, Z. Ren, and T.-W. Chou. Advances in the science and technology of carbon nanotubes and their composites: a review. *Composites Science and Technology*, 61(13):1899–1912, 2001.

[115] J. N. Coleman, U. Khan, and Y. K. Gun'ko. Mechanical Reinforcement of Polymers Using Carbon Nanotubes. *Advanced Materials*, 18(6):689–706, 2006.

[116] P.-C. Ma, N. A. Siddiqui, G. Marom, and J.-K. Kim. Dispersion and functionalization of carbon nanotubes for polymer-based nanocomposites: A review. *Composites Part A: Applied Science and Manufacturing*, 41(10):1345–1367, 2010.

[117] D. G. Papageorgiou, I. A. Kinloch, and R. J. Young. Mechanical properties of graphene and graphene-based nanocomposites. *Progress in Materials Science*, 90:75–127, 2017.

[118] V. D. Punetha, S. Rana, H. J. Yoo, A. Chaurasia, J. T. McLeskey, M. S. Ramasamy, N. G. Sahoo, and J. W. Cho. Functionalization of carbon nanomaterials for advanced polymer nanocomposites: A comparison study between CNT and graphene. *Progress in Polymer Science*, 67:1–47, 2017.

[119] E. Camponeschi, B. Florkowski, R. Vance, G. Garrett, H. Garmestani, and R. Tannenbaum. Uniform Directional Alignment of Single-Walled Carbon Nanotubes in Viscous Polymer Flow. *Langmuir*, 22(4):1858–1862, 2006.

[120] T. Kimura, H. Ago, M. Tobita, S. Ohshima, M. Kyotani, and M. Yumura. Polymer Composites of Carbon Nanotubes Aligned by a Magnetic Field. *Advanced Materials*, 14(19):1380–1383, 2002.

[121] H. Le Ferrand, S. Bolisetty, A. F. Demirörs, R. Libanori, A. R. Studart, and R. Mezzenga. Magnetic assembly of transparent and conducting graphene-based functional composites. *Nature Communications*, 7(May):12078, 2016.

[122] R. M. Erb, R. Libanori, N. Rothfuchs, and A. R. Studart. Composites Reinforced in Three Dimensions by Using Low Magnetic Fields. *Science*, 335(6065):199–204, 2012.

[123] J. C. Kearns and R. L. Shambaugh. Polypropylene fibers reinforced with carbon nanotubes. *Journal of Applied Polymer Science*, 86(8):2079–2084, 2002.

[124] P. Miaudet, S. Badaire, M. Maugey, A. Derré, V. Pichot, P. Launois, P. Poulin, and C. Zakri. Hot-Drawing of Single and Multiwall Carbon Nanotube Fibers for High Toughness and Alignment. *Nano Letters*, 5(11):2212–2215, 2005.

[125] B. Vigolo. Macroscopic Fibers and Ribbons of Oriented Carbon Nanotubes. *Science*, 290(5495):1331–1334, 2000.

[126] A. B. Dalton, S. Collins, E. Muñoz, J. M. Razal, V. H. Ebron, J. P. Ferraris, J. N. Coleman, B. G. Kim, and R. H. Baughman. Super-tough carbon-nanotube fibres. *Nature*, 423(6941):703–703, 2003.

[127] J. N. Coleman, W. J. Blau, A. B. Dalton, E. Muñoz, S. Collins, B. G. Kim, J. Razal, M. Selvidge, G. Vieiro, and R. H. Baughman. Improving the mechanical properties of single-walled carbon nanotube sheets by intercalation of polymeric adhesives. *Applied Physics Letters*, 82(11):1682–1684, 2003.

[128] S. C. Joshi and V. Dikshit. Enhancing interlaminar fracture characteristics of woven CFRP prepreg composites through CNT dispersion. *Journal of Composite Materials*, 46(6):665–675, 2012.

[129] T. Lyashenko, N. Lerman, A. Wolf, H. Harel, and G. Marom. Improved Mode II delamination fracture toughness of composite materials by selective placement of protein-surface treated CNT. *Composites Science and Technology*, 85:29–35, 2013.

[130] R. J. Sager, P. J. Klein, D. C. Davis, D. C. Lagoudas, G. L. Warren, and H.-J. Sue. Interlaminar fracture toughness of woven fabric composite laminates with carbon nanotube/epoxy interleaf films. *Journal of Applied Polymer Science*, 121(4):2394–2405, 2011.

[131] V. Eskizeybek, A. Yar, and A. Avcı. CNT-PAN hybrid nanofibrous mat interleaved carbon/epoxy laminates with improved Mode I interlaminar fracture toughness. *Composites Science and Technology*, 157:30–39, 2018.

[132] R. Guzman de Villoria, P. Hallander, L. Ydrefors, P. Nordin, and B. Wardle. In-plane strength enhancement of laminated composites via aligned carbon nanotube interlaminar reinforcement. *Composites Science and Technology*, 133:33–39, 2016.

[133] B. L. Wardle and S.-G. Kim. Nano-engineered material architectures: Ultra-tough hybrid nanocomposite system, 2009.

[134] B. L. Wardle, A. J. Hart, E. J. Garcia, and A. H. Slocum. Nano-engineered material architectures: Ultra-tough hybrid nanocomposite system, 2012.

[135] V. P. Veedu, A. Cao, X. Li, K. Ma, C. Soldano, S. Kar, P. M. Ajayan, and M. N. Ghasemi-Nejhad. Multifunctional composites using reinforced laminae with carbon-nanotube forests. *Nature Materials*, 5(6):457–462, 2006.

[136] Z. H. Hu, S. M. Dong, J. B. Hu, Z. Wang, B. Lu, J. S. Yang, Q. G. Li, B. Wu, L. Gao, and X. Y. Zhang. Synthesis of carbon nanotubes on carbon fibers by modified chemical vapor deposition. *Xinxing Tan Cailiao/New Carbon Materials*, 27(5):352–361, 2012.

[137] T. R. Pozegic, I. Hamerton, J. V. Anguita, W. Tang, P. Ballocchi, P. Jenkins, and S. R. Silva. Low temperature growth of carbon nanotubes on carbon fibre to create a highly networked fuzzy fibre reinforced composite with superior electrical conductivity. *Carbon*, 74:319–328, 2014.

[138] M. A. Rafiee, W. Lu, A. V. Thomas, A. Zandiatashbar, J. Rafiee, J. M. Tour, and N. a. Koratkar. Graphene Nanoribbon Composites. *ACS Nano*, 4(12):7415–7420, 2010.

[139] G. Lalwani, A. M. Henslee, B. Farshid, L. Lin, F. K. Kasper, Y.-X. Qin, A. G. Mikos, and B. Sitharaman. Two-Dimensional Nanostructure-Reinforced Biodegradable Polymeric Nanocomposites for Bone Tissue Engineering. *Biomacromolecules*, 14(3):900–909, 2013.

[140] L. Gan, S. Shang, C. W. M. Yuen, S. X. Jiang, and N. M. Luo. Facile preparation of graphene nanoribbon filled silicone rubber nanocomposite with improved thermal and mechanical properties. *Composites Part B: Engineering*, 69:237–242, 2015.

[141] S. Sadeghi, M. Arjmand, I. Otero Navas, A. Zehtab Yazdi, and U. Sundararaj. Effect of Nanofiller Geometry on Network Formation in Polymeric Nanocomposites: Comparison of Rheological and Electrical Properties of Multiwalled Carbon Nanotube and Graphene Nanoribbon. *Macromolecules*, 50(10):3954–3967, 2017.

[142] R. Nadiv, M. Shtein, M. Buzaglo, S. Peretz-Damari, A. Kovalchuk, T. Wang, J. M. Tour, and O. Regev. Graphene nanoribbon – Polymer composites: The critical role of edge functionalization. *Carbon*, 99:444–450, 2016.

Chapter 2

Methods

Different methods can be employed for predicting the shape and behaviours of molecular structures. At the highest and most computationally expensive levels of theory are electronic structure methods. These find approximate solutions for the electronic wavefunctions by solving equations derived from quantum mechanics. In this case the Schrödinger equation is solved in order to find an electronic wavefunction. However, electrons are interacting particles and for a system of such particles the problem becomes analytically intractable. Instead, approximations are made which allow numerical methods to be applied so approximate solutions can be found. There are different methods for solving approximations to the Schrödinger equation which generally follow the trend of increasing accuracy resulting in increasing computational complexity. The electronic structure methods used in this work include Møller-Plesset perturbation theory (MP), density-functional theory (DFT) and density-functional tight-binding (DFTB).

Another method for investigating molecular structures is through the use of empirical force fields or molecular mechanics. This method avoids the Schrödinger equation and does not calculate the electronic structure. The interactions between electrons and between the electrons and nuclei are not calculated. Instead, the interaction between atoms is approximated by simple analytical functions containing parameters obtained by fitting to known molecular properties. These functions can then be used for predicting the energetics of structural conformations of molecules. Although this lowers the computational expense significantly it comes at the cost of applicability. Information relating to the electronic behaviour, such as electronic band gaps, magnetic states and conductivities, is unavailable. These methods also rely on the accuracy and applicability of their parametrisations. Most empirical force fields are only useful for predicting molecular structures near or at their minimum energy conformations.

This chapter provides a brief overview of the methods used in the work presented in this thesis. First, the theory of various electronic structure methods are described and then there is a brief discussion on molecular mechanics force fields.

2.1 Electronic structure methods

Electronic structure calculations attempt to solve the time independent Schrödinger equation [1] for a system of particles. This equation is written as

$$\left(-\frac{1}{2}\nabla^2 + V(\boldsymbol{r})\right)\Psi = E\Psi, \tag{2.1}$$

where E is the energy of system described by wavefunction Ψ and $V(\boldsymbol{r})$ is a spatially varying potential. This form assumes all quantities are given in atomic units: the units of charge and mass are the charge and mass of an electron respectively and the reduced Planck's constant for action. This is equivalent to setting these quantities along with the Coulomb force constant $K_\mathrm{e} = 1/(4\pi\epsilon_0)$ to a value of 1. The atomic units combine to give the unit of length as the Bohr radius and the unit of energy as the Hartree. In this manner all the physical constants that appear in the Schrödinger equation when using S.I. units disappear leaving just the operators, wavefunction and energy. Equation 2.1 is written in an operator form as

$$\hat{H}\Psi = E\Psi, \tag{2.2}$$

where $\hat{H} = -\frac{1}{2}\nabla^2 + V(\mathbf{r})$ is the Hamiltonian operator for the system. The first term in the Hamiltonian is the kinetic energy operator and the second term is the potential energy operator. This differential equation can be solved for any specific system to find a set of orthogonal eigenfunctions with corresponding energy eigenvalues. The eigenfunctions are normalised to provide an orthonormal set. For a molecule the Hamiltonian consists of kinetic energy operators for both electrons and nuclei as well as nuclei-nuclei, nuclei-electron and electron-electron interaction potentials. In most electronic structure calculations the Born-Oppenheimer approximation is applied to the Hamiltonian [2]. This assumes that as electrons are much less massive than nuclei they will alter their behaviour instantaneously to any change in the positions of the nuclei. This allows the nuclei to be considered as static particles, and their kinetic energy can be neglected. For an atom with a single electron the potential $V(\mathbf{r})$ is simply the electrostatic potential produced by the atomic nucleus. For polyelectronic systems the Hamiltonian becomes significantly more complex. The Hamiltonian for N electrons and M nuclei is

$$\hat{H} = -\frac{1}{2}\sum_{i=1}^{N}\nabla_i^2 - \sum_{i=1}^{M}\sum_{A=1}^{N}\frac{Z_A}{r_{iA}} + \sum_{i=1}^{N}\sum_{j>i}^{N}\frac{1}{r_{ij}}, \tag{2.3}$$

where the index i runs over the electrons, index A runs over the nuclei, r_{ij} is the distance between particles i and j and Z_A is the charge on nuclei A. The first sum gives the electronic kinetic energy contributions, the second gives the interaction between the nuclei and the electrons and the third gives the electron-electron interactions. The electrostatic repulsion between the nuclei is omitted in this instance as it is constant with respect to

the electron wave function and therefore does not affect them. Nevertheless, internuclear repulsion energy must be included when computing the total energy of any molecule.

The electron interaction term of the Hamiltonian operator leads to two problems. Firstly, the electrons repel each other electrostatically and secondly electrons are fermions so they obey the Pauli exclusion principle [3]. The first issue is normally handled by incorporating electron-electron interactions into the Hamiltonian by way of a mean-field approximation whereby each electron interacts with the rest through a mean-field potential. This in turn requires an iterative approach, known as the self-consistent-field (SCF) method, to find a converged solution for the problem starting from an initial guess for the electron-electron interaction potential. Rather than solve the system for the total wavefunction it is normal to generate a set of one-particle wavefunctions, or spin-orbitals, and combine them to form a many-particle solution. The second problem requires that the Hamiltonian must remain unchanged when swapping particle labels,

$$\hat{H}(1,2) = \hat{H}(2,1). \tag{2.4}$$

and the Pauli principle requires that the total wave function changes sign when swapping particle labels:

$$\Phi(1,2,3) = -\Phi(2,1,3) = \Phi(2,3,1)\ldots. \tag{2.5}$$

For non-interacting particles the total wavefunction Φ can be written as a set of one particle spin orbitals ϕ_i multiplied together,

$$\Phi(1,2,3) = \phi_1(1)\phi_2(2)\phi_3(3), \tag{2.6}$$

where subscripts number the spin orbitals and the numbers in brackets indicate particle coordinates. However, such wavefunctions are not antisymettric with respect to particle exchange and do not obey the Pauli principle for fermions. To ensure the above constraints for interacting particles the total wavefunction must include all possible permutations of electrons in all spin orbitals. For a three electron system the wavefunction is

$$\begin{aligned}\Phi(1,2,3) = A(&\phi_1(1)\phi_2(2)\phi_3(3) - \phi_1(1)\phi_2(3)\phi_3(2) - \phi_1(2)\phi_2(1)\phi_3(3) \\ &+\phi_1(3)\phi_2(1)\phi_3(2) + \phi_1(2)\phi_2(3)\phi_3(1) - \phi_1(3)\phi_2(2)\phi_3(1)),\end{aligned} \tag{2.7}$$

where $A = 1/\sqrt{6}$ is the normalisation factor. This is more succinctly written in general form as a Slater determinant [4]

$$\Phi = \frac{1}{\sqrt{N!}}\begin{vmatrix} \phi_1(1) & \phi_2(1) & \cdots & \phi_N(1) \\ \phi_1(2) & \phi_2(2) & \cdots & \phi_N(2) \\ \vdots & \vdots & \ddots & \vdots \\ \phi_1(N) & \phi_2(N) & \cdots & \phi_N(N) \end{vmatrix}, \tag{2.8}$$

where N electrons occupy N spin orbitals. A spin orbital for an electron can be decomposed into two parts, the spatial component ψ and a spin component σ. The spin component describes the electron spin, either 'up' or 'down', and the spatial component describes the electron's spatial wavefunction. Each spatial wavefunction can hold two electrons provided those electrons have different spins. For a two-electron system where both electrons occupy the same spatial function, the overall wavefunction is written as

$$\Phi = 1/\sqrt{2}\left[\psi(1)\psi(2)\left(\sigma_1(\uparrow)\sigma_2(\downarrow) - \sigma_1(\downarrow)\sigma_2(\uparrow)\right)\right]. \tag{2.9}$$

The spin component of this function ensures the electrons are indistinguishable and meet the antisymmetry principle (the minus sign). By expanding out the bracket and rearranging to get

$$\Phi = 1/\sqrt{2}\left[\psi(1)\sigma_1(\uparrow)\psi(2)\sigma_2(\downarrow) - \psi(1)\sigma_1(\downarrow)\psi(2)\sigma_2(\uparrow)\right], \tag{2.10}$$

it is straightforward to see the connection with the Slater determinant

$$1/\sqrt{2}\begin{vmatrix}\psi(1)\sigma_1(\uparrow) & \psi(1)\sigma_1(\downarrow)\\ \psi(2)\sigma_2(\uparrow) & \psi(2)\sigma_2(\downarrow)\end{vmatrix}. \tag{2.11}$$

The equations presented here form the basis for electronic structure calculations. The missing component to dealing with these equations is that both the orbitals and the energies must be calculated. This requires a method for calculating the mean-field potential for electron-electron interactions and finding a suitable basis for describing the orbital functions.

2.2 Basis Sets

Most electronic structure methods use a set of basis functions from which linear combinations can be used to describe molecular orbitals. The basis prescribes the analytical form of the orbitals and reduces the problem to one of finding linear coefficients for each basis function to produce a set of molecular orbitals. Basis functions are commonly formed from approximate representations of the atomic orbitals of individual atoms. A reasonable starting point is Slater-type orbitals (STOs) which are based on hydrogenic orbitals with the radial component of the orbital scaled according to Slater's rules [5]. The hydrogenic orbitals can be calculated analytically by solving the time independent Schrödinger equation for a single electron in a radially symmetric potential. The solutions are written as

$$\Psi(n, m, l) = R_{nl}(r)Y_{ml}(\theta, \phi), \tag{2.12}$$

where n, l and m are quantum numbers, $R_{nl}(r)$ is the radial function and $Y_{ml}(\theta, \phi)$ is the angular part which are the spherical harmonic functions. The radial function is

$$R_{nl}(r) = A_{nl} \left(\frac{2Zr}{na_\mu} \right)^l e^{-Zr/na_\mu} L_{nl}(r), \tag{2.13}$$

where A_{nl} is the normalisation coefficient, $L_{nl}(r)$ is a generalised Laguerre polynomial, Z is the nuclear charge and a_μ is a physical constant related to the reduced mass of the system. Slater orbitals simplify the radial expression to

$$R_{nl}(r) = Ar^{n^*-1} e^{-\zeta r} \tag{2.14}$$

where A is the normalisation coefficient, n^* is a modified principle quantum number and $\zeta = (Z - s)/n^*$ where s is a shielding constant. The shielding constant s depends on quantum numbers and shell occupancies according to Slater's rules. Slater orbitals modify the radial function by considering the inner electrons as shielding the nuclear charge from the outer electrons. A key difference between hydrogenic and Slater orbitals is the loss of the radial nodes seen in hydrogenic orbitals. Although Slater orbitals are very useful they are difficult to implement in molecular calculations due to the complexity in calculating integrals involving two atomic orbitals based on different atoms, known as two-center integrals. To simplify the problem it is possible to approximate Slater orbitals using linear combinations of Gaussian functions such that

$$R_{nl}(r) = r^{n-1} \sum_i c_i e^{-\alpha_i r^2}, \tag{2.15}$$

where c_i and α_i are fitted parameters. These Gaussian-approximated Slater orbitals are the atomic orbitals which make up many basis sets. More recent atomic orbital basis sets fit Gaussian functions to more advanced calculations of the atomic orbitals. The molecular spin orbitals that are sought can now be formed by taking linear combinations of basis set functions which minimise the energy of the system. The linear combinations of atomic orbitals (LCAO) method forms the basis of most electronic structure calculations.

It is worth noting that the linear combinations of Gaussian functions can be fitted to reproduce atomic electron wavefunctions and are not limited to STOs. It must also be pointed out that density-functional theory (DFT) can use a much more diverse array of basis functions. DFT is routinely performed using plane waves for calculations of solids, where it is computationally beneficial to perform part of the calculation in reciprocal space, but other basis set options are also available (e.g. numerical basis sets).

The quality of the calculated molecular orbitals can be improved by adding more functions to the basis set. The basis set limit is used to describe the point at which the total minimum energy for a calculation stops changing as more basis functions are included. It is usual to check basis set convergence to ensure the accuracy of any calculation is

not being hindered by the choice of basis. Basis functions are an important part of any electronic structure calculation and hundreds of different sets are available. The general requirement for most basis sets is that they can be used in integrals where up to four basis functions, centred on as many nuclear coordinates, can be computed with relative ease. The source of these integrals comes from the mean-field approximation used in computing the electron-electron interactions discussed in the following sections.

2.3 Hartree-Fock theory

The Hartree-Fock method [6, 7] breaks the Hamiltonian into three parts: the internuclear repulsion, the core Hamiltonian operator and the electron interaction operator. The internuclear repulsion operator provides the energy due to the internuclear repulsion which is uncoupled from the electronic behaviour by applying the Born-Oppenheimer approximation. The core operator for the ith electron is

$$\hat{H}_i^{\text{core}} = -\frac{1}{2}\nabla_i^2 - \sum_{A=1}^{M} \frac{Z_A}{r_{iA}}, \tag{2.16}$$

where the first term is the kinetic energy operator and the second term is the interaction between the electron and the M nuclear charges present in the system. The electron interaction term involves the expression

$$V_{ee}(\tau_i, \tau_j) = \int\int \Phi^* \frac{1}{r_{ij}} \Phi \, \mathrm{d}\tau_i \, \mathrm{d}\tau_j \tag{2.17}$$

where $V^{ee}(\tau_i, \tau_j)$ is the electronic interaction energy between electrons i and j, τ the spatial and spin coordinates of an electron, Φ the total wavefunction in the form of a Slater determinant and r_{ij} is the electron interaction operator. The * indicates the complex conjugate of the wavefunction. This integral can be expanded out to a series of integrals involving the two electrons in different spin orbitals. The values of many of these integrals is zero, due to orthogonality of the spin orbitals, leaving two main types of integrals to compute called the Coulomb and exchange integrals. These integrals take the forms

$$J_{ij} = \int\int \chi_i^*(1)\chi_j^*(2)\frac{1}{r_{ij}}\chi_i(1)\chi_j(2) \, \mathrm{d}\tau_1 \, \mathrm{d}\tau_2 \qquad \text{and} \tag{2.18}$$

$$K_{ij} = \int\int \chi_i^*(1)\chi_j^*(2)\frac{1}{r_{ij}}\chi_i(2)\chi_j(1) \, \mathrm{d}\tau_1 \, \mathrm{d}\tau_2, \tag{2.19}$$

where χ_i indicates spin orbital i and the numbers in brackets indicate the electronic coordinates over which the integration is performed. J is the Coulomb integral and it describes the electrostatic repulsion between two continuous charge distributions. K is the exchange integral and it describes the energy due to the exchange of the two electrons in their respective spin orbitals. If $i = j$ then $J_{ij} = K_{ij}$ and if the two spin orbitals are

of opposite spin then $K_{ij} = 0$. The electron interaction energy can be written as

$$V_{ee} = \sum_{ij} J_{ij} - K_{ij}. \tag{2.20}$$

The electron interaction operator can be similarly defined by breaking down the operator into Coulomb and exchange terms. The Coulomb operator is

$$\hat{J}_j = \int \chi_j(2) \frac{1}{r_{12}} \chi_j(2) \, \mathrm{d}\tau_2, \tag{2.21}$$

where χ_j is a real valued spin orbital. This operator provides the average Coulombic potential energy between an electron and an electron in orbital χ_j. Similarly, the exchange operator is defined in terms of

$$\hat{K}_j(1)\chi_i(1) = \left(\int \chi_j(2) \frac{1}{r_{12}} \chi_i(2) \, \mathrm{d}\tau_2 \right) \chi_j(1). \tag{2.22}$$

The exchange operator takes this form because it can only be defined by its effect when operating on the orbital $\chi_i(1)$. Unlike the Coulomb operator, for which a potential can be defined, the exchange operator depends on the value of $\chi_i(1)$ for the entire space not just at a single point and so is non-local [8]. In a LCAO calculation the integrals will be expanded in terms of the basis functions which gives rise to the four centre integrals discussed in the previous section.

The Fock operator can now be defined as

$$\hat{f}_i(1) = \hat{H}^{\mathrm{core}}(1) + \sum_{j=1}^{N} \hat{J}_j(1) - \hat{K}_j(1). \tag{2.23}$$

The first term calculates the energy of an electron moving in the field of the bare nuclei and is described as a one-electron operator as it depends only on the coordinates of a single electron. The second term introduces the electron-electron interaction by way of a mean-field potential acting on an electron and is called a two-electron operator, as are the Coulomb and exchange operators, as it depends on the coordinates of pairs of electrons. The Fock operator is an *effective* one-electron operator as it represents the effect of the total system of particles on a single electron by creating a potential based on the mean field of the electrons. The Fock operator provides a means for finding a set of spin orbitals from which the total wavefunction can be constructed by forming a Slater determinant.

A Hartree-Fock calculation solves the set of equations

$$\hat{f}_i \chi_i = \varepsilon_i \chi_i \tag{2.24}$$

for the spin orbitals and their associated energies. Throughout the calculation the spin

orbitals are represented by a linear sum of atomic orbitals so the equation above becomes

$$\hat{f}_i \sum_p C_{ip}\phi_p = \varepsilon_i \sum_p C_{ip}\phi_p, \tag{2.25}$$

where ϕ_p is a basis set function and C_{ip} is a coefficient for the basis set function p in molecular orbital i. Multiplying both sides by any basis function and integrating gives

$$\sum_p C_{ip} \int \phi_q \hat{f} \phi_p \, \mathrm{d}\tau = \varepsilon_i \sum_p C_{ip} \int \phi_q \phi_p \, \mathrm{d}\tau. \tag{2.26}$$

This gives rise to two matrix elements:

$$F_{qp} = \int \phi_q \hat{f} \phi_p \, \mathrm{d}\tau = \left\langle \phi_q \left| \hat{f} \right| \phi_p \right\rangle, \tag{2.27}$$

and

$$S_{qp} = \int \phi_q \phi_p \, \mathrm{d}\tau = \langle \phi_q | \phi_p \rangle, \tag{2.28}$$

which form the Fock matrix $\boldsymbol{F}$ and the overlap matrix $\boldsymbol{S}$. Note that the basis set functions are not orthogonal so the overlap matrix will contain off diagonal elements. These matricies can then be combined with the coefficient matrix formed from the C_{ip} to create the Roothan Hall equations [9, 10]:

$$\boldsymbol{FC} = \boldsymbol{SCE}, \tag{2.29}$$

where $\boldsymbol{E}$ is a diagonal matrix containing the spin orbital energy eigenvalues. This equation can then be solved using an initial guess of the eigenvector matrix to find the entries of $\boldsymbol{F}$ which can then be diagonalised to find a new set of eigenvectors and eigenvalues. The eigenvectors give the coefficients found in $\boldsymbol{C}$ and the eigenvalues in $\boldsymbol{E}$. The new coefficients can then be used to form new molecular orbitals which can be used to find new Fock matrix elements. This process is then repeated until the eigenvalues satisfy some convergence criteria at which point the molecular orbitals are described as self consistent.

Most molecules have a spin-paired ground state where all electrons are spin-paired. Such states can be reasonably described by computing a single set of spatial wavefunctions that can be used for both spin-up and spin-down electrons. Such calculations are referred to as spin-restricted Hartree-Fock. The alternative is to generate separate spatial wavefunctions for electrons of different spin, called unrestricted Hartree-Fock. In unrestricted Hartree-Fock theory the equations are separated according to orbital spins. This creates two sets of matrix equations with two corresponding sets of orbitals, one for spin-up and one for spin-down. The two sets still interact through the Coulomb operator but the electrons now fill orbitals with independent spatial components rather than having one spatial orbital containing two electrons. Unrestricted Hartree-Fock is therefore more computationally expensive than the restricted variant but it does produce better results

for molecules containing unpaired electrons.

Hartree-Fock is not, by itself, used in the work presented here. However, a number of post Hartree-Fock methods are used which start from a converged Hartree-Fock wavefunction. Hartree-Fock, in the basis set limit, does not necessarily produce quantitatively correct answers. The difference between the exact total energy and the restricted Hartree-Fock energy is referred to as the correlation energy. There are two important approximations used in Hartree-Fock are that give rise to correlation energy. First, the eigenfunction is written as a single Slater determinant. In many instances this will not cause significant issues but it will not accurately describe a system where two or more determinants have degenerate or nearly degenerate energy eigenvalues. This situation occurs in situations such as bond dissociation where a molecule changes from a spin-paired ground state to a pair of radical fragments after dissociation. Second, the electron-electron interactions are calculated as the interaction between one electron and the mean field of the others. This fails to fully account for the instantaneous electrostatic repulsion between them which results in less correlated electronic behaviour and therefore higher energies. This latter correlation energy is referred to as dynamic correlation and the former as static correlation and various methods have been developed to include both types of correlation energy to improve the accuracy of the calculation.

2.4 Møller Plesset perturbation theory

One method to recover some of the correlation energy missing from the Hartree-Fock method was proposed by Møller and Plesset in 1934 [11]. This method relies on the knowledge that the Hartree-Fock wavefunction recovers about 99% of the total energy. This implies that the wavefunction only requires a small perturbation to become exact. Rayleigh-Schrödinger perturbation theory [12] can be applied to the problem in the form specified by Møller and Plesset. The basis for the theory is that the exact Hamiltonian can be written as

$$\hat{H} = \hat{H}_0 + \lambda \hat{H}', \tag{2.30}$$

where $\hat{H}_0$ is a known Hamiltonian operator with known eigenfunctions $\Phi_i^{(0)}$ and known eigenvalues $E_i^{(0)}$, λ a constant and $\hat{H}'$ the perturbation operator. This can be expanded using a Taylor expansion in powers of λ to give

$$E_i = E_i^{(0)} + \lambda E_i^{(1)} + \lambda^2 E_i^{(2)} + \ldots, \tag{2.31}$$

and

$$\Phi_i = \Phi_i^{(0)} + \lambda \Phi_i^{(1)} + \lambda^2 \Phi_i^{(2)} + \ldots, \tag{2.32}$$

where E_i and Φ_i are eigenvalues and eigenfunctions of the exact Hamiltonian. Substituting the expansions of the exact Hamiltonian and the eigenvalues and eigenfunctions

into the Schrödinger equation yields

$$\left(\hat{H}_0 + \lambda\hat{H}'\right)\left(\Phi_i^{(0)} + \lambda\Phi_i^{(1)} + \lambda^2\Phi_i^{(2)} + \ldots\right) = \tag{2.33}$$

$$\left(E_i^{(0)} + \lambda E_i^{(1)} + \lambda^2 E_i^{(2)} + \ldots\right)\left(\Phi_i^{(0)} + \lambda\Phi_i^{(1)} + \lambda^2\Phi_i^{(2)} + \ldots\right). \tag{2.34}$$

This expression can be broken down by equating powers of λ to produce

$$\hat{H}_0\Phi_i^{(0)} = E_i^{(0)}\Phi_i^{(0)}, \tag{2.35}$$

$$\hat{H}_0\Phi_i^{(1)} + \hat{H}'\Phi_i^{(0)} = E_i^{(0)}\Phi_i^{(1)} + E_i^{(1)}\Phi_i^{(0)}, \tag{2.36}$$

$$\hat{H}_0\Phi_i^{(2)} + \hat{H}'\Phi_i^{(1)} = E_i^{(0)}\Phi_i^{(2)} + E_i^{(1)}\Phi_i^{(1)} + E_i^{(2)}\Phi_i^{(0)}, \tag{2.37}$$

and in general,

$$\hat{H}_0\Phi_i^{(n)} + \hat{H}'\Phi_i^{(n-1)} = \sum_k E_i^{(k)}\Phi_i^{(n-k)}. \tag{2.38}$$

To calculate the first order correction we note that $\Phi_i^{(0)}$ is a complete orthonormal basis generated by the unperturbed operator. This allows the first order correction to the wavefunction to be written as a linear combination in this basis,

$$\Phi_i^{(1)} = \sum_k a_{ik}\Phi_k^{(0)}. \tag{2.39}$$

Substituting this into equation 2.36 and rearranging gives

$$\left(\hat{H}' - E_i^{(1)}\right)\Phi_i^{(0)} = \sum_k a_{ik}\left(E_i^{(0)} - E_k^{(0)}\right)\Phi_k^{(0)}, \tag{2.40}$$

which by multiplying by the complex conjugate of $\Phi_i^{(0)}$ and integrating over all space gives the first order correction to the energy,

$$E_i^{(1)} = \int \Phi_i^{(0)*}\hat{H}'\Phi_i^{(0)}\,\mathrm{d}\tau. \tag{2.41}$$

The coefficients a_{ik} can then found by multiplying both sides of 2.40 by $\Phi_j^{(0)*}$, where $j \neq i$, and integrating over all space to find

$$a_{ij} = \frac{\int \Phi_j^{(0)*}\hat{H}'\Phi_i^{(0)}\,\mathrm{d}\tau}{E_i^{(0)} - E_j^{(0)}} \tag{2.42}$$

where $a_{ii} = 0$ by way of intermediate normalisation. A similar process can be used to determine higher order corrections.

Møller-Plesset perturbation theory uses an unperturbed operator constructed from the sum of Fock operators

$$\hat{H}_0 = \sum_n \left(-\frac{1}{2}\nabla_n^2 - \sum_m \frac{Z_m}{r_{nm}} + \sum_p (J_{np} - K_{np}) \right). \tag{2.43}$$

The basis functions $\Phi^{(0)}$ are therefore the set of determinants made by arranging the electrons in every possible combination of the Hartree-Fock orbitals. The sum of the Fock operators is not the same as the Hartree-Fock total energy operator as it will double count the electron-electron interaction energies. This means the perturbation operator can be defined as

$$\hat{H}' = \frac{1}{2}\sum_{np} \frac{1}{r_{np}} - \sum_p (J_{np} - K_{np}), \tag{2.44}$$

which in turn means the sum of the zero-order and first-order energies is equal to the Hartree-Fock energy. The terms in the perturbation operator are all dependent on two electrons so it is a two-particle operator. The expectation value of a two-particle operator between a ground state and a singly-excited state is zero due to Brillouin's theorem. Expectation values of the operator between the ground state and any excited state beyond second order are also zero. This means that eigenstates, $\Phi_i^{(0)}$ of the $\hat{H}_0$ operator that need to be considered are the ground and doubly-excited determinants. In theory there are an infinite number of excited molecular orbitals leading to an infinite number of excited determinants (of any order), but in practice the number of excited orbitals is determined by the size of the basis set used in a calculation. The number of doubly-excited determinants increases with the number of unoccupied excited orbitals such that the number of doubly-excited determinants is given by

$$M_{\text{Doubles}} = \binom{n}{2}\binom{K-n}{2}, \tag{2.45}$$

where n is the number of electrons and K the total number of molecular orbitals which depends on the size of the basis set. Most modern basis sets will generate more unoccupied than occupied orbitals and the basis will increase with the number of atoms. The effect of this scaling makes Møller-Plesset perturbation theory computationally expensive to implement on large molecules. Møller-Plesset perturbation theory is most commonly used at the second-order perturbation level (MP2) due to the ever worse scaling when higher order perturbations are included. MP2 scales as N^5, where N is the number of basis functions, with each increase in the perturbation level resulting in an increase in the scaling by a factor of N (MP3 scales as N^6, MP4 as N^7 etc.).

The main alternative to MP2 is density-functional theory (DFT) which can provide reasonable results in comparison to MP2 at a much lower computational cost, scaling as N^3. MP2 is generally more accurate than DFT and it behaves in a more reliable manner

making it a useful benchmark for comparison. MP2 is also used in conjunction with multi-configuration self-consistent field methods for including the dynamic correlation that such methods are less able at calculating.

2.5 Density-functional theory

The premise of density-functional theory (DFT) is that the Hamiltonian operator for a specific arrangement of nuclei is a functional of the ground-state electron density distribution of the system. This was proved by Hohenberg and Kohn with the so-called Hohenberg-Kohn existence theorem and a further theory, the Hohenberg-Kohn variational theory, proved that for any constant external potential all densities other than the ground-state will give higher energies than the ground-state energy [13]. In order to make use of these ideas it is necessary to model the electrons as non-interacting thus allowing the Hamiltonian to be described as a sum of one-electron operators [14]. The eigenfunctions of the Hamiltonian will be Slater determinants, composed of the one-electron eigenfunctions, and the corresponding eigenvalues are sums of the one-electron eigenvalues. This approach relies on the Hohenberg-Kohn theorems in that if a ground-state density can be found using non-interacting electrons that define the same nuclei and nuclear positions of a real system then the non-interacting system must have the same electron density function as the real system.

The equation for the total energy of a system of electrons as a functional of the electron density is

$$E\left[\rho\right] = T\left[\rho\right] + E_{\mathrm{Ext}}\left[\rho\right] + J\left[\rho\right] + E_{\mathrm{XC}}\left[\rho\right], \tag{2.46}$$

where E is the total energy, ρ the total electron density, T the non-interacting kinetic energy functional, E_{Ext} the external potential functional, J the non-interacting classical Coulomb interaction functional and E_{XC}, the exchange-correlation functional which contains the correction to the kinetic functional needed to reproduce the interacting system and all non-classical electron interaction terms. The total density ρ is related to the electron wave functions via

$$\rho = \sum_{i=1}^{N} \phi_i^* \phi_i, \tag{2.47}$$

where ϕ_i is the i th electron wavefunction and N is the total number of electrons. The kinetic energy of the electrons is normally computed through use of electron wavefunctions that reproduce the correct density. This leads to

$$T\left[\rho\right] = \sum_{i=1}^{N} \int \phi_i^*(\boldsymbol{r}) \left(-\frac{1}{2}\nabla^2\right) \phi_i(\boldsymbol{r})\, \mathrm{d}\boldsymbol{r}, \tag{2.48}$$

where $\boldsymbol{r}$ are the electronic coordinates and the central bracket contains the kinetic energy

operator from the Schrödinger equation. The external potential follows similarly with

$$E_{\mathrm{Ext}}\left[\rho\right] = -\sum_{A=1}^{M} \int \frac{Z_A \rho(\boldsymbol{r})}{|\boldsymbol{r} - \boldsymbol{r}_A|}\,\mathrm{d}\boldsymbol{r}, \tag{2.49}$$

where Z_A are the M nuclear charges and $\boldsymbol{r}_A$ their postions. The Coulomb interaction functional is very similar to the Coulomb integral but uses the total density's self-interaction rather than electron wavefunctions,

$$J\left[\rho\right] = \frac{1}{2}\int\int \frac{\rho(\boldsymbol{r})\rho(\boldsymbol{r}')}{|\boldsymbol{r} - \boldsymbol{r}'|}\,\mathrm{d}\boldsymbol{r}'\,\mathrm{d}\boldsymbol{r}, \tag{2.50}$$

where $\boldsymbol{r}$ and $\boldsymbol{r}'$ are dummy coordinates for the integrals. The factor of one half deals with the double counting that occurs as

$$\rho = \sum_i \rho_i, \tag{2.51}$$

where ρ_i are the electron densities for each electron, which when substituted into equation 2.50 gives

$$J\left[\rho\right] = \frac{1}{2}\int\int \sum_{ij} \frac{\rho_i(\boldsymbol{r}_1)\rho_j(\boldsymbol{r}_2)}{|\boldsymbol{r}_1 - \boldsymbol{r}_2|}\,\mathrm{d}\boldsymbol{r}_1\,\mathrm{d}\boldsymbol{r}_2. \tag{2.52}$$

The double counting can be seen explicitly in this expression as the interaction between two electrons is included in the sum twice (e.g. the interaction between electron densities 1 and 2 is calculated when $i = 1, j = 2$ and $i = 2$ and $j = 1$). This leaves the exchange-correlation potential E_{XC}, which contains all the necessary corrections to make DFT exact, to be determined.

In order to work within this formalism a set of non-interacting electron orbitals must be determined. This is done in a fashion similar to the Hartree-Fock method but with the Fock operator replaced with the one-electron Kohn-Sham operator [14]

$$\hat{h}_i = -\frac{1}{2}\nabla_i^2 - \sum_{A=1}^{M} \frac{Z_A}{|\boldsymbol{r}_i - \boldsymbol{r}_A|} + \int \frac{\rho(\boldsymbol{r}')}{|\boldsymbol{r}_i - \boldsymbol{r}'|}\,\mathrm{d}r' + V_{\mathrm{XC}} \tag{2.53}$$

where

$$V_{\mathrm{XC}} = \frac{\delta E_{\mathrm{XC}}}{\delta \rho}. \tag{2.54}$$

This operator combined with a set of initial guess orbitals allows a set of matrix elements to be determined using

$$K_{qp} = \int \phi_q \hat{h} \phi_p\,\mathrm{d}\tau. \tag{2.55}$$

This is analogous to the Fock matrix in the Roothan-Hall equations and leads to a similar

set of equations, called the Kohn-Sham equations, which can be written as

$$\boldsymbol{KC} = \boldsymbol{SCE}, \tag{2.56}$$

where $\boldsymbol{C}$ are eigenvectors of basis set coefficients, $\boldsymbol{S}$ is the overlap matrix as defined previously and $\boldsymbol{E}$ is a diagonal matrix of the energy eigenvalues. A self-consistent procedure can be applied to find converged energy eigenvalues and eigenvectors that provide the Kohn-Sham orbitals. The Kohn-Sham orbitals are not the true orbitals for a system, except if the exchange-correlation functional were to be exact, but they will produce a reasonable electron density function. Hohenberg and Kohn proved that there is a universal exchange-correlation energy functional that will provide the exact energy for any system of electrons. However, the form of this exact functional is unknown but a large number of approximate functionals have been created.

The earliest exchange-correlation functional was based on the analytic result for the electron exchange-correlation energy of a uniform electron gas as a function of a spatially constant electron density, known as the local density approximation (LDA). The LDA functional assumes that the exchange-correlation energy for a point in space with a specific electron density is equivalent to the exchange-correlation energy for the uniform electron gas at the same density. Clearly the density for a molecule changes throughout space so alternative functionals include corrections based on the gradient, or indeed higher derivatives, of the density. Further improvements have been made by mixing in the exact exchange calculated using the Kohn-Sham orbitals, known as hybrid methods. This logic has been extended by introducing an MP2 correction, using determinants composed of Kohn-Sham orbitals, to provide a perturbation based correlation energy.

One key reason for using DFT is its ability to use arbitrary basis sets, including plane wave basis sets, which makes it particularly attractive for calculations in reciprocal space. This allows infinite crystals to be modelled which permits the calculation of bulk properties of condensed matter without having to simulate very large numbers of atoms. A plane wave basis set can be determined by setting a cutoff energy for the basis functions. This allows the user to test for basis set convergence by increasing the cutoff energy until calculated properties converge.

Although extremely useful and more scalable than most post Hartree-Fock methods DFT is still limited to systems of about a couple of hundred atoms. To model larger systems further approximations must be made which in turn requires further compromises in accuracy.

2.6 Density-functional tight-binding approximation

The density-functional tight-binding method (DFTB) is a parametrised DFT method. The method uses a DFT one-electron operator based on a fixed reference density which

is assumed to be close to the density of the system of interest. This allows values for an effective potential based on the reference system to be pre-calculated and stored and also removes the self-consistent field iterations used in Hartree-Fock or DFT [15, 16].

As a starting point it is useful to consider the energy of a molecule as given by DFT,

$$\begin{aligned} E_{\mathrm{DFT}}\left[\rho(\boldsymbol{r})\right] = & \sum_{i}^{\mathrm{occ.}} \left\langle \chi_i(\boldsymbol{r}) \left| \hat{h}_i\left[\rho(\boldsymbol{r})\right] \right| \chi_i(\boldsymbol{r}) \right\rangle - \frac{1}{2} \int\int \frac{\rho(\boldsymbol{r}')\rho(\boldsymbol{r})}{|\boldsymbol{r}-\boldsymbol{r}'|}\,\mathrm{d}\boldsymbol{r}'\,\mathrm{d}\boldsymbol{r} \\ & - \int V_{\mathrm{XC}}\left[\rho(\boldsymbol{r})\right]\,\mathrm{d}\boldsymbol{r} + E_{\mathrm{XC}}\left[\rho(\boldsymbol{r})\right] + E_{\mathrm{II}}, \end{aligned} \tag{2.57}$$

where the first term is simply the sum of orbital energy eigenvalues and the next three are corrections to the double counting of electron-electron interaction energies and the last term is the energy due to the ionic repulsion of the bare nuclei. The one-electron operators

$$\hat{h}_i\left[\rho(\boldsymbol{r})\right] = -\frac{1}{2}\nabla^2 + \sum_{A}^{M} \frac{Z_A}{|\boldsymbol{r}_i - \boldsymbol{r}_A|} + \int \frac{\rho(\boldsymbol{r}')}{|\boldsymbol{r}_i - \boldsymbol{r}'|}\,\mathrm{d}\boldsymbol{r}' + V_{\mathrm{XC}}\left[\rho(\boldsymbol{r})\right] \tag{2.58}$$

are used to build a matrix which is diagonalised to find the orbitals χ. If some reference density ρ_0 that is close to the exact density can be used in these equations then the orbitals can be computed by a single diagonalisation. In standard DFT the density is recomputed for every new set of orbitals and is then used to find new one-electron operators $\hat{h}_i$, which are then used to find new orbitals until self consistency is achieved. In DFTB it is assumed that the reference density is close enough to the true density for the computed orbitals and energy eigenvalues to be reasonable approximations of orbitals and energies computed using full DFT.

To proceed it is necessary to define a basis set which can be used to describe the orbitals. DFTB uses a minimal atomic orbital basis set based on compressed orbitals of neutral atoms. A DFT calculation is performed on single atoms using the modified one-electron operator

$$\hat{h}_{\mathrm{C}} = -\frac{1}{2}\nabla^2 - \frac{Z}{r} + \int \frac{\rho(\boldsymbol{r}')}{|\boldsymbol{r}_i - \boldsymbol{r}'|}\,\mathrm{d}\boldsymbol{r}' + V_{\mathrm{XC}} + \left(\frac{r}{r_0}\right)^2 \tag{2.59}$$

where the last term is introduced to constrain the electron density closer to the nucleus than the free neutral atom with r_0 as a variational parameter. The minimal basis set provides a single radial function for each angular momentum state, i.e. one for s-states, three for p-states, five for d-states etc., and uses real spherical functions to describe the angular component.

With the basis set defined it is possible to compute the overlap and Hamiltonian matrix elements for different orbitals on different atoms. This is done once, over a range of internuclear distances, and the result is stored in tables for use in calculations. The

overlap matrix elements are given by

$$S_{pq} = \int \phi_p(\boldsymbol{r})^* \phi_q(\boldsymbol{r}) \, \mathrm{d}\boldsymbol{r}, \tag{2.60}$$

where the ϕ's are orbitals of the constrained atoms and are described by single basis functions from the minimal set. The Hamiltonian matrix elements are calculated using

$$H_{pq} = \begin{cases} \varepsilon_p, & \text{if } p = q \\ \left\langle \phi_p^A \left| \hat{T} + V_{\text{eff}}\left[\rho_0\right] \right| \phi_q^B \right\rangle & \text{if } A \neq B \\ 0 & \text{otherwise,} \end{cases} \tag{2.61}$$

where ε_p is the Kohn-Sham eigenvalue for the neutral unconfined atom, A and B denote different atoms and $V_{\text{eff}}\left[\rho_0\right]$ is the sum of the effective potentials due to the densities of the confined atoms. The overlap and Hamiltonian matrix entries for pairs of different atoms can be computed over a range of different internuclear distances and stored for later use.

A Hamiltonian matrix based on the confined atomic densities can be used to calculate molecular orbitals and their corresponding energy eigenvalues. The sum of the occupied orbital energies is referred to as the band structure energy and for any given molecule this should be close to the band structure energy computed using full DFT. However, equation 2.57 shows that the DFT based total energy includes four other terms that are yet to be included in the DFTB calculation. These missing components are combined into a single potential referred to as the repulsive potential [15] leading to

$$E_{\text{Tot}} = E_{\text{BS}}\left[\rho_0\right] + E_{\text{Rep}}, \tag{2.62}$$

where $E_{\text{BS}}\left[\rho_0\right]$ is the band structure energy, i.e the sum of the energy eigenvalues, E_{Rep} the repulsive potential and E_{Tot} is the total energy. The repulsive potential is found by subtracting the DFTB band structure energy for a given molecule from the total energy, calculated by using any suitable means e.g. DFT, MP2, coupled cluster method etc [17]. The repulsive energy is calculated in this way over a range of internuclear distances and stored for later use.

This is the most basic form of DFTB known as non-self-consistent DFTB [16] as the calculation for any user supplied molecular geometry requires a single diagonalisation of the Hamiltonian matrix to find the molecular orbitals and energy eigenvalues. The non-self-consistent approach does not allow for any charge transfer between the atoms, which is common for molecules containing atoms with different electronegativities. This shortfall is addressed by modifying the equations to include not just the reference density but also a small density fluctuation i.e. $\rho \to \rho + \delta\rho$. By expanding the equation for total

energy, equation 2.57, to second order in $\delta\rho$ the total energy becomes [15]

$$\begin{aligned} E\left[\rho_0(\boldsymbol{r})+\delta\rho(\boldsymbol{r})\right] =& E\left[\rho_0(\boldsymbol{r})\right] \\ &+\frac{1}{2}\int\int\left(\frac{1}{|\boldsymbol{r}-\boldsymbol{r}'|}+\frac{\partial^2 E_{\mathrm{XC}}}{\partial\rho(\boldsymbol{r})\partial\rho(\boldsymbol{r}')}\delta\rho(\boldsymbol{r})\delta\rho(\boldsymbol{r}')\right)\mathrm{d}\boldsymbol{r}'\,\mathrm{d}\boldsymbol{r}. \end{aligned} \tag{2.63}$$

The first term is the standard non-self-consistent energy given by

$$\begin{aligned} E\left[\rho_0(\boldsymbol{r})\right] =& \sum_i^{\text{occ.}}\left\langle\chi_i\left|\hat{h}_i[\rho_0]\right|\chi_i\right\rangle-\frac{1}{2}\int\int\frac{\rho_0(\boldsymbol{r}')\rho_0(\boldsymbol{r})}{|\boldsymbol{r}-\boldsymbol{r}'|}\,\mathrm{d}\boldsymbol{r}\,\mathrm{d}\boldsymbol{r}' \\ &+E_{\mathrm{XC}}\left[\rho_0(\boldsymbol{r})\right]-\int V_{\mathrm{XC}}\left[\rho_0(\boldsymbol{r})\right]\rho(\boldsymbol{r})\,\mathrm{d}\boldsymbol{r}+E_{\mathrm{II}}, \end{aligned} \tag{2.64}$$

and the second part is the sum of the second-order corrections to the Coulomb and exchange-correlation energies due to the charge fluctuation. The non-self-consistent part is solved as normal to find the shape of the orbitals χ_i. Rather than find the density fluctuation $\delta\rho$ directly a set of partial atomic charges are sought instead. These quantities are connected by the expression

$$\Delta q_A \approx \int_{V_A}\delta\rho(\boldsymbol{r})\,\mathrm{d}\boldsymbol{r}, \tag{2.65}$$

where Δq_A are the partial atomic charges and V_A the atomic volumes. The atomic volumes are not defined explicitly but implicitly by the partial atomic charges found using Mulliken population analysis [18]. By normalising the atomic densities with respect to the atomic volumes,

$$\int_{V_A}\delta\rho_A(\boldsymbol{r})\,\mathrm{d}\boldsymbol{r}=1, \tag{2.66}$$

they can be related to the total density using

$$\delta\rho=\sum_A\Delta q_A\delta\rho_A. \tag{2.67}$$

This allows the double integral in equation 2.63 to be decomposed into a sum of double integrals over atomic volumes. This leads to the expression

$$E_{\text{2nd Order}}=\sum_{AB}\frac{1}{2}\Delta q_A\Delta q_B\int_{V_A}\int_{V_B}\left(\frac{1}{|\boldsymbol{r}-\boldsymbol{r}'|}+\frac{\partial^2 E_{\mathrm{XC}}\left[\rho_0\right]}{\partial\rho(\boldsymbol{r})\partial\rho(\boldsymbol{r}')}\right)\delta\rho_A(\boldsymbol{r})\delta\rho_B(\boldsymbol{r}')\,\mathrm{d}\boldsymbol{r}'\,\mathrm{d}\boldsymbol{r}. \tag{2.68}$$

When $A=B$ the integral can be approximated by the Hubbard parameter U. This can be shown by expanding atomic energy in terms of charge to second order to get

$$E(Q)\approx E_0+\frac{\partial E}{\partial Q}Q+\frac{1}{2}\frac{\partial^2 E}{\partial Q^2}Q^2, \tag{2.69}$$

where E_0 is the energy of the neutral atom and Q is charge. The change in energy of the

atom due to gaining an electron, when $Q = -1$, is the electron affinity

$$E_{\text{ea}} \approx \frac{\partial E}{\partial Q} + \frac{1}{2}\frac{\partial^2 E}{\partial Q^2} \tag{2.70}$$

and when an electron is removed, $Q = +1$ the energy change is the negative of the ionisation energy E_{i},

$$-E_{\text{i}} \approx -\frac{\partial E}{\partial Q} + \frac{1}{2}\frac{\partial^2 E}{\partial Q^2}. \tag{2.71}$$

Using the Mulliken definition of electronegativity,

$$\chi \approx \frac{1}{2}\left(E_{\text{i}} + E_{\text{ea}}\right), \tag{2.72}$$

and, noting that in this instance χ is the electronegativity and not an orbital as previously defined, with the definition of the Hubbard parameter

$$U \approx E_{\text{i}} - E_{\text{ea}} \tag{2.73}$$

it is possible, by substituting the expressions for E_{i} and E_{ea}, to show that

$$\chi = -\frac{\partial E}{\partial Q} \tag{2.74}$$

and

$$U = \frac{\partial^2 E}{\partial Q^2}. \tag{2.75}$$

Hence, U can replace the second derivative in equation 2.68 when $A = B$.

At large internuclear distances the exchange-correlation part of equation 2.68 will tend to zero leaving the other term which is a classical Coulomb interaction energy for point charges. The classical Coulomb potential will not produce the correct behaviour for two electrons on the same atom at which the second-order correction should be equal to the Hubbard parameter. As the internuclear distance tends to zero a predetermined analytic function, based on integrals assuming spherically symmetric charge distributions, is used [18]. This allows the second-order correction to be written as

$$E_{\text{2nd Order}} = \frac{1}{2}\sum_{AB}\gamma_{AB}\Delta q_A \Delta q_B, \tag{2.76}$$

using the expression for γ as suggested by Koskinen [17]:

$$\gamma_{AB} = \begin{cases} U_A, & \text{if } A = B, \\ \dfrac{\operatorname{erf}(C_{AB} r_{AB})}{r_{AB}} & \text{if } A \neq B, \end{cases} \tag{2.77}$$

where r_{AB} is the internuclear distance between atoms A and B and $\operatorname{erf}(x)$ is the Gauss er-

ror function. The function C_{AB} is defined using the full width at half maximum (FWHM) for Gaussian distribution functions used for the spherically symmetric charge distributions. The function is

$$C_{AB} = \sqrt{\frac{4\ln 2}{\mathrm{FWHM}_A^2 + \mathrm{FWHM}_B^2}}, \tag{2.78}$$

with the full-width half-maximum values related to the Hubbard parameter by

$$\mathrm{FWHM}_A = \sqrt{\frac{8\ln 2}{\pi}}\frac{1}{U_A}. \tag{2.79}$$

With the second-order correction defined and a set of partial atomic charges found using Mulliken population analysis the total energy can be calculated. However, the partial atomic charges must now be incorporated into the one-electron operators $\hat{h}$ via the nuclear-electron interaction term. This results in the need to generate new orbitals which in turn requires the generation of new partial atomic charges, a process which must be repeated until self-consistency is achieved. This is why this form of DFTB is referred to as self-consistent-charge DFTB (SCC-DFTB). This form of DFTB allows for some charge transfer between the atomic sites which improves on the original non-self-consistent DFTB form by permitting polarisation within simulated molecules. It should be noted that there is no polarisation effect in the charge fluctuations.

The concept of expanding the total energy has been extended further by incorporating a third-order correction term, a method referred to as DFTB3 [19]. By extending the energy of an atom with respect to its charge to third order leads to

$$E(Q) \approx E_0 + \frac{\partial E}{\partial Q}Q + \frac{1}{2}\frac{\partial^2 E}{\partial Q^2}Q^2 + \frac{1}{6}\frac{\partial^3 E}{\partial Q^3}Q^3, \tag{2.80}$$

which in terms of the electronegativity and Hubbard parameter becomes

$$E(Q) \approx E_0 - \chi Q + \frac{1}{2}UQ^2 + \frac{1}{6}\frac{\partial U}{\partial Q}Q^3. \tag{2.81}$$

The third-order correction for the DFTB total energy is thus

$$E_{\text{3rd Order}} \approx \frac{1}{6}\sum_{ABC}\Delta q_A \Delta q_B \Delta q_C \left.\frac{\partial \gamma_{AB}}{\partial q_C}\right|_{q_C^0}, \tag{2.82}$$

which requires the derivative of the gamma function, defined in 2.77, with respect to an atomic partial charge. Although three-center contributions exist it is in the spirit of tight-binding calculations to limit the included terms to two-centre approximations. In

this manner equation 2.82 can be rewritten as

$$E_{\text{3rd Order}} \approx \frac{1}{6}\sum_{A}\Delta q_A \left.\frac{\partial \gamma_{AA}}{\partial q_A}\right|_{q_A^0} + \frac{1}{6}\sum_{A\neq B}\Delta q_A \Delta q_B \left(\Delta q_A \left.\frac{\partial \gamma_{AB}}{\partial q_A}\right|_{q_A^0} + \Delta q_B \left.\frac{\partial \gamma_{AB}}{\partial q_B}\right|_{q_B^0}\right) \tag{2.83}$$

The derivative of γ is calculated by differentiating by parts to get

$$\left.\frac{\partial \gamma_{AB}}{\partial q_A}\right|_{q_A^0} = \left.\frac{\partial \gamma_{AB}}{\partial U_A}\frac{\partial U_A}{\partial q_A}\right|_{q_A^0}. \tag{2.84}$$

The derivative of γ with respect to ∂U can be determined analytically through differentiation of equation 2.77 but the derivative of the Hubbard parameter must be calculated numerically. This is performed by numerical differentiation of the Hubbard parameter calculated at different charge states ($Q = +1$, $Q = 0$ and $Q = -1$) using DFT. The Hubbard parameter is not constant with respect to atomic charge so by including charge dependence on the derivative of the Hubbard parameter it is possible to reproduce the behaviour of partially charged systems with greater accuracy using DFTB3.

All forms of DFTB require careful parametrisation. Parameters are not automatically transferable from one form of DFTB to another. By adding second- and then third-order correction terms it is necessary to recompute the repulsive potentials. This makes comparison of the different flavours of DFTB difficult. A further problem is that parameters must be calculated for every pair of species leading to a quadratic growth in the number of parameters with respect to atomic species. This does not tend to be an issue for a user provided that the necessary parameters are freely available for the atomic species used in their calculations.

DFTB offers an exceptionally fast method for computing molecular and crystal properties using an electronic structure based approach. Systems of several thousand atoms can be simulated making it a useful method for simulating nanostructures. Larger systems can be modelled using molecular mechanics force fields but the accuracy of results generated using such methods is less than those produced using DFTB. Furthermore, DFTB captures electronic behaviour, allowing for the electronic properties of materials to be investigated, which is not possible using molecular mechanics.

2.7 Molecular mechanics

The alternative to electronic structure methods is to ignore the electron orbitals and describe the molecular energy using only the nuclear coordinates. Such models are referred to as molecular mechanics potentials or force fields. This method avoids issues with achieving self-consistent fields and the quantum nature of the electrons. Instead, it uses analytic expressions for the interatomic forces with parameters fitted to experimental data or higher order calculations. This reduces the problem to the Newtonian

mechanics of a system of interacting particles and reduces the computational cost by orders of magnitude. However, such methods generally require knowledge of the input structures and may only provide accurate results close to the equilibrium geometries.

The potential energy of structure as a function of nuclear coordinates is

$$U = f(\boldsymbol{x}), \tag{2.85}$$

where U is the total potential energy of the system and $\boldsymbol{x}$ is the vector of nuclear coordinates. The degrees of freedom $\boldsymbol{x}$ can contain additional variables, such as shell coordinates in a core-shell model, but in this work the variables will only be of the former type. Many potentials use known properties like relaxed bond lengths, steric effects, torsional barriers and vibrational frequencies to provide a method for parametrising the potential. This leads to the natural form for a potential as

$$U = \sum_{\text{Bonds}} f(r_{ij}) + \sum_{\text{Angles}} g(\theta_{ijk}) + \sum_{\text{Dihedrals}} h(\phi_{ijkl}), \tag{2.86}$$

where r_{ij} is the distance between two bonded atoms, θ_{ijk} the angle between three atoms connected by two bonds and ϕ_{ijkl} the angle between two bonds that are connected by a third. The sums occur over all combinations and will contain parameters that depend on the atomic species of the atoms involved.

Many potentials choose to represent the bond stretch function using a harmonic potential,

$$f(r_{ij}) = \frac{1}{2}k(r_{ij} - r_0)^2, \tag{2.87}$$

where k and r_0 are parameters whose value depends on the atoms connected by the bond. This simple harmonic potential produces forces that vary linearly but it can only describe the bond energy accurately when r is close to the equilibrium bond length r_0 and dissociation is not possible. An alternative form is the Morse potential,

$$f(r_{ij}) = D\left(1 - e^{-a(r-r_0)}\right)^2, \tag{2.88}$$

which requires the depth D and width a of the potential along with the equilibrium bond length as predetermined parameters. The benefit of this form is that it better describes the bond energy away from the equilibrium length than a harmonic approximation.

The bond angle term can be represented using a harmonic form but a trigonometric form can also be used [20, 21]. By representing the bond angle potential with

$$g(\theta_{ijk}) = k\left(1 - \cos(n\theta_{ijk})\right) \qquad \text{where} \quad n = 1, 2, 3\ldots \tag{2.89}$$

where k is parametrised dependent on the three atoms and how they are connected, it is possible to better reproduce the potential energy due to large angular deformations

compared to a simple harmonic form [20]. The above expression is based on a Fourier expansion of the angular potential and additional sine and cosine terms can be included at the cost of more parameter fitting.

Torsional barriers have relatively low energies so it is very common to use Fourier expansions to represent the dihedral torsion term. In this case

$$h(\phi_{ijkl}) = k \sum_{n=0}^{m} C_n \cos(n\phi_{ijkl}) \tag{2.90}$$

allows for multiple minima and torsional barriers to be included in the forcefield.

The terms described above are the most common type of bonded interactions included in molecular mechanics potentials but they are usually not used by themselves. Non-bonded interactions, such as van der Waals and electrostatic interactions, are incorporated into potentials by use of appropriate terms. The van der Waals potentials are generally included by way of a Lennard-Jones potential [22],

$$U_{vdW} = D\left(\left(\frac{r_0}{r_{ij}}\right)^{12} - 2\left(\frac{r_0}{r_{ij}}\right)^{6}\right), \tag{2.91}$$

which is a function of interatomic distance r_{ij} and the fitted parameters D and r_0. The classical Coulomb potential

$$U_{\text{Coulomb}} = \frac{q_i q_j}{4\pi\epsilon_0 r_{ij}} \tag{2.92}$$

is employed for electrostatic interactions between atoms i and j with partial atomic charges q_i and q_j and interatomic separation r_{ij}.

Potentials may be supplemented with additional terms or simplified by removing some of the terms discussed. Many systems have been investigated using only Morse or Lennard-Jones potentials calculated between all atom pairs. However, the basic forms shown above are used by a number of readily available force fields in many simulation packages [23, 24, 21].

An alternative method for describing interactions between atoms are bond order potentials. These potentials simulate the interactions between atoms based on the distance between atoms and their coordination numbers. This methodology has been used to build a number of potentials for carbon that have become increasingly popular for simulating carbon nanostructures. Of particular note is the Tersoff-Brenner potential [25, 26] that has the form

$$U_{ij} = f_C(r_{ij})\left[a_{ij} f_R(r_{ij}) + b_{ij} f_A(r_{ij})\right], \tag{2.93}$$

where the functions f_R and f_A determine the energy due to repulsive and attractive forces between the atoms i and j as functions of their separation r_{ij}. The cutoff function $f_C(r_{ij})$ allows the potential to be limited to nearest neighbours and the functions a and b modify the strength of the repulsion or attraction based on the local environment of

the atoms. The attractive and repulsive functions are usually

$$f_R(r) = A\exp(-\lambda_1 r), \tag{2.94}$$

$$f_A(r) = -B\exp(-\lambda_2 r), \tag{2.95}$$

where r is the distance between the atoms and λ_1, λ_2, A and B are fitted parameters. When added together these two functions form a Morse type potential. The function b_{ij}, known as the bond order function, in Tersoff's original paper is

$$b_{ij} = \left(1 + \beta^n \zeta_{ij}^n\right)^{-\frac{1}{2n}}, \tag{2.96}$$

where β and n are parameters and the function

$$\zeta_{ij} = \sum_{k\neq i,j} f_C(r_{ik}) g(\theta_{ijk}) \exp\left[\lambda^3 (r_{ij} - r_{ik})^3)\right], \tag{2.97}$$

provides modification of the attractive potential due to third atoms denoted by the index k. The function $g(\theta_{ijk})$ is a function of the angle between the connecting lines between atoms i and j and i and k, which allows for shielding behaviour. The potential uses

$$g(\theta) = 1 + \left(\frac{c}{d}\right)^2 - \frac{c^2}{d^2 + (h - \cos\theta_{ijk})^2}, \tag{2.98}$$

where c, d and h are fitted parameters, to provide shielding when a third atom lies between the atoms i and j. The function

$$a_{ij} = (1 + \alpha^n \eta_{ij}^n)^{-\frac{1}{2n}}, \quad \text{with} \tag{2.99}$$

$$\eta_{ij} = \sum_{k\neq i,j} f_C(r_{ik}) \exp\left[\lambda^3 (r_{ij} - r_{ik})^3\right], \tag{2.100}$$

where α is another parameter, is suggested for modifying the repulsive potential. However, in the original work it is suggested that α be taken as 0 which leads to a_{ij} having a constant value of 1. The original potential was developed and parametrised for pure silicon but in later papers parameters were devolped for carbon [27] and some type III-V semiconductors [28, 29].

The basic potential for carbon fails to account for conjugated bonds leading to spurious results for finite graphene based structures terminated with hydrogen. This was recognised later and a correction term introduced which corrected for conjugated and nonconjugated bonds [26]. A later version of this potential, known as the reactive empirical bond order potential (REBO), also modifies the attractive and repulsive functions [30]. In REBO the repulsive function is replaced by a screened Coulomb potential of the form

$$f_R(r) = \left(1 + \frac{Q}{r}\right) A\exp(-\alpha r), \tag{2.101}$$

where r is interatomic distance and Q is a fitted parameter. The Q/r term allows the potential to tend to infinity as the distance goes to zero instead of to a finite value as occurred in equation 2.94. The attractive term is replaced with a more complex superposition of exponential functions,

$$f_A(r) = \sum_{n=1}^{3} B_n \exp(-\beta_n r), \tag{2.102}$$

where the three values of β are new parameters to be determined during fitting. The REBO potential also used an expanded database of properties to use in the fitting to improve the parametrisation. These adjustments improved the predicted bond lengths, energies and force constants of the potential for both carbon and hydrocarbon structures.

Further developement of the potential introduced terms to provide torsion and intermolecular effects, that were previously missing, led to the adaptive intermolecular REBO potential or AIREBO [31]. The intermolecular term is a Lennard-Jones potential but uses a range dependant adaptive switching function. The switching range varies based on the adjacent atoms types and how the atoms involved are bonded. The torsional term is similar to the those used in the empirical potentials and provides the torsional behaviour that was missing in the earlier potentials.

Other potentials have also introduced long range potential functions such as the long range carbon bond order potential (LCBOP) [32]. Here Morse potentials are used to reproduce the interplanar van der Waals bonding in graphite. This potential was updated to LCBOP II [33] by introducing a correction term to improve how the potential dealt with unpaired electrons and a torsion term into the bond order function (b_{ij} in function 2.96).

As alternative bond order dependant potential is ReaxFF [34]. This potential writes the system energy as

$$\begin{aligned} U_{\text{System}} = E_{\text{BO}} + E_{\text{Over}} + E_{\text{Under}} + E_{\text{Valence}} + E_{\text{Penalty}} \\ + E_{\text{Torsion}} + E_{\text{Conjugation}} + E_{\text{vdW}} + E_{\text{Coulomb}}, \end{aligned} \tag{2.103}$$

where E_{BO} is a bond potential, E_{Over} and E_{Under} corrects for over or under binding, E_{Valence} accounts for deviations in the bond angle energy, E_{Penalty} is a penalty term to correct the bond angle energy for certain structures, $E_{\text{Conjugation}}$ incorporates conjugation effects and E_{Torsion}, E_{vdW} and E_{Coulomb} are torsion, van de Waals and Coulomb terms similar to those introduced previously.

All terms except the van der Waals and Coulomb potentials have some dependence on the bond order. The bond order is calculated as a function of bond length using

$$B_{ij} = \sum_{n=1}^{V} \exp\left[a_n \left(\frac{r_{ij}}{r_0}\right)^{b_n}\right], \tag{2.104}$$

where n indicates bond order and varies up to the maximum number of bonds V, r_{ij} is the interatomic separation and all other parameters are fitted for specific atom pairs. This allows B to vary continuously from V to zero over a range of bond lengths. This provides the mechanism for simulating reactions between atoms as bonds are made or broken. The actual forms of the energy terms tend to be complicated and dependent on the environment of the atoms involved in the calculation so are not given here.
Molecular mechanics potentials offer a computationally efficient method for simulating large numbers of atoms. Most potentials are built such that first, second and possibly higher derivatives can be included explicitly for use in function minimisation methods or molecular dynamics simulations. The more basic potentials require the molecular structures to be provided by the user and they generally can not model reactions without additional user input. Bond order potentials have been developed to simulate reactions and phase changes for carbon based materials but these are dependent on complex mathematical forms involving large parameter sets.

2.8 Software

2.8.1 Gaussview

Gaussview is a graphical user interface for the Gaussian package that provides a set of tools for building and viewing molecules. It provides access to most of the features of Gaussian through menus and dialogues. It was used in this work for generating initial geometries form some of the investigated structures.

2.8.2 Gaussian09

Gaussian09 [35] is a quantum chemistry package that was developed for AO basis sets with calculations performed in real space. It can be used for periodic calculations although this is uncommon as plane wave DFT packages exist for this purpose (see CASTEP). Gaussian09 offers a number of different calculation types including Hartree-Fock (HF), density-functional theory (DFT) and a number of post-HF methods including Möller-Plesset perturbation (MP2 and MP4), configuration interaction, multi-reference self-consistent-field methods (including complete-active-space self-consistent-field) and coupled-cluster methods.

2.8.3 CASTEP

CASTEP [36] is a plane-wave DFT package that uses pseudopotentionals to perform solid state calculations of crystal structures. The DFT calculation is mostly performed in reciprocal space using a plane-wave basis set. The basis set size can be increased by increasing the cutoff energy for the plane waves which provides a simple method for testing for basis set convergence. The drawbacks to performing the calculation is

reciprocal space include the computational cost of applying certain types of exchange-correlation functionals and the need to simulate vacuum gaps when dealing with 1D and 2D systems. Functionals containing exact exchange, using the exchange integral of the Hartree-Fock method, are particularly costly in this method.

2.8.4 DFTB+

DFTB+ [37] uses the density-functional tight-binding approximation with predetermined parameter sets to calculate the electronic structure of crystals and molecules. The approximations made in this method, the parametrised potentials and matrix elements and the short range cutoff of the interactions, trades calculation accuracy for speed, allowing much larger systems of atoms to be considered than DFT.

2.8.5 GULP

GULP [38] is a molecular mechanics/dynamics package which provides considerable choice of empirical potentials, the ability to model periodic systems and various calculation methods. GULP can provide reasonable values for mechanical properties close to a systems equilibrium and can handle very large systems of atoms.

2.8.6 LAMMPS

LAMMPS [39] is another molecular mechanics/dynamics package containing many molecular mechanics potentials and fulfils the same roles as GULP.

2.8.7 MATLAB

Matlab [40] is a general purpose maths programming language with a wide variety of tools from file I/O to plotting to symbolic mathematics. A number of tools for generating input geometries, plotting data, converting input files and performing analyses were coded in Matlab for use in this project.

Bibliography

[1] E. Schrödinger. An Undulatory Theory of the Mechanics of Atoms and Molecules. *Physical Review*, 28(6):1049–1070, 1926.

[2] M. Born and R. Oppenheimer. Zur Quantentheorie der Molekeln. *Annalen der Physik*, 389(20):457–484, 1927.

[3] W. Pauli. Über den Zusammenhang des Abschlusses der Elektronengruppen im Atom mit der Komplexstruktur der Spektren. *Zeitschrift für Physik*, 31(1):765–783, 1925.

[4] J. C. Slater. The Theory of Complex Spectra. *Physical Review*, 34(10):1293–1322, 1929.

[5] J. C. Slater. Atomic shielding constants. *Physical Review*, 36(1):57–64, 1930.

[6] D. R. Hartree. The Wave Mechanics of an Atom with a Non-Coulomb Central Field. Part I. Theory and Methods. *Mathematical Proceedings of the Cambridge Philosophical Society*, 24(01):89, 1928.

[7] V. Fock. Näherungsmethode zur Lösung des quantenmechanischen Mehrkörperproblems. *Zeitschrift für Physik*, 61(1-2):126–148, 1930.

[8] A. Szabo and N. S. Ostlund. *Modern Quantum Chemistry: introduction to advanced electronic structure theory*. Dover Publications, Inc., 1989.

[9] C. C. J. Roothaan. New Developments in Molecular Orbital Theory. *Reviews of Modern Physics*, 23(2):69–89, 1951.

[10] G. G. Hall. The Molecular Orbital Theory of Chemical Valency. VIII. A Method of Calculating Ionization Potentials. *Proceedings of the Royal Society A: Mathematical, Physical and Engineering Sciences*, 205(1083):541–552, 1951.

[11] C. Møller and M. S. Plesset. Note on an Approximation Treatment for Many-Electron Systems. *Physical Review*, 46(7):618–622, 1934.

[12] E. Schrödinger. Quantisierung als eigenwertproblem. *Annalen der Physik*, 385(13):437–490, 1926.

[13] P. Hohenberg and W. Kohn. Inhomogeneous Electron Gas. *Physical Review*, 136(3B):B864–B871, 1964.

[14] W. Kohn and L. J. Sham. Self-Consistent Equations Including Exchange and Correlation Effects. *Physical Review*, 140(4A):A1133–A1138, 1965.

[15] W. M. C. Foulkes and R. Haydock. Tight-binding models and density-functional theory. *Physical Review B*, 39(17):12520–12536, 1989.

[16] D. Porezag, T. Frauenheim, T. Köhler, G. Seifert, and R. Kaschner. Construction of tight-binding-like potentials on the basis of density-functional theory: Application to carbon. *Physical Review B*, 51(19):12947–12957, 1995.

[17] P. Koskinen and V. Mäkinen. Density-functional tight-binding for beginners. *Computational Materials Science*, 47(1):237–253, 2009.

[18] M. Elstner, D. Porezag, G. Jungnickel, J. Elsner, M. Haugk, T. Frauenheim, S. Suhai, and G. Seifert. Self-consistent-charge density-functional tight-binding method for simulations of complex materials properties. *Physical Review B*, 58(11):7260–7268, 1998.

[19] M. Gaus, Q. Cui, and M. Elstner. DFTB3: Extension of the Self-Consistent-Charge Density-Functional Tight-Binding Method (SCC-DFTB). *Journal of Chemical Theory and Computation*, 7(4):931–948, 2011.

[20] V. S. Allured, C. M. Kelly, and C. R. Landis. SHAPES empirical force field: new treatment of angular potentials and its application to square-planar transition-metal complexes. *Journal of the American Chemical Society*, 113(1):1–12, 1991.

[21] A. K. Rappe, C. J. Casewit, K. S. Colwell, W. A. Goddard, and W. M. Skiff. UFF, a full periodic table force field for molecular mechanics and molecular dynamics simulations. *Journal of the American Chemical Society*, 114(25):10024–10035, 1992.

[22] J. E. Jones. On the Determination of Molecular Fields. II. From the Equation of State of a Gas. *Proceedings of the Royal Society A: Mathematical, Physical and Engineering Sciences*, 106(738):463–477, 1924.

[23] B. R. Brooks, R. E. Bruccoleri, B. D. Olafson, D. J. States, S. Swaminathan, and M. Karplus. CHARMM: A program for macromolecular energy, minimization, and dynamics calculations. *Journal of Computational Chemistry*, 4(2):187–217, 1983.

[24] S. L. Mayo, B. D. Olafson, and W. A. Goddard. DREIDING: a generic force field for molecular simulations. *The Journal of Physical Chemistry*, 94(26):8897–8909, 1990.

[25] J. Tersoff. New empirical approach for the structure and energy of covalent systems. *Physical Review B*, 37(12):6991–7000, 1988.

[26] D. W. Brenner. Empirical potential for hydrocarbons for use in simulating the chemical vapor deposition of diamond films. *Physical Review B*, 42(15):9458–9471, 1990.

[27] J. Tersoff. Empirical interatomic potential for carbon, with applications to amorphous carbon. *Physical Review Letters*, 61(25):2879–2882, 1988.

[28] R. Smith. A semi-empirical many-body interatomic potential for modelling dynamical processes in gallium arsenide. *Nuclear Instruments and Methods in Physics Research Section B: Beam Interactions with Materials and Atoms*, 67(1-4):335–339, 1992.

[29] K. Albe, W. Möller, and K.-H. Heinig. Computer simulation and boron nitride. *Radiation Effects and Defects in Solids*, 141(1-4):85–97, 1997.

[30] D. W. Brenner, O. a. Shenderova, J. a. Harrison, S. J. Stuart, B. Ni, and S. B. Sinnott. A second-generation reactive empirical bond order (REBO) potential energy expression for hydrocarbons. *Journal of Physics: Condensed Matter*, 14(4):783–802, 2002.

[31] S. J. Stuart, A. B. Tutein, and J. A. Harrison. A reactive potential for hydrocarbons with intermolecular interactions. *The Journal of Chemical Physics*, 112(2000):6472–6486, 2000.

[32] J. H. Los and A. Fasolino. Intrinsic long-range bond-order potential for carbon: Performance in Monte Carlo simulations of graphitization. *Physical Review B*, 68(2):024107, 2003.

[33] J. H. Los, L. M. Ghiringhelli, E. J. Meijer, and A. Fasolino. Improved long-range reactive bond-order potential for carbon. I. Construction. *Physical Review B*, 72(21):214102, 2005.

[34] A. C. T. van Duin, S. Dasgupta, F. Lorant, and W. A. Goddard. ReaxFF: A Reactive Force Field for Hydrocarbons. *The Journal of Physical Chemistry A*, 105(41):9396–9409, 2001.

[35] M. J. Frisch, G. W. Trucks, H. B. Schlegel, G. E. Scuseria, M. A. Robb, J. R. Cheeseman, G. Scalmani, V. Barone, B. Mennucci, G. A. Petersson, H. Nakatsuji, M. Caricato, X. Li, H. P. Hratchian, A. F. Izmaylov, J. Bloino, G. Zheng, J. L. Sonnenberg, M. Hada, M. Ehara, K. Toyota, R. Fukuda, J. Hasegawa, M. Ishida, T. Nakajima, Y. Honda, O. Kitao, H. Nakai, T. Vreven, J. A. Montgomery, Jr., J. E. Peralta, F. Ogliaro, M. Bearpark, J. J. Heyd, E. Brothers, K. N. Kudin, V. N. Staroverov, T. Keith, R. Kobayashi, J. Normand, K. Raghavachari, A. Rendell, J. C. Burant, S. S. Iyengar, J. Tomasi, M. Cossi, N. Rega, J. M. Millam, M. Klene, J. E. Knox, J. B. Cross, V. Bakken, C. Adamo, J. Jaramillo, R. Gomperts, R. E. Stratmann, O. Yazyev, A. J. Austin, R. Cammi, C. Pomelli, J. W. Ochterski, R. L. Martin, K. Morokuma, V. G. Zakrzewski, G. A. Voth, P. Salvador, J. J. Dannenberg, S. Dapprich, A. D. Daniels, O. Farkas, J. B. Foresman, J. V. Ortiz, J. Cioslowski, and D. J. Fox. Gaussian 09, Revision D.01, 2013. Gaussian Inc. Wallingford CT.

[36] S. J. Clark, M. D. Segall, C. J. Pickard, P. J. Hasnip, M. I. J. Probert, K. Refson, and M. C. Payne. First principles methods using CASTEP. *Zeitschrift für Kristallographie - Crystalline Materials*, 220(5/6):567–570, 2005.

[37] B. Aradi, B. Hourahine, and T. Frauenheim. DFTB+, a sparse matrix-based implementation of the DFTB method. *Journal of Physical Chemistry A*, 111(26):5678–5684, 2007.

[38] J. D. Gale. GULP: A computer program for the symmetry-adapted simulation of solids. *Journal of the Chemical Society, Faraday Transactions*, 93(4):629–637, 1997.

[39] S. Plimpton. Fast Parallel Algorithms for Short-Range Molecular Dynamics. *Journal of Computational Physics*, 117(1):1–19, 1995.

[40] *MATLAB 2017a*. The MathWorks Inc., Natick, Massachusetts, US, 2017.

Chapter 3

Piezoelectric effects in boron nitride nanotubes

The principle aim of the work in this chapter was to build and test a computational method capable of capturing piezoelectric effects using a pre-existing molecular modelling method called atomistic finite element method (AFEM). This method uses a space frame structure to describe molecules which allows conventional finite element packages to carry out atomistic simulations. This is accomplished by treating bonds as beams that connect atoms with the beam properties determined from force constants taken from molecular mechanics potentials. The work presented here attempts to expand this method by incorporating piezoelectric effects so it can be used to calculate the piezoelectric coupling tensor for a specified nanostructure. This chapter is based on work previously submitted as my extended project and published, in part, in conference proceedings and in more detail in a journal paper where I was lead author. The work was presented at the 24th International Congress of Theoretical and Applied Mechanics [1] and the journal paper was published in Nanotechnology where it was included in the 2017 highlights for the journal [2].

3.1 Introduction

AFEM was first used to model carbon nanotubes by Li and Chou [3] in 2003 and has since been used to model graphene, hexagonal boron nitride, boron nitride nanotubes and zirconia nanotubes by various authors [4, 5, 6, 7]. The method has even been applied to deoxyribonucleic acid as a way to study the study the mechanics of DNA [8]. The method is based on the concept of taking energy equivalence between the strain energy of deformed beams and the deformation energy of molecular bonds as given by molecular mechanics potential models. The chemical bonds between atoms are modelled as beams which can stretch, twist, bend and shear allowing the application of standard structural finite element techniques to determine the response of nanostructures to an applied force

or deformation. Li and Chou demonstrated this method using both static [9] and dynamic simulations [10].

Much work using this method and related formulations have adopted different element types to model the molecular bonds. Meo and Rossi used non-linear spring elements and torsional spring elements to model bond extension and angular deformation properties of carbon-carbon bonds in graphene and carbon nanotubes [11]. Adhikari et al. used the same method as Li and Chou to model DNA with the addition of elastic spar elements for the hydrogen bonds [8]. Boldrin et al. [12] used the same principles as the Li and Chou authors but used deep shear Timoshenko type beam elements to calculate the mechanical properties of boron nitride nanosheets. These beam elements differ from the slender Euler-Bernoulli elements used elsewhere by including shear deformation, a deformation mode that is relevant to beams with a low length to width ratio. It can be shown that this ratio is low for the effective beams employed in the atomistic finite element method. Boron nitride structures subject to an external electric field have been modelled by Zhang et al. using the Li and Chou method [6]. However, their choice of atomic charges is based on a simplified ionic model that does not necessarily represent realistic charge density distributions. Their assumption of charges of $+3$ e and -3 e, for the boron and nitrogen atoms respectively, is intuitive but it is not consistent with results from population analysis of *ab initio* quantum mechanical calculations [13, 14]. Nasdala et al. developed a multi element approach (MDFEM) that uses different element types to represent the force terms in the underlying molecular mechanics model [15]. To account for different types of forces, the elements consist of two node spring elements to carry bond elongation, three node coupled bond elements to carry angular deformation and four node elements to carry torsion. Although this method is more complicated than the method proposed by Li and Chou, a single bond will require many elements in order to capture the different deformation mechanisms, it only requires three translational degrees of freedom at each node instead of six. Another somewhat more simplified multi-element approach is that of Giannopoulos et al. which uses one type of element to represent bond stretching and another element which connects two atoms that share a bond with a common third atom to carry the angular and torsional load [16].

The atomistic finite element method has been employed almost solely for the purpose of examining the stiffnesses of molecular structures. Moreover, the initial geometries used have been idealised nanotube geometries, where all atoms lie on the surface of a cylinder, as opposed to energy minimised structures. However, we seek to add additional functionality to calculate piezoelectric properties, such as those of boron nitride nanotubes. This requires effective charges to be calculated for the atoms based on the molecular geometry and structure and a family of methods that provide a rapid method for effective charge calculations have been developed from the premise of electronegativity equalization [17, 18, 19, 20].

Nanotubes are one of several intriguing synthetic molecular structures produced over the

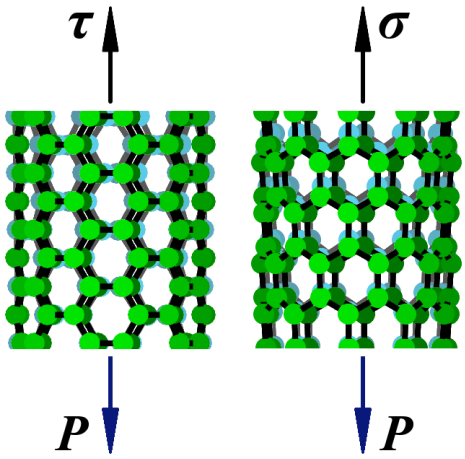

Figure 3.1: A diagram showing the resultant dipole vector, $\boldsymbol{P}$, due to applied stress, the left image shows a torque, $\boldsymbol{\tau}$, (assuming the right hand rule) and the right image shows axial stress, $\boldsymbol{\sigma}$. The green atoms show the relaxed state and the blue atoms show the (exaggerated) response to an applied stress.

last few decades. They were first produced composed entirely of carbon atoms [21], the well known carbon nanotube (CNT). This discovery lead to studies of other potential candidate materials with the potential to form nanotubes. One of the most promising was boron nitride as it was known to form both cubic and hexagonal polymorphs, as an almost exact III-V analogue of carbon. Boron nitride nanotubes (BNNTs) were predicted in 1994 [22] and shown to be semiconductors with a large band gap. The first successful synthesis of BNNTs was subsequently reported in 1995 by Chopra et al. [23] using the plasma discharge method. In 2003 Mele and Král [24] used a Berry phase approach to predict piezoelectric properties of BNNTs caused by symmetry breaking of the structure under deformation. They showed that boron nitride nanotubes would generate a coupled electric dipole dependant on their chirality and the loading type to which they were subjected. Armchair nanotubes subjected to torsion would generate a coupled electric dipole, while zigzag nanotubes would respond to elongation (as shown in figure 3.1). Furthermore, their work showed how the strength of the coupling varied with chiral angle for a given type of loading. The predicted values for the piezoelectric coupling tensor entries suggest BNNTs are better piezoelectric materials than polymer piezoelectric materials [25]. Their piezoelectric properties coupled with their axial stiffness offers potential applications in composites [26] and nano-electro-mechanical devices (NEMs) [27]. A further benefit of boron nitride materials is their large neutron absorption cross sectional area, adding to their value in space vehicle applications [26].

BNNTs provide an excellent test structure for testing an extended AFEM which incorporates piezoelectric effects. Calculating the piezoelectric properties of BNNTs requires that the AFEM accurately reproduces the deformation of the structure of BNNTs under

both tensile and torsional loading. Predicted piezoelectric coupling coefficients can be compared to readily available values from the literature, which simplifies validation. The necessary data to build the AFEM model are also widely available from the literature.
The work presented here seeks to determine the piezoelectric tensor coefficients of boron nitride nanotubes of a variety of chiralities using the atomistic finite element method and a molecular mechanics energy minimisation approach. The dependence of the piezoelectric properties of BNNTs on the atomic displacements makes this a good test of the atomistic finite element method. The work compares the results of the atomistic finite element method with those of molecular mechanics simulations of the same structures to highlight the differences in the outcomes from the different simulation methods.

3.2 Methods

3.2.1 Atomistic Finite Element Method

The atomistic finite element method seeks to model molecular bonds using beam theory and the material and geometric properties of the beams have to be defined. The properties of the beams are deduced from empirical force models developed for molecular mechanics simulations. Common empirical force models describes the structural energy of a molecule using

$$U_{\text{Total}} = \sum_{\text{Bonds}} U_{ij} + \sum_{\text{Angles}} U_{ijk} + \sum_{\text{Torsions}} U_{ijkl} + \sum_{\text{Pairs}} U_{\text{vdW}} + U_{\text{Coulomb}}. \tag{3.1}$$

U_{ij} is the bond stretch energy and is the change in energy due to the change in length of the bond between between atoms i and j. U_{ijk} is the bond angle energy and is the change in energy due to the change in angle between bonds ij and jk where atom j is common to both bonds. U_{ijkl} is the torsion energy and is the change in energy due to the change in angle between bonds ij and kl which are connected by the bond jk. U_{vdW} and U_{Coulomb} are van der Waals and electrostatic energy respectively and are considered non-bonded energy terms as they are calculated for pairs of atoms which lie within a certain range of each other. The van der Waals and electrostatic terms have no counterpart in beam deformation and are neglected in the atomistic finite element method. These force models can use linear relationships between force and displacement or they can use nonlinear relationships such as Morse potentials and truncated Fourier series. It is possible to approximate, using Taylor series, these nonlinear potentials as linear at least close to equilibrium bond lengths, angles and dihedral angles thus allowing the determination of properties of the modelled structure due to small strains.
The linearised force coefficients can then be equated to the structural properties of beams using [3]

$$U_{\text{Extend}} = \frac{1}{2} k_{ij} \Delta r_{ij}^2 = \frac{EA}{2L} \Delta r_{ij}^2, \tag{3.2}$$

$$U_{\text{Dihedral}} = \frac{1}{2}k_{ijkl}\Delta\phi_{ijkl}^2 = \frac{GJ}{2L}\Delta\phi_{ijkl}^2, \tag{3.3}$$

and using either

$$U_{\text{Angle}} = \frac{1}{2}k_{ijk}\Delta\theta_{ijk}^2 = \frac{EI}{2L}\Delta\theta_{ijk}^2, \tag{3.4}$$

or

$$U_{\text{Angle}} = \frac{1}{2}k_{ijk}\Delta\theta_{ijk}^2 = \frac{EI}{2L}\frac{4+\Phi}{1+\Phi}\Delta\theta_{ijk}^2. \tag{3.5}$$

Here, $\Delta r_{ij}, \Delta\theta_{ijk}$ and $\Delta\phi_{ijkl}$ are the bond elongation, angular and dihedral deformations respectively and are determined from the difference between their deformed values and their relaxed values which were calculated by minimising the energy of the molecule. The force constants k_{ij}, $kijk$ and k_{ijkl} define the relationship between the different deformations and the change in energy. E, A, I, L, G and J are the material and geometric properties of beams, namely the Young's modulus, cross sectional area, second moment of area, length, shear modulus and angular moment of area respectively. The length of the beam is the relaxed length of the molecular bond and the beam cross section is taken as a solid circle to provide symmetric bending properties which gives $A = \pi r^2$, $I = \pi r^4/4$ and $J = \pi r^4/2$. Finally, Φ in equation 3.5 is the shear deformation constant and is given by

$$\Phi = \frac{12EI}{GA_sL^2}, \tag{3.6}$$

where $A_s = A/\kappa$ is the shear area and κ is the shear correction factor, for which there are several formulations available, such as that by Cowper [28],

$$\kappa = \frac{6(1+\nu)}{7+6\nu}, \tag{3.7}$$

where ν is the Poisson's ratio of the hypothetical material of the beam representing the atomic interactions.

The choice of beam model determines whether equation 3.4 or 3.5 is used (equation 3.4 for slender beams and 3.5 for deep shear beams) and in turn affects the need for determining the beam radius and Poisson's ratio. In the slender beam, also referred to as an Euler-Bernoulli beam, model there is no need to determine a Poisson's ratio or radius as the molecular mechanics derived constants can be used directly to construct the entries in the element stiffness matrix [3]. The radii of these beams can be calculated by combining equations 3.2 and 3.4 substituting appropriate functions of radius for the cross sectional area and second moment of area for a solid cylindrical tube and then solving for the radius to give

$$r = \sqrt{\frac{4k_{ijk}}{k_{ij}}}. \tag{3.8}$$

The radius of the beam produced using this beam model results in a significant radius to length ratio which in standard beam theory requires the use of a deep shear, Timoshenko

type beam model. Euler-Bernoulli slender beams have been used in previous work with apparent success so whether one needs to be concerned with deep shear for modelling molecular bonds remains an open question.

The deep shear beam model requires calculation of the shear deformation constant and the shear correction factor which requires finding appropriate values for radius and Poisson's ratio. This is achieved by substituting the appropriate functions of radius for the area, second moment of area and polar moment of area into equations 3.2, 3.3, 3.5 and 3.6 to give

$$\frac{1}{2}k_{ij}\Delta r_{ij}^2 = \frac{E\pi r^2}{2L}\Delta r_{ij}^2, \tag{3.9}$$

$$\frac{1}{2}k_{ijkl}\Delta\phi_{ijkl}^2 = \frac{G\pi r^4}{4L}\Delta\phi_{ijkl}^2, \tag{3.10}$$

$$\frac{1}{2}k_{ijk}\Delta\theta_{ijk}^2 = \frac{E\pi r^4}{8L}\frac{4+\Phi}{1+\Phi}\Delta\theta_{ijk}^2 \quad \text{where} \tag{3.11}$$

$$\Phi = \frac{3E\pi r^2}{GL^2}\frac{6(1+\nu)}{7+6\nu}, \tag{3.12}$$

using the shear correction factor in equation 3.7. Solving equations 3.9 and 3.10 for E and G one finds

$$E = \frac{k_{ij}L}{\pi r^2} \quad \text{and} \tag{3.13}$$

$$G = \frac{2k_{ijkl}L}{\pi r^4}, \tag{3.14}$$

$$\tag{3.15}$$

which can then be substituted into equations 3.11 and 3.12 to give

$$\frac{1}{2}k_{ijk}\Delta\theta_{ijk}^2 = \frac{k_{ij}r^2}{8}\frac{4+\Phi}{1+\Phi}\Delta\theta_{ijk}^2 \quad \text{and} \tag{3.16}$$

$$\Phi = \frac{3k_{ij}r^4}{2k_{ijkl}L^2}\frac{6(1+\nu)}{7+6\nu}. \tag{3.17}$$

Substituting 3.17 into 3.16 and solving for k_{ijk} yields

$$k_{ijk} = \frac{k_{ij}r^2}{4}\frac{4+\frac{9k_{ij}r^3(1+\nu)}{k_{ijkl}L^2(7+6\nu)}}{1+\frac{9k_{ij}r^3(1+\nu)}{k_{ijkl}L^2(7+6\nu)}} \tag{3.18}$$

which can be rearranged to the more readable form

$$k_{ijk} = \frac{k_{ij}r^2}{4}\frac{\left(9k_{ij}r^4\left(1+\nu\right)+4l^2k_{ijkl}\left(6\nu+7\right)\right)}{\left(9k_{ij}r^4(1+\nu)+l^2k_{ijkl}(6\nu+7)\right)}. \tag{3.19}$$

This result provides a function relating radius and Poisson's ratio with the force constants and the beam/bond lengths appearing as coefficients. This can be solved for coupled

values of the radius and Poisson's ratio by minimising the difference between the value k_{ijk} as provided by a suitable molecular mechanics force field and the right hand side of equation 3.19. A suitable pair of values can be chosen by applying the additional constraint of material isotropy,

$$G = \frac{E}{2(1+\nu)}. \tag{3.20}$$

The isotropy condition is imposed for simplicity of the model rather than for any physical considerations. We can rewrite this by substituting equations 3.13 and 3.14 into equation 3.20

$$r(\nu) = \sqrt{\frac{4k_{ijkl}(1+\nu)}{k_{ij}}}. \tag{3.21}$$

The molecular mechanics constants thus provide all the required information to model the molecular bonds using beams. These can then be constructed to form a frame structure using standard finite element techniques.

3.2.2 Calculating piezoelectric properties

In order to use AFEM and molecular mechanics to calculate the piezoelectric properties of boron nitride nanotubes the dipole density of the tubes and its rate of change due to deformation must be calculated. The dipole density can be found by summing the atomic dipole moments and dividing by the surface area of the tube. The areal dipole density is used, rather than the volumetric density which would normally be used in calculations for bulk material properties, due to the difficulty in assigning a wall thickness to the hollow nanotube [25]. The use of areal rather than volumetric densities also changes the nature of the piezoelectric tensor and the units of its entries from $\mathrm{C/m^2}$ to C/m. Nanotubes are considered to be a one dimensional structure due to their high length to radius ratio. This low dimensionality allows the neglect of all but uniaxial tension and torsional deformation in determining their piezoelectric properties.

Atomic dipole moments can be calculated using atomic polarisabilities and the electric field at the atom sites using

$$\boldsymbol{p}_A = \alpha \boldsymbol{E}(\boldsymbol{r}_A), \tag{3.22}$$

where $\boldsymbol{p}_A$ is the atomic dipole moment, α is the atomic polarisability and $\boldsymbol{E}(\boldsymbol{r}_A)$ is the electric field at the atom position, $\boldsymbol{r}_A$. Atomic polarisabilities are available from the literature and are either calculated using quantum mechanics or are determined experimentally [29]. The polarisabilities of boron and nitrogen used in this work were $3.03 \times 10^{-24}\mathrm{cm}^3$ and $1.10 \times 10^{-24}\mathrm{cm}^3$ respectively [30].

To calculate the electric field the position of the atom centres and the values of the effective charges on the atoms must be known. The atom positions are calculated using molecular mechanics or with AFEM; they are the same as the location of the nodes in the finite element simulation. There are many methods available for calculating effective

atomic charges but the most convenient are simple approaches based on electronegativities and atomic hardness or idempotential [18, 19, 20, 31, 32]. The basis of such methods is electronegativity equalisation, which involves the expansion of chemical potential E of an atom A in a molecule so

$$E_A(Q) = E_A + Q_A \left.\frac{\partial E}{\partial Q}\right|_A + \frac{1}{2}Q_A^2 \left.\frac{\partial^2 E}{\partial Q^2}\right|_A \dots \tag{3.23}$$

where Q is the charge on the atom [18]. If the energy at $Q = 0$ is taken as the zero point of the energy scale, the atomic energy at $Q = +1$ is equivalent to the ionisation energy. In the same manner, the energy at $Q = -1$ is equivalent to the electron affinity and it is possible to show that

$$\left.\frac{\partial E}{\partial Q}\right|_A = \frac{1}{2}(E_\mathrm{i} + E_\mathrm{ea}), \tag{3.24}$$

where E_i is the first ionisation potential and E_ea is the electron affinity of the atom. Equation 3.24 is the definition of the Mulliken electronegativity [33], χ_A^0. A further expression which can be derived from equation 3.23 is

$$\left.\frac{\partial^2 E}{\partial Q^2}\right|_A = E_\mathrm{i} - E_\mathrm{ea}, \tag{3.25}$$

which is the idempotential J_{AA}^0, the Coulomb repulsion between two electrons in the ϕ_A orbital[19]. This allows the expression of the total energy of the molecule as the sum of the atomic energies plus the Coulomb potential generated due to atoms with non zero charge thus,

$$E(Q_1 \dots Q_N) = \sum_{A=1}^{N} \left(E_{A0} + \chi_A^0 Q_A + \frac{1}{2} J_{\mathrm{AA}}^0 Q_A^2 \right) + \sum_{A=1}^{N} \sum_{B=1, B\neq A}^{N} Q_A Q_B J_{AB}. \tag{3.26}$$

Here, $Q_A Q_B J_{AB}$ is the Coulomb interaction energy of atom A and atom B. When atoms A and B are far apart the Coulomb interaction energy is equivalent to the classical Coulomb potential $J = Q_A Q_B / 4\pi\epsilon_0 r_{AB}$. However, at short interatomic distances the Coulomb interaction must be represented using a functional form that tends to the to the idempotential and not infinity as r_{AB} tends to zero. Taking the derivative of equation 3.26 with respect to Q_A leads to

$$\frac{\partial E}{\partial Q_A} = \chi_A^0 + \sum_{B=1}^{N} \sum_{B=1}^{N} J_{AB} Q_B. \tag{3.27}$$

where $\partial E / \partial Q_A = \chi_A$ which is the atomic chemical potential. There must be a certain set of partial atomic charges Q_B that lead to equal values for the atomic chemical potentials. These partial charges describe the electronegativity equalised state, where the potential due to differences in the electronegativity of the atoms is equal to the potential created

by the electric field due to the partial charges. The equilibration of the atomic chemical potentials leads to the $N-1$ constraints

$$\chi_1 = \chi_2 = \cdots \chi_N, \tag{3.28}$$

which when combined with the constraint of constant total charge

$$Q_{\text{Total}} = \sum_{A=1}^{N} Q_A \tag{3.29}$$

can be used to solve the N simultaneous equations described by equation 3.27. This can be achieved by solving the linear system $\boldsymbol{AQ} = \boldsymbol{b}$ where

$$\boldsymbol{A} = \begin{bmatrix} 1 & 1 & \dots & 1 \\ J_{1,1} - J_{2,1} & J_{1,2} - J_{2,2} & \dots & J_{1,N} - J_{2,N} \\ J_{2,1} - J_{3,1} & J_{2,2} - J_{3,2} & \dots & J_{2,N} - J_{3,N} \\ \vdots & \vdots & \ddots & \vdots \\ J_{N-1,1} - J_{N,1} & J_{N-1,2} - J_{N,2} & \dots & J_{N-1,N} - J_{N,N} \end{bmatrix} \tag{3.30}$$

and

$$\boldsymbol{b} = \left[Q_{\text{Total}}, \chi_2^0 - \chi_1^0, \chi_3^0 - \chi_2^0, \dots, \chi_N^0 - \chi_{N-1}^0\right]^T \tag{3.31}$$

and $\boldsymbol{Q}$ is a vector of the partial atomic charges. Once the atomic positions and charges are known the electric field at the individual atom sites is calculated using Coulomb's law.

The piezoelectric property of interest in this work is the piezoelectric coupling tensor for the boron nitride nanotubes,

$$\mathsf{e} = \frac{\partial \boldsymbol{P}}{\partial \boldsymbol{S}}. \tag{3.32}$$

Here $\boldsymbol{P}$ is the areal dipole density vector and $\boldsymbol{S}$ is the strain vector in a constant electric field. Due to the one dimensional nature of nanotubes the only entry for $\boldsymbol{P}$ that must be considered is parallel to the tube axis. Likewise, the only entries for the strain vector are axial elongation and axial torsion. The non zero entries of the piezoelectric coupling tensor all take the same value for boron nitride nanotubes so it is only necessary to calculate a single derivative. In this work the effect of torsion on the dipole moment parallel to the tube axis was studied. The dipole density per unit area for the tubes is given by

$$\boldsymbol{P} = \frac{\sum_{A=1}^{N} \boldsymbol{p}_A}{2\pi R_{\text{tube}} L}, \tag{3.33}$$

where $\boldsymbol{P}$ is the dipole moment density, R_{tube} is the radius of the nanotube and L is the length of the nanotube. The shear strain γ due to the torsion in the nanotube was

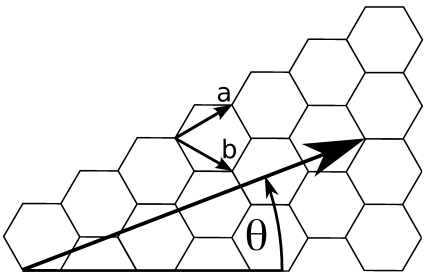

Figure 3.2: A two dimensional hexagonal lattice can be spanned by two basis vectors **a** and **b**. The diagram shows a $(5, 1)$ vector $(5\mathbf{a} + \mathbf{1b})$ with chiral angle θ defined between the (n, n) vector and the $(5, 1)$ vector. Valid vectors must have the correct type, boron or nitrogen, at both end of the chiral vector to ensure periodicity of the boron nitride lattice.

calculated using

$$\gamma = \tan^{-1}\left(\frac{R_{\text{tube}}\theta}{L}\right), \tag{3.34}$$

where θ is the torsion angle. The piezoelectric tensor entry was generated by simulating a number of tubes undergoing varying amounts of axial torsion and using finite differences to approximate the derivative.

3.2.3 Boron Nitride Nanotube Simulations

To test the AFEM method a range of boron nitride nanotubes were modelled using a bespoke Matlab script. The tubes varied in radius from 1.6 Å to 11.0 Å covering all available chiralities in this range. The chirality of the nanotubes is determined by the vector that connects two equivalent lattice points of a hexagonal sheet. This vector describes the direction of rolling if the tube were to be produced by rolling a sheet to form the tube. The chirality can be described by either two integer values, that act as multipliers of the two basis vectors needed to span the two dimensional hexagonal lattice, or by an angle formed between the vector and a predefined direction. In this work a 0° chiral angle is the same as an (n, n) chiral vector, a vector which points along an armchair edge of the hexagonal lattice. See figure 3.2 for illustration of this point.
The length of tubes was varied as a function of tube radius in order to ensure a length to radius ratio of twenty. The tubes were terminated with hydrogen atoms in order to provide a physically realistic structure, necessary for the charge equilibration methods. A range of electronegativity equalisation methods are available, such as the charge equilibration method (QEq) [19] and the PACHA formalism [20], which utilise the concepts presented in section 3.2.2. Atomic charges in this work were generated using the PACHA formalism as implemented in the General Lattice Utility Program (GULP) [34]. Initially the QEq method was used but its recursive procedure failed to converge for many of the tubes so PACHA was adopted instead. The partial charges were generated for each tube and the variation of chiralities and radii resulted in subtly different partial charges, as can

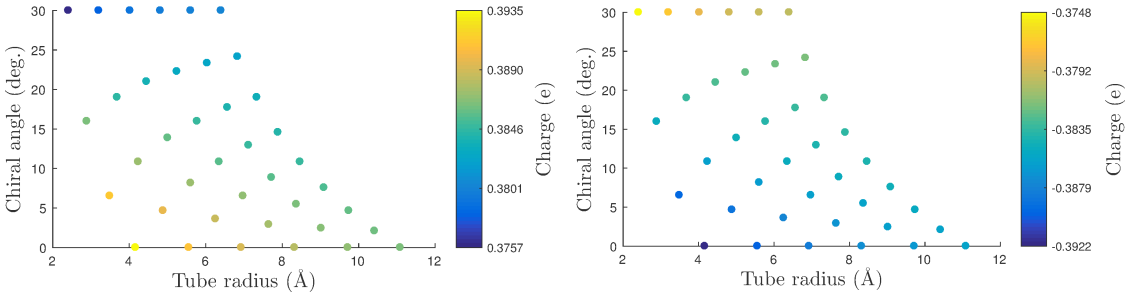

(a) Boron charges **(b)** Nitrogen charges

Figure 3.3: The partial charges of boron and nitrogen atoms for different radii and chirality.

Table 3.1: The linearised force constants and effective beam properties used for both the Euler-Bernoulli and Timoshenko beam models which were used for the (16,16) nanotube. The beam radius for the Euler-Bernoulli beam model is included for comparison with the Timoshenko beam model radius only. The beam radii and Poisson's ratio were found using the methods described in section 3.2.1.

Energy component	Euler-Bernoulli	Timoshenko
k_{Axial}	6.265×10^{-8}N Å^{-1}	6.265×10^{-8} N Å^{-1}
k_{Bend}	4.873×10^{-9}N Årad^{-1}	4.873×10^{-9}N Årad^{-1}
k_{Torsion}	1.325×10^{-9}N Årad^{-2}	1.325×10^{-9}N Årad^{-2}
r_{Beam}	0.558Å	0.301Å
ν (Poisson's ratio)	-	0.068

be seen in figure 3.3. The Universal Force Field (UFF) [35] potential model was chosen to provide the force constants used in the AFEM model and the molecular mechanics optimisations, thus allowing for direct comparison of results. UFF was chosen as it is relatively simple, has the option of linear or non-linear force expressions and provides the required parameters for boron, nitrogen and hydrogen atoms.

The first step in the simulations was optimisation of the nanotube geometry using molecular mechanics energy minimisation in GULP. AFEM requires that the original atomic positions are those of the minimum energy for the molecule [36]. The original input geometry, generated by our script, assumed that all the atoms lie on the surface of a cylinder which is not an accurate model of a boron nitride nanotube [37]. Structure optimisation results in the atoms forming a wrinkled tube surface as can be seen in figure 3.4.

The depth of the wrinkling of the surface varies with the tube radii, as the radius increases the wrinkling lessens. This relationship suggests that as the radius tends to infinity the wrinkles will disappear leaving a planar hexagonal boron nitride sheet. The relationship between wrinkle depth and nanotube radius is shown in figure 3.5 with data from density functional theory calculations of Wirtz et al [38].

The force constants for the AFEM model were generated by making linear approximations of the force equations generated from the UFF potential about the equilibrium

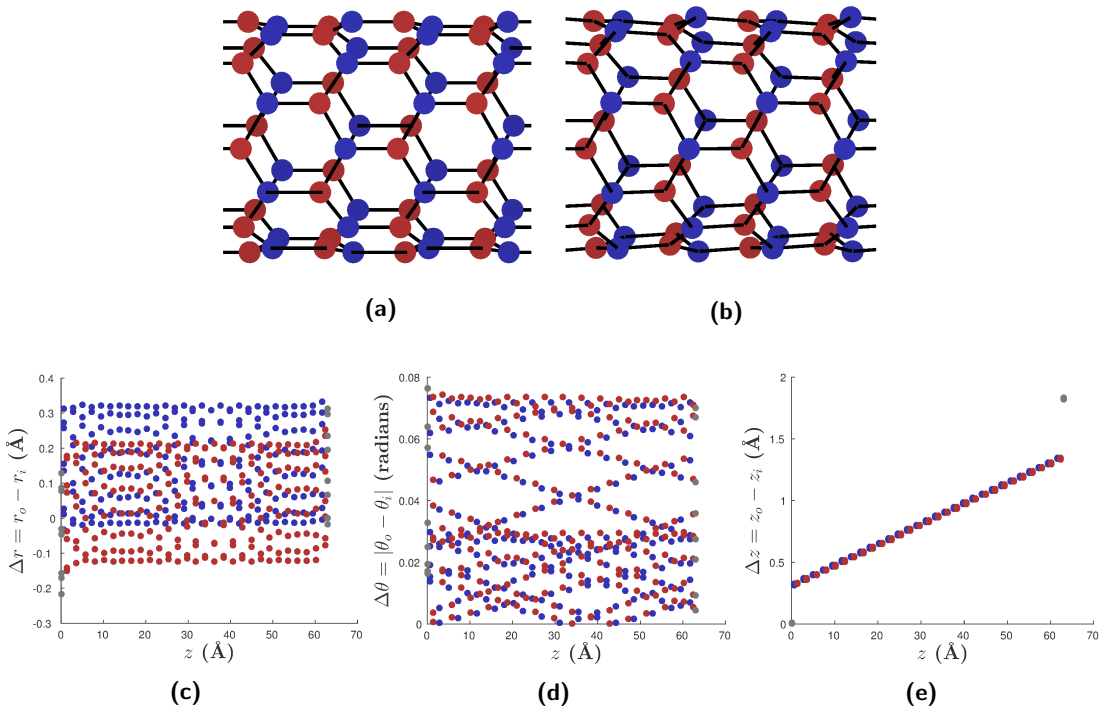

Figure 3.4: Figure 3.4(a) shows the shape of an (8,0) nanotube in its initial state, where all atoms lie on the circumference of a circle and figure 3.4(b) shows the relaxed state with its 'wrinkled' surface. The boron atoms are marked as red and the nitrogen atoms as blue with the grey dots representing the hydrogen atoms used to terminate the tubes (only visible in c through d). The graphs show the change in position of the atoms in cylindrical polar coordinates plotted against position along the length of the tube. Figure 3.4(c) shows the change in radial distance from the central axis of the tube, figure 3.4(d) shows the slight adjustments to the angular positions and figure 3.4(e) shows how the relaxed tube has changed length as the surface has wrinkled.

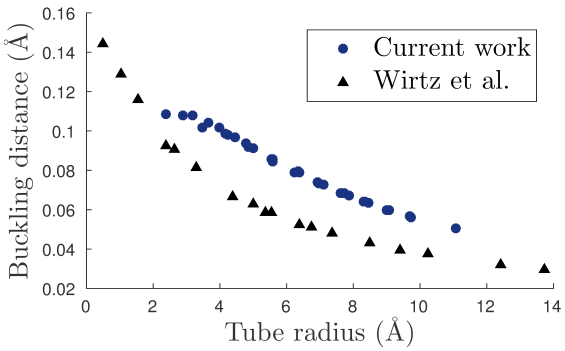

Figure 3.5: Plot showing the depth of the wrinkles of different boron nitride nanotubes against tube radius. The DFT data from Wirtz et al. [38] shows a similar pattern but with a faster decay as the radius increases. The UFF based data of this work shows a flattening of the cusp seen in the DFT data as the radius tends to 0.

bond lengths, angles and torsion angles of the optimised geometry for each nanotube. Table 3.1 shows some examples of the force constants and beam properties that were used in the AFEM simulations. This harmonic potential approximation requires that all deformations are kept small.

With the molecular geometry optimised, two different loading scenarios were simulated: torsion and extension. For the torsional simulations the hydrogen atoms and the first connected boron and nitrogen atoms at one end of the tube were rotated about the tube axis by progressively larger angles.

The angles of rotation were chosen by setting a limit of 0.2% on the shear strain of a continuous hollow tube with the same length and radius of the nanotube under consideration. The translational degrees of freedom perpendicular to the tube axis of the atoms at both ends of the tubes were then removed in order to provide the boundary conditions for both the molecular mechanics and atomistic finite element simulations. This allowed the tubes to change in length while the relative rotation of the two ends is kept constant. For the extension simulations a similar approach was taken but with one end of the tubes subjected to an increasing displacement along the tube axis. The extension of the tubes was limited to 0.1% strain and only the axial coordinate was held constant for the boundary atoms at both ends of the tubes.

Finally, the tubes were optimised in GULP (using UFF) with the applied restrictions on the end atoms and using second derivative methods employing the Broyden – Fletcher – Goldfarb – Shanno (BFGS) algorithm [39]. For the largest tubes limited memory BFGS (lBFGS) was used for the first optimisation steps and the final steps employed the full BFGS algorithm. Simultaneously, the tube geometries were input into the AFEM code and a sparse stiffness matrix generated by assembling translated element stiffness matrices. The boundary conditions were applied and the stiffness matrix subdivided and the system of equations solved using Matlab's inbuilt left divide method. After the final atom positions were calculated in each method the dipole density was calculated and a finite difference scheme used to determine the rate of change of dipole density due to

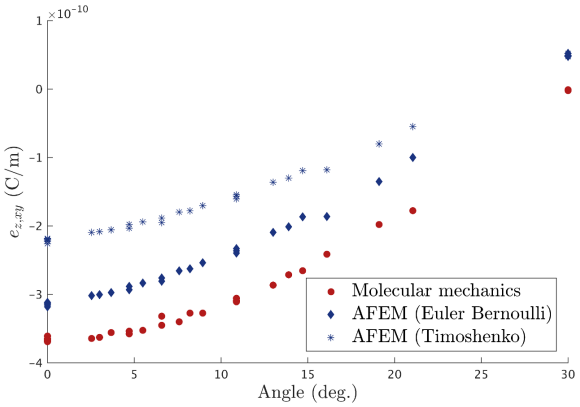

Figure 3.6: Piezoelectric coefficients, $e_{z,xy}$, for a number of different nanotubes with varying chirality placed under torsional loading. Results from Sai and Mele [25] are included for comparison. Qualitatively, both the AFEM plots show similar responses compared to the molecular mechanics as the chiral angle is varied, but quantitatively they show a smaller piezoelectric response and erroneous non zero tensor coefficients for the 30° chiral angle tubes (i.e. zigzag tubes).

increasing stress in the tubes.

3.3 Results

The results of the torsional simulations are shown in figure 3.6 which plots the piezoelectric response of a number of nanotubes of different chirality subjected to a torsional loading. The chiral angle varies between 0°, an armchair nanotube with chiral vector (n, n), and 30°, a zig-zag nanotube with chiral vector $(n, 0)$. The chiral vector is the same that which is commonly used for carbon nanotubes but it is important to note that only even values of n are used to ensure boron atoms are only bonded to nitrogen atoms and vice versa. Although the overall trend in the results is similar to that in other work, the values for the piezoelectric tensor coefficient produced using AFEM are notably lower. The most significant failure of AFEM is the inability to produce a zero value for the piezoelectric tensor coefficient for zig-zag type BNNTs under axial torsional loading. The results generated using molecular mechanics, even using a relatively old potential model such as UFF, were surprisingly close to those generated using more accurate quantum mechanical electronic structure methods [25].

The results for the extension based simulations are shown in figure 3.7. The molecular mechanics based results can be seen clearly in figure 3.7(b) and show the correct trend with respect to chiral angle but the method appears to overestimate the value of the piezoelectric tensor coefficient. The data points should be a mirror image of those seen in figure 3.6 tending to -3.68 C/m at 30° but the simulations produced a value of -4.28 C/m. The AFEM results fail to reproduce either the trend or the values expected based on either the molecular mechanics results or results produced by other authors using

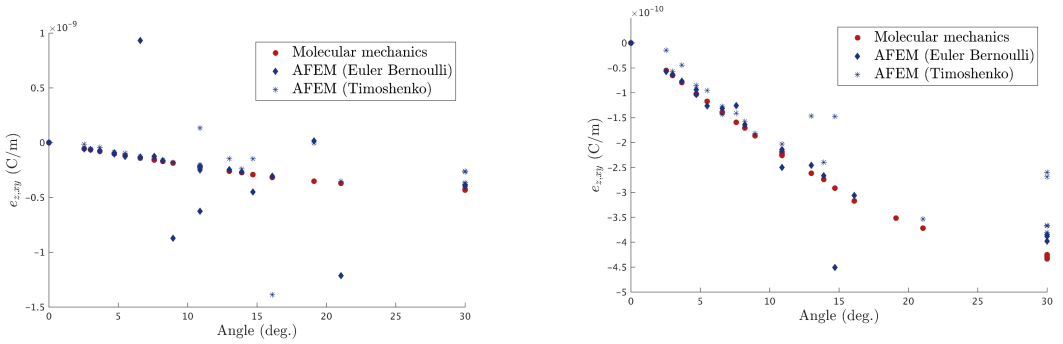

(a) Plot showing all results.

(b) Close up of the molecular mechanics minimisation results.

Figure 3.7: Calculated piezoelectric coefficients of nanotubes subjected to an axial load. The left plot shows all the results and the significant variability of the AFM values. The right plot shows a close up of the molecular mechanics minimisation results showing the correct trend and reasonable values.

higher fidelity models. Figure 3.7(a) captures the scatter of all the AFEM results and shows the extent of the disparity with the molecular mechanics results.

To examine the differences between the AFEM and molecular mechanics results a comparison of the final positions of the atoms, generated using AFEM and MM, was performed for a each nanotube. The atomic positions were transformed from Cartesian to cylindrical polar coordinates and then the atomic displacements were calculated, for both AFEM and MM the change in position from the optimised geometry to the twisted are extended geometries. A selection of the results from this analysis can be seen in figures 3.8 and 3.9. For the torsional case seen in figure 3.9, the AFEM results show a linear increase in angular displacement, which is expected of a continuum mechanics based model. They also show a slight bulge at one end of the tube and a spread of displacements along the length of the tube which vary depending on the chirality of the tube. The molecular mechanics method shows the tubes bulging in different positions along the tube from the AFEM, normally in the middle of the tube, and that the bulge is coupled to angular displacement behaviour. The two methods give very different results for the tension load case. The radial and angular displacements for the AFEM simulations are entirely different to those generated using the molecular mechanics method.

To understand further the discrepancy between the two methods the energies relating to different molecular deformation modes were compared. This analysis was carried out on a (16,16) armchair BNNT and the results are in tables 3.2 and 3.3. These results clearly show that the Timoshenko formulation, although arguably correct for the aspect ratio of the beams used to model the molecular bonds, results in significantly lower total energies when compared with the Euler-Bernoulli formulation or molecular mechanics. This result is expected as the more compliant nature of the Timoshenko beam formulation will result in lower input energies required to produce the same amount of deformation. The Euler-Bernoulli formulation performs reasonably well in the torsion load case but poorly in the tensile load case when compared with the molecular mechanics minimisation results.

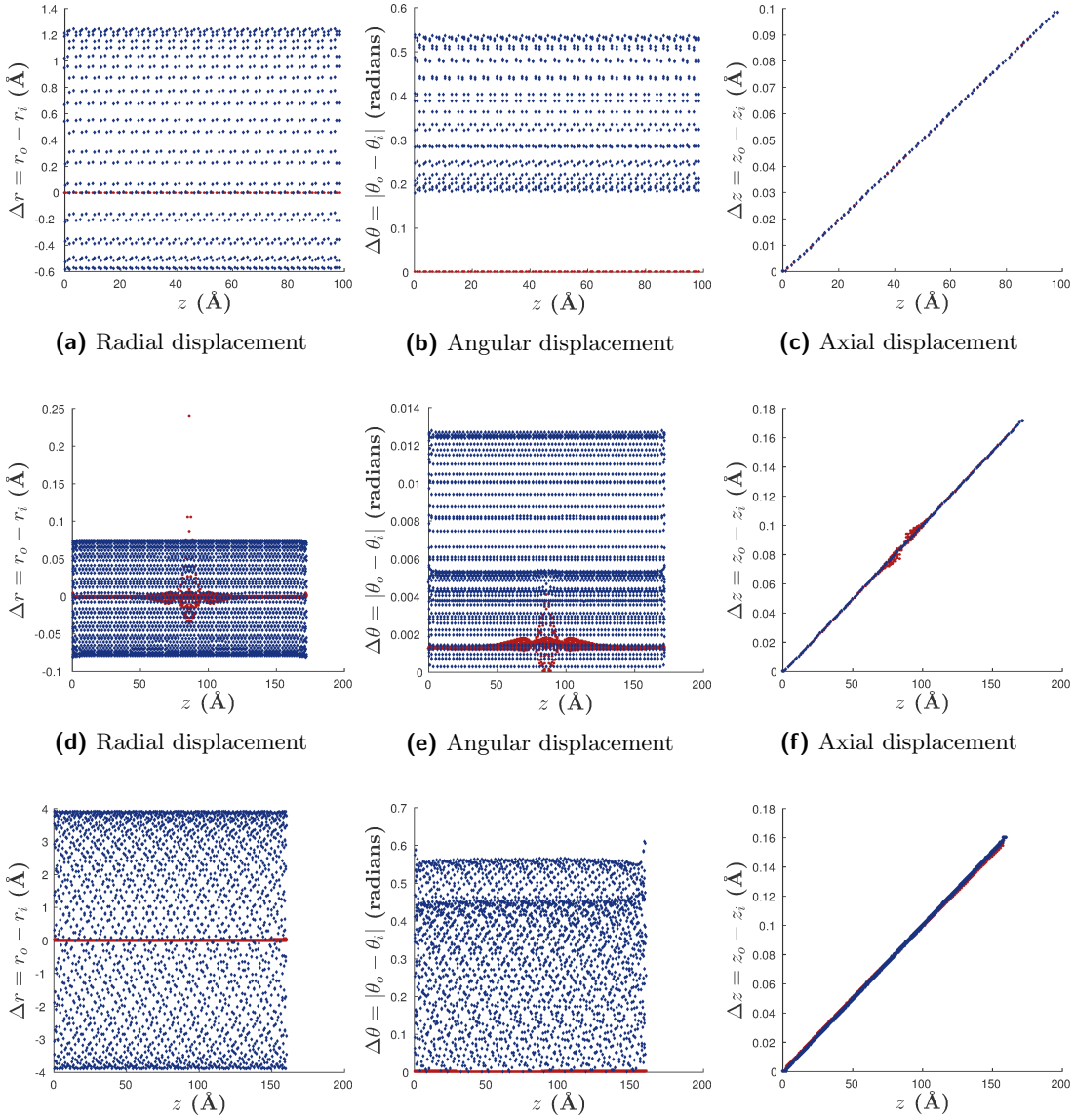

(a) Radial displacement **(b)** Angular displacement **(c)** Axial displacement

(d) Radial displacement **(e)** Angular displacement **(f)** Axial displacement

(g) Radial displacement **(h)** Angular displacement **(i)** Axial displacement

Figure 3.8: A selection of plots comparing the displacement of the molecular mechanics results (shown in red) with the displacements of the atomistic finite element method using Euler-Bernoulli beam elements (shown in blue) for nanotubes under axial tension. The displacements are measured from the optimised atomic coordinates of the relaxed nanotube and are given in cylindrical polar coordinates with the z axis at the center of the tube. Figures a-c are for a (12,0) nanotube, d-f are for a (12,12) nanotube and g-i are for a (14,8) nanotube.

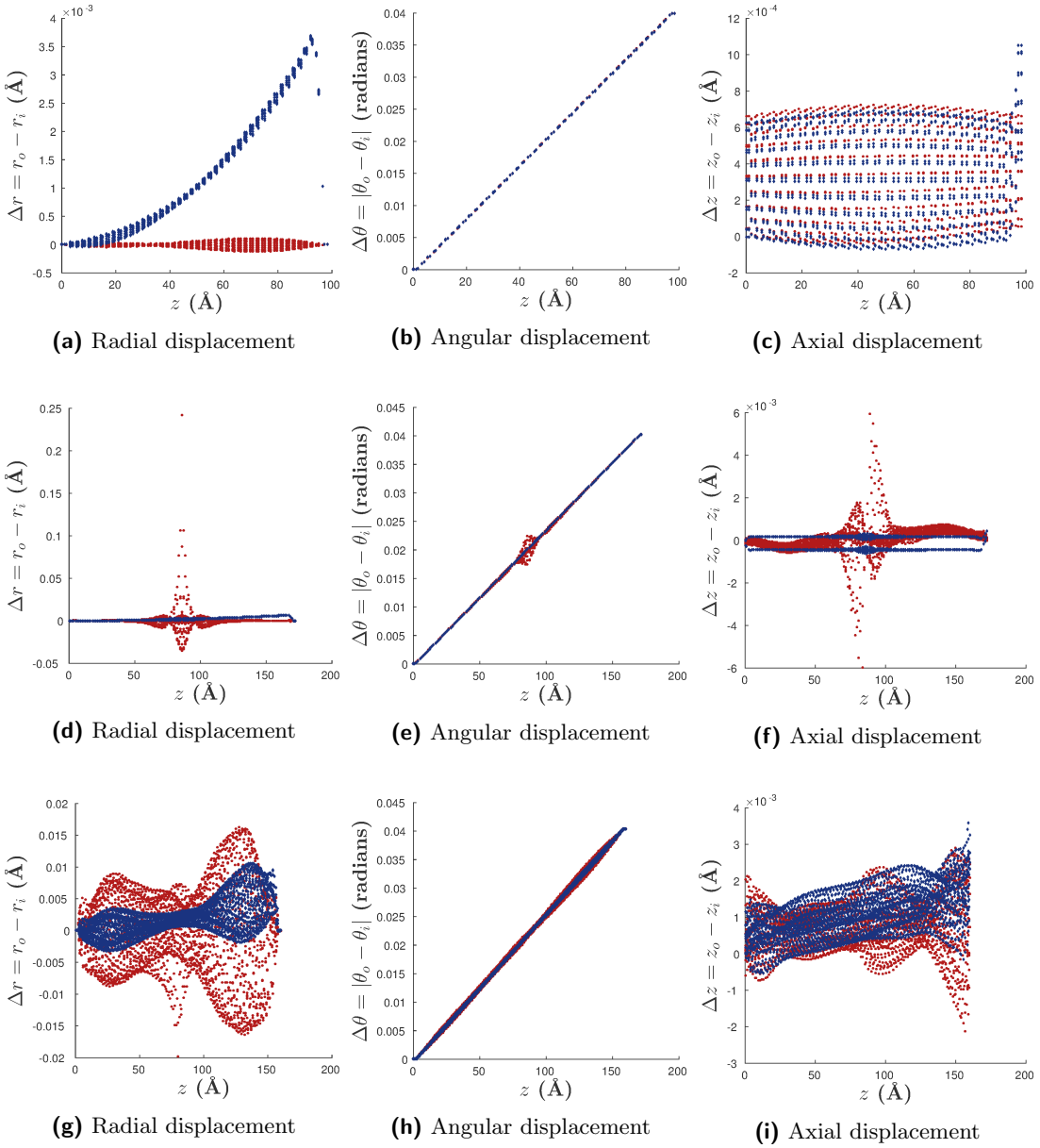

(a) Radial displacement **(b)** Angular displacement **(c)** Axial displacement

(d) Radial displacement **(e)** Angular displacement **(f)** Axial displacement

(g) Radial displacement **(h)** Angular displacement **(i)** Axial displacement

Figure 3.9: A selection of plots on the same basis as figure 3.8 but for torsionally loaded nanotubes.

Table 3.2: Components of energy, given in electron volts, for a (16,16) BNNT under axial tension at 1% strain. The molecular mechanics minimisation results are the difference between the energy of the optimised geometry and the energy at 0.1% strain. The AFEM values are the sum of the strain energies for all elements for the different modes of deformation, tension/compression, bending and torsion, at 0.1% strain. The AFEM method assumes that beam tension/compression, bending and torsion corresponds to the bond extension, angle and torsion terms of the molecular mechanics potential.

Energy component	MM minimisation (eV)	AFEM (Euler-Bernoulli) (eV)	AFEM (Timoshenko) (eV)
Bond extension	0.1167	0.0767	0.0130
Bond angle	0.6389	0.0612	0.0437
Bond torsion	-0.4753	0.0000	0.0000
Inversion	-0.1393	-	-
Van de Waals	-3.5153	-	-
Electrostatic	3.5399	-	-
Total	0.1656	0.1379	0.0567

This difference appears to depend on the non-bonded energy terms ignored in the AFEM formulation.

The energy calculations can be used to calculate values for the Young's modulus and the shear modulus of the nanotubes using

$$U_{\text{Tension}} = \frac{1}{2}\frac{EA}{L}\left(\Delta L\right)^2, \tag{3.35}$$

and

$$U_{\text{Torsion}} = \frac{1}{2}\frac{GJ}{L}\left(\Delta\theta\right)^2, \tag{3.36}$$

rearranged for E and G respectively. The area, A, and the torsion constant, J, can be calculated for a hollow tube with a wall thickness equal to the interplanar distance of hexagonal boron nitrite. The results of this analysis and some values from the literature are shown in table 3.4. These are in good agreement with those from similar methodologies. The values from Verma et al. [40] for a similar nanotube predicted show good agreement with the values produced in this work despite the significant differences in the formulations of the Tersoff-Brenner potential [41] and the UFF potential. Li & Chou [9], the orginal authors of AFEM as implemented in the work, used Euler-Bernoulli type beams but generated force constants using the DREIDING potential [42]. Their results show similar values for the Young's modulus and shear modulus the values in this work for the Euler-Bernoulli type element formulation combined with the UFF potential.

The AFEM method implements the bond stretch term in exactly the same manner as the molecular mechanics potential. However the bonded terms from the potential, angle bending, torsion, and out of plane bending, are present in the AFEM model only after

Table 3.3: Components of energy, given in electron volts, for a (10,0) BNNT under torsion resulting in a 0.2% shear strain following the same method as Table 3.2.

Energy component	MM minimisation (eV)	AFEM (Euler-Bernoulli) (eV)	AFEM (Timoshenko) (eV)
Bond extension	0.1431	0.0645	0.0065
Bond angle	0.1904	0.1528	0.0606
Bond torsion	-0.0364	0.0010	0.0005
Inversion	-0.0078	-	-
Van de Waals	-0.0028	-	-
Electrostatic	0.0282	-	-
Total	0.3147	0.2184	0.0675

Table 3.4: Young's modulus, E, and shear modulus, G from different methods and authors with the wall thickness, t, used stated in each case. All values are calculated using an arbitrary wall thickness of 3.33Å, the interplanar distance for hexagonal boron nitride, except for the result from Li and Chou who performed the calculation using 3.4Å. The values for this work are for a (16,16) boron nitride nanotube. The values from Verma et al. are for a (15,15) nanotube and the values from Li & Chou are for a nanotube with a radius similar to that of the (16,16) tube, $r_{\text{Tube}} = 11.1$Å.

Work	Method	Potential	E (GPa)	G (GPa)	t (Å)
This work	MM	UFF	1039	492	3.33
This work	AFEM	UFF (Euler-Bernoulli)	865	342	3.33
This work	AFEM	UFF (Timoshenko)	356	106	3.33
Verma et al. [40]	MM	Tersoff-Brenner	1035	507	3.33
Li & Chou [9]	AFEM	DREIDING (Euler-Bernoulli)	900	500	3.40

considerable simplifications. These simplifications reduce the number of atoms involved in the bonded interaction terms by removing the three-body bond angle and four-body bond torsion interactions. The beam models attempt to replace these terms with two body bending and torsion terms which require the addition of rotational degrees of freedom. These degrees of freedom are not present in molecular mechanics methods and the stiffness matrix coefficients for these terms rely on various assumptions which are questionable in a molecular context. This leads to situations where pure bond torsions that occur in molecular mechanics are modelled as beam bending in AFEM, as shown by Nasdala et al. [43]. Complete neglect of the non-bonded interaction terms will always produce significant differences when comparing molecular mechanics minimisations, using potentials with bonded and non-bonded terms, with AFEM regardless of how well the bonded terms are reproduced.

Overall, it is clear that the AFEM generates quantitatively different atomic displace-

ments compared with molecular mechanics methods. This results in the quantitatively and qualitatively incorrect behaviour of the piezoelectric tensor values, energies due to deformation and mechanical properties of boron nitride nanotubes.

3.4 Discussion

While investigating AFEM as a potential candidate for simulating nanostructures under applied external loads it became evident it has significant similarities with the molecular mechanics models on which AFEM is built. Molecular mechanics force fields describe the energy of a molecular structure based on the atomic coordinates and the bonds that connect the atoms. Equation 3.1 is commonly used by many molecular mechanics potentials, although other forms are used as well. We can write equation 3.1 in general terms as

$$U = U(\boldsymbol{x}), \tag{3.37}$$

where U is the total energy and $\boldsymbol{x}$ are N atomic coordinates. Taking the gradient of the potential gives

$$F_i = -\frac{\partial U}{\partial x_i}, \tag{3.38}$$

where F_i is a force component on some atom and in some direction. The gradient of the energy can be used to find the energy minima close to some initial molecular conformation or can be used to provide forces for a time step integrator to perform molecular dynamic simulations. Methods such as conjugate gradient or steepest descents are two such methods for finding the energy minima and relaxing the structure. Furthermore, if the functional form of U is chosen such that the derivatives of U can be explicitly provided then such calculations can be performed with minimal computational cost. However, for many functions the most efficient method for finding a minimum is to employ the Newton-Raphson method, which requires the second derivatives

$$H_{ij} = \frac{\partial U}{\partial x_i \partial x_j}. \tag{3.39}$$

The second derivatives defined above form the entries for a Hessian matrix, the inverse of which is used in the Newton-Raphson method. This minimisation method still requires an initial geometry but can converge on a minimum in fewer iterations than first order methods. The draw back, compared to first derivative methods, is that it requires N^2 second derivatives to be computed and stored rather than just the N derivatives. For large numbers of atomic coordinates the computational time and storage requirements can be become onerous. However, most potentials are restricted by only having energy contributions based on nearby atoms. The bonded terms of equation 3.1 will only contribute energy for interactions between an atom and up to its third nearest neighbours. If a suitable cutoff to the nonbonded interaction terms of equation 3.1 are applied then

many of the mixed second derivatives will be zero.

FEM uses a similar approach to minimise the strain energy of a space frame structure but with two main differences: interactions between nodes are nearest neighbour pairwise interactions only and instead of node positions it uses node displacements. The first of these is reasonable when applied to continuum mechanics as any forces in a structure must be passed through its connected members. However, reducing the three- and four-body terms found in molecular mechanics potentials to nearest neighbour interactions will lead to a poor reproduction of the potential. Restricting the interactions to nearest neighbours does allow a very sparse and almost diagonal Hessian to be constructed which reduces the computational cost and memory requirements for solving the system. The second difference will cause no issues when transferring from linear pairwise interactions of MM to FEM but may cause problems if non-linear potential terms are used. If the second derivatives of the energy are constants in the MM potential then they will also be constants in the equivalent AFEM Hessian but provided displacements are kept small the constant AFEM Hessian should be a reasonable approximation. In this work the MM potential was linearised at the bond length, angles and dihedral angles of the MM relaxed structures to minimise error between the non-linear potential terms and the effective beam properties.

The question is why should anyone seek to simplify a MM potential to this degree and then seek to implement it in a FEM package? The parameters and functional forms for various potentials are available in many purpose built atomistic simulation packages but converting these to AFEM parameters is non-trivial. The quality of the output of AFEM clearly suffers due to the localisation of the many-body terms, the linearisation of the potentials and the loss of the non-bonded interactions. It would be possible to speed up calculations by implementing these alterations to the MM potential directly but it would be wise to maintain the many-body terms even if they are linearised. Throughout this work a significant part of the computational cost of the MM simulations was due to the large cutoff distances required for the electrostatic interaction term in the non-bonded energy. The fact that a large cutoff was needed to achieve convergence indicates that removing this term entirely will have a significant negative impact on the results.

It is possible to construct a stiffness matrix that follows the form of a molecular mechanics potential exactly such that the stiffness matrix of the FEM model and the Hessian matrix of the molecular mechanics potential will be identical [15, 44]. Equally, it is possible to parametrise a purely linear nearest neighbours potential for use in a any standard molecular mechanics package. There are few reasons to do either of these although some have suggested that by implementing atomistic simulations methods makes it easier to combine atomistic and continuum mechanics simulations [43]. The drawbacks of this approach are that implementing a MM potential in a FEM package takes time and the FEM software will not have the many useful tools present in atomistic simulation packages.

3.5 Conclusions

This chapter has shown the limitations of using a simple implementation of an atomistic finite element method for investigating the piezoelectric behaviour of boron nitride nanotubes. Further, it shows the failure of the method to accurately generate the displacement due to external loading for molecules with significant Coulombic interactions. We have applied methods for investigating the qualitative and quantitative behaviour of such models which allow direct comparison with higher fidelity models. The work raises the question of whether simple beam models, that use force-displacement constants that couple movement of only the bonded neighbour atoms, are suitable for molecular studies. The work also shows that neglecting non-bonded interaction terms from an empirical molecular mechanics potential will generate spurious results.
The use of molecular mechanics, coupled with dipole density calculations based on partial atomic charges calculated using electronegativity equalisation methods, shows some promise for calculating the piezoelectric properties of molecules.

Bibliography

[1] M. Tolladay, F. Scarpa, D. Ivanov, and N. Allan. Predicting piezoelectric effects in atomistic finite element simulations. In J. M. Floryan, editor, *Contributions to the Foundations of Multidisciplinary Research in Mechanics: Papers presented during the 24th International Congress of Theoretical and Applied Mechanics, ICTAM2016, Montreal 22-26, 2016.*, pages "2650–2651". International Union of Theoretical and Applied Mechanics, 2017.

[2] M. Tolladay, D. Ivanov, N. L. Allan, and F. Scarpa. Piezoelectric effects in boron nitride nanotubes predicted by the atomistic finite element method and molecular mechanics. *Nanotechnology*, 28(35):355705, 2017.

[3] C. Li and T. Chou. A structural mechanics approach for the analysis of carbon nanotubes. *International Journal of Solids and Structures*, 40(10):2487–2499, 2003.

[4] K. I. Tserpes and P. Papanikos. Finite element modeling of single-walled carbon nanotubes. *Composites Part B: Engineering*, 36(5):468–477, 2005.

[5] F. Scarpa, S. Adhikari, and A. Srikantha Phani. Effective elastic mechanical properties of single layer graphene sheets. *Nanotechnology*, 20(6):065709, 2009.

[6] J. Zhang, C. Wang, and S. Adhikari. Molecular structure-dependent deformations in boron nitride nanostructures subject to an electrical field. *Journal of Physics D: Applied Physics*, 46(23):235303, 2013.

[7] I. D. Muhammad, M. Awang, O. Mamat, and K. Z. K. Shaari. Estimating Young's Modulus of Single-Walled Zirconia Nanotubes Using Nonlinear Finite Element Modeling. *Journal of Nanomaterials*, 2015:1–8, 2015.

[8] S. Adhikari, E. I. Saavedra Flores, F. Scarpa, R. Chowdhury, and M. I. Friswell. A Hybrid Atomistic Approach for the Mechanics of Deoxyribonucleic Acid Molecules. *Journal of Nanotechnology in Engineering and Medicine*, 4(4):041006, 2014.

[9] C. Li and T. Chou. Static and dynamic properties of single-walled boron nitride nanotubes. *Journal of nanoscience and nanotechnology*, 6(1):54–60, 2006.

[10] C.-Y. Li and T.-W. Chou. Strain and pressure sensing using single-walled carbon nanotubes. *Nanotechnology*, 15(11):1493–1496, 2004.

[11] M. Meo and M. Rossi. Prediction of Young's modulus of single wall carbon nanotubes by molecular-mechanics based finite element modelling. *Composites Science and Technology*, 66(11-12):1597–1605, 2006.

[12] L. Boldrin, F. Scarpa, R. Chowdhury, and S. Adhikari. Effective mechanical properties of hexagonal boron nitride nanosheets. *Nanotechnology*, 22(50):505702, 2011.

[13] V. Nirmala and P. Kolandaivel. Structure and electronic properties of armchair boron nitride nanotubes. *Journal of Molecular Structure: THEOCHEM*, 817(1-3):137–145, 2007.

[14] S. Hou, Z. Shen, J. Zhang, X. Zhao, and Z. Xue. Ab initio calculations on the open end of single-walled BN nanotubes. *Chemical Physics Letters*, 393(1-3):179–183, 2004.

[15] L. Nasdala, A. Kempe, and R. Rolfes. The molecular dynamic finite element method (mdfem). *Computers Materials and Continua*, 19(1):57, 2010.

[16] G. I. Giannopoulos, D. N. Kontoni, and S. K. Georgantzinos. Efficient FEM simulation of static and free vibration behavior of single walled boron nitride nanotubes. *Superlattices and Microstructures*, 96:111–120, 2016.

[17] J. Gasteiger and M. Marsili. Iterative partial equalization of orbital electronegativity - a rapid access to atomic charges. *Tetrahedron*, 36(22):3219–3228, 1980.

[18] W. J. Mortier, K. Van Genechten, and J. Gasteiger. Electronegativity equalization: application and parametrization. *Journal of the American Chemical Society*, 107(4):829–835, 1985.

[19] A. K. Rappe and W. A. Goddard. Charge equilibration for molecular dynamics simulations. *The Journal of Physical Chemistry*, 95(8):3358–3363, 1991.

[20] M. Henry. Nonempirical quantification of molecular interactions in supramolecular assemblies. *ChemPhysChem*, 3(7):561–569, 2002.

[21] S. Iijima. Helical microtubules of graphitic carbon. *Nature*, 354(6348):56–58, 1991.

[22] A. Rubio, J. L. Corkill, and M. L. Cohen. Theory of graphitic boron nitride nanotubes. *Physical Review B*, 49(7):5081–5084, 1994.

[23] N. G. Chopra, R. J. Luyken, K. Cherrey, V. H. Crespi, M. L. Cohen, S. G. Louie, and A. Zettl. Boron Nitride Nanotubes. *Science*, 269(5226):966–967, 1995.

[24] E. J. Mele and P. Král. Electric Polarization of Heteropolar Nanotubes as a Geometric Phase. *Physical Review Letters*, 88(5):056803, 2002.

[25] N. Sai and E. J. Mele. Microscopic theory for nanotube piezoelectricity. *Physical Review B*, 68(24):241405, 2003.

[26] A. L. Tiano, C. Park, J. W. Lee, H. H. Luong, L. J. Gibbons, S.-H. Chu, S. Applin, P. Gnoffo, S. Lowther, H. J. Kim, P. M. Danehy, J. A. Inman, S. B. Jones, J. H. Kang, G. Sauti, S. A. Thibeault, V. Yamakov, K. E. Wise, J. Su, and C. C. Fay. Boron nitride nanotube: synthesis and applications. *Proc. SPIE*, 9060(Cvd):906006–906019, 2014.

[27] M. B. Panchal and S. H. Upadhyay. Boron Nitride Nanotube-Based Mass Sensing of Zeptogram Scale. *Spectroscopy Letters*, 48(1):17–21, 2015.

[28] G. Cowper. The shear coefficient in timoshenko's beam theory. *Journal of applied mechanics*, 33(2):335–340, 1966.

[29] J. Mitroy, M. S. Safronova, and C. W. Clark. Theory and applications of atomic and ionic polarizabilities. *J. Phys. B*, 43(202001):44, 2010.

[30] A. K. Das and A. J. Thakkar. Static response properties of second-period atoms: coupled cluster calculations. *Journal of Physics B: Atomic, Molecular and Optical Physics*, 31(10):2215–2223, 1998.

[31] C. E. Wilmer, K. C. Kim, and R. Q. Snurr. An Extended Charge Equilibration Method. *The Journal of Physical Chemistry Letters*, 3(17):2506–2511, 2012.

[32] G. C. Martin-Noble, D. Reilley, L. M. Rivas, M. D. Smith, and J. Schrier. EQeq+C: An Empirical Bond-Order-Corrected Extended Charge Equilibration Method. *Journal of Chemical Theory and Computation*, 11(7):3364–3374, 2015.

[33] R. S. Mulliken. A New Electroaffinity Scale; Together with Data on Valence States and on Valence Ionization Potentials and Electron Affinities. *The Journal of Chemical Physics*, 2(11):782, 1934.

[34] J. D. Gale and A. L. Rohl. The General Utility Lattice Program (GULP). *Molecular Simulation*, 29(5):291–341, 2003.

[35] A. K. Rappe, C. J. Casewit, K. S. Colwell, W. A. Goddard, and W. M. Skiff. UFF, a full periodic table force field for molecular mechanics and molecular dynamics simulations. *Journal of the American Chemical Society*, 114(25):10024–10035, 1992.

[36] X. Chen and G. Cao. A structural mechanics study of single-walled carbon nanotubes generalized from atomistic simulation. *Nanotechnology*, 17(4):1004–1015, 2006.

[37] M. Menon and D. Srivastava. Structure of boron nitride nanotubes: tube closing versus chirality. *Chemical Physics Letters*, 307(5-6):407–412, 1999.

[38] L. Wirtz, A. Rubio, R. de la Concha, and A. Loiseau. Ab initio calculations of the lattice dynamics of boron nitride nanotubes. *Physical Review B*, 68(4):045425, 2003.

[39] R. Fletcher. *Practical Methods of Optimization, 2nd ed.* John Wiley & Sons, Chichester, 1987.

[40] V. Verma, V. K. Jindal, and K. Dharamvir. Elastic moduli of a boron nitride nanotube. *Nanotechnology*, 18(43):435711, 2007.

[41] D. W. Brenner, O. A. Shenderova, J. A. Harrison, S. J. Stuart, B. Ni, and S. B. Sinnott. A second-generation reactive empirical bond order (REBO) potential energy expression for hydrocarbons. *Journal of Physics: Condensed Matter*, 14(4):783–802, 2002.

[42] S. L. Mayo, B. D. Olafson, and W. A. Goddard. DREIDING: a generic force field for molecular simulations. *The Journal of Physical Chemistry*, 94(26):8897–8909, 1990.

[43] L. Nasdala, A. Kempe, and R. Rolfes. Are finite elements appropriate for use in molecular dynamic simulations? *Composites Science and Technology*, 72(9):989–1000, 2012.

[44] A. A. R. Wilmes and S. T. Pinho. A coupled mechanical-charge/dipole molecular dynamics finite element method, with multi-scale applications to the design of graphene nano-devices. *International Journal for Numerical Methods in Engineering*, 100(4):243–276, 2014.

Chapter 4

Tensile mechanical strength of carbon-carbon bonds

This chapter examines the ability of different computational methods to calculate the forces between carbon atoms over a range of internuclear distances. The purpose of this work is to determine suitable methods for studying the mechanical strength of carbon based materials such as graphene nanoribbons or carbon nanotubes. Commonly used molecular mechanics potentials are tested alongside density-functional tight-binding methods (DFTB), a variety of density-functional methods (DFT) and a pair of post-Hartree-Fock (post-HF) methods, MP2 and CASSCF. The molecular mechanics potentials are shown to perform poorly compared to the electronic structure calculations and reasons for this are examined. DFTB is shown to be capable of reproducing the results of the computational more demanding DFT and post-HF calculations. Some of the work presented here was used as the basis for a conference paper [1].

4.1 Introduction

Nanostructures are an increasingly important topic in material science, with potential uses in electronics [2], hydrogen storage [3], water purification [4], catalysis [5] and composite materials [6]. Experimental investigation of nanostructures is difficult and costly to perform and often require verification of results through theoretical calculations. Simulating these structures requires modelling a few hundred to a few thousand atoms which is problematic for most electronic structure methods. The computational cost of these methods scales poorly with the number of electrons leading to limits on the size of the nanostructures which can be investigated.

Using nanostructures as structural components requires knowledge of what loads they can withstand and the degree of deformation to which they can be subjected. Determining the mechanical properties, such as the tensile strength, of nanoscale devices experimentally is an exceptionally complex task due to the difficulty of manipulating them accurately

and without causing damage while setting up the experiment. The alternative is to simulate nanostructures, which may contain thousands of atoms, responding to externally applied forces to the point at which the structure breaks into two or more pieces. Such calculations require accurate simulation of bonds being stretched to breaking point and beyond, which in turn requires an accurate description of the electronic behaviour. Computational chemistry has many tools capable of determining the electronic structure of molecules and materials over a wide range of bond lengths but there is always a trade off between accuracy and computational expense and bond dissociation is particularly challenging. It is important that reliable methods for simulating failure of nanostructures, containing thousands of atoms, can be identified. Common methods employed for simulating fracture and failure of nanostructures include reactive bond order potentials, which are parametrised molecular mechanics potentials that permit simulations of large numbers of atoms. The two most common methods are Tersoff-Brenner type potentials [7, 8] and the ReaxFF potential [9]. Prediction of the strength of graphene nanoribbons [10, 11, 12] and fracture growth in graphene [13, 14, 15] have been investigated using both of these potentials but the approximations made by these potentials make such predictions less reliable than *ab initio* results.

Accurate electronic structure methods are computationally expensive. Methods such as density functional theory (DFT), Møller-Plesset pertubation theory and many others can be employed but they all scale poorly with system size. Furthermore, it is necessary to employ multi-reference methods to capture the energetics of bond breaking [16, 17, 18, 19] due to the lack of size consistency and failure to account for static correlation effects in single reference methods. This can be seen graphically in figures 4.1(a) and 4.1(b) which shows the potential energy and corresponding force, respectively, for H_2 at a range of bond lengths. These figures show the results of a single reference method, PBE based DFT, using two different spin states compared with a multi-reference method labelled CASSCF(2,6).

Failure at the macroscale is defined by a materials tensile strength, the peak stress the material can carry before catastrophic failure. Since stress is determined by force per unit area the peak stress occurs at the peak force for a constant cross sectional area, at least when considering engineering rather than true stresses. From this perspective, bond strength can be considered as the maximum force that can be carried by the bond [20]. If a constant tensile force, greater than this limit, is applied to a pair of bonded atoms then it will overcome the restorative force of the bond and the bond will break. Bond strength is conventionally defined as the energy required to stretch a bond from its equilibrium separation to infinity so the term peak restorative force will be used to describe the mechanical strength investigated here. The peak occurs at the inflection point of the bond energy as a function of bond length [21], see figure 4.1(a). Determining values for this quantity experimentally is challenging but has been achieved using polysaccharide molecules covalenlty attached to a substrate and an atomic force microscope tip [20]. One

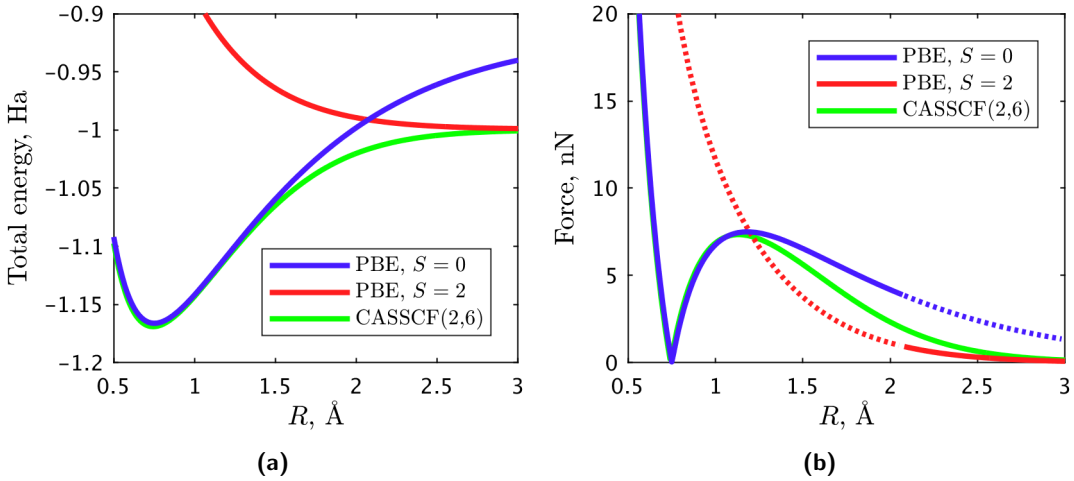

Figure 4.1: Figure (a) plots the total energy for a H_2 molecule as a function of internuclear separation and figure (b) plots the magnitude of the force on a hydrogen atom in H_2 as a function of internuclear separation where the dotted lines indicate that the plotted state is not the single determinant ground state. The two PBE functional based density functional theory results are for the cases where the electrons are spin paired ($S = 0$) and unpaired ($S = 2$). The spin paired PBE calculation tends towards an incorrect energy, higher than one Hartree, and converges less rapidly than the CASSCF result. The $S = 2$ plot crosses the $S = 0$ plot at which point it becomes the single determinant ground state which leads to an unphysical discontinuity in the force. The complete active space self consistent field (CASSCF) result shows the correct physical behaviour by tending towards an energy value of one Hartree, the energy of two hydrogen atoms at infinite separation. The multi reference CASSCF calculation contains contributions from a number of excited determinants so it avoids the discontinuity seen in the DFT results.

of the difficulties of these experiments was determining which bond had broken. This was achieved *a posteriori* by comparison with theoretical calculations for the various bonds that were present in the polysaccharide molecule and those that attached the molecule to the apparatus.

The field of mechanochemistry has undergone considerable development over the last two decades. This has included investigations of how polymer chains break or how otherwise inaccessible reaction pathways can be exploited. Experimental studies have used atomic force microscopy to study the mechanical strength of individual polymer chains [20, 22], ultrasound to open up reaction pathways in mechanophores contained in dissolved polymers [23, 24] and externally applied force to macroscale polymer samples [25]. Theoretical mechanochemistry has had to develop to keep pace with the experimental work. The constrained-geometry-to-generate-external-force (COGEF) method [21] uses relaxed potential energy scans to determine atomic forces. In this method the distance between a pair of atoms is scanned in a stepwise manner with the rest of the atoms allowed to relax at each step. The peak atomic forces found in these scans can then be used to construct Morse potentials for use in kinetics calculations of bond rupture. An alternative method, external-force-is-explicitly-included (EFEI) [26], applies forces to the atoms during the optimisation process. Although this allows for the structural response to the applied force to be determined it makes it difficult to map the post-peak-force

landscape. Both methods can be used to determine which bond breaks in a particular molecule but it is equally important to understand why a specific bond breaks. It has been shown that both mechanical bond strength and the alignment of the bond relative to the applied force determine whether it will or will not fail [27]. Analysis of the Hessian matrix of a molecule, using the redundant internal coordinate system, provides a method for calculating the distribution of energy within the conformal degrees of freedom for a molecular structure. This method, called the judgement of energy distribution (JEDI) [28], can be applied to a molecule to study how the applied force is passed through the molecule. A combination of these methods can be used to find the transition states for mechanochemically induced reactions but an alternative method for mapping such reaction pathways has been developed [29]. This method makes a cubic approximation of the potential energy at the critical point that lies between the equilibrium and transition states as a function of the reaction coordinate . In this way the behaviour of the molecule beyond the peak force can be determined.

In this work, calculations on small hydrocarbon molecules are carried out, extending the carbon-carbon bond lengths, in order to determine the peak restorative forces and the bond lengths at which they occur. Different techniques ranging from computationally expensive high accuracy calculations down to much cheaper molecular mechanics methods are examined and compared in order to establish suitable approaches for simulating hydrocarbon nanostructures undergoing large deformations. We examine whether multi-reference methods are required to calculate accurate peak restorative forces and corresponding bond lengths. Finally, we carry out calculations of large deformations on larger molecules to investigate the ability of different methods to capture the tensile forces required to pull apart molecules bonded with conjugated π-bonds.

4.2 Methods

4.2.1 Theoretical methods

A variety of single reference *ab initio* electronic structure techniques, a multi-reference method, density functional tight binding and two popular reactive molecular mechanics potentials were employed for the calculations. The single reference methods include density function theory (DFT) using a range of exchange correlation functionals. The PBE [30] functional was used; it is a very popular functional in current use. B3LYP [31, 32] was also selected as it is the most common hybrid functional in DFT calculations. Finally, the more recent B2PLYPD3 [33] was chosen as it contains both exact exchange, a perturbation theory based correlation correction and a dispersion term. The other single reference method tested was Møller-Plesset perturbation theory [34], MP2, which is capable of recovering significant amounts of dynamic correlation energy. Complete-active-space-self-consistent-field (CASSCF) calculations were performed due

to the multi-reference nature of bond breaking events. Multiple degenerate or nearly degenerate wavefunctions can describe an extended bond close to scission. This results in a large static correlation error for single reference methods. Multi-configuration approaches, such as CASSCF, are capable of recovering the static correlation energy by including excited states in their calculations. CASSCF was used to determine whether multi-reference methods produce peak restorative forces significantly different from single reference methods. These unrestricted spin calculations were performed using Gaussian 09 [35]. The PVTZ basis set (cc-PTVZ) [36] was selected as it offered the best balance between accuracy and computational speed. Higher zeta and augmented basis sets were tested on ethane and ethene and the maximum forces were the same to two significant figures as those from the cc-PTVZ calculations.

These methods all involve computationally expensive calculations that are unfeasible for modelling nanostructures of thousands of atoms so cheaper alternatives were also considered. Two commonly used methods for simulating nanostructure failure are the reactive molecular mechanics potentials REBO and ReaxFF. Brenner's reactive empirical bond order potential (REBO) [8] and its derivatives have been widely used for modelling hydrocarbon nanotructures [37, 11, 38]. Different parametrisations of this potential have also been used for boron nitride based structures [39, 40]. This potential and its derivatives have been implemented in many popular atomistic modelling packages. The second generation REBO potential [41] was used as implemented in the General Utility Lattice Program (GULP) [42] and the adaptive intermolecular REBO (AIREBO) [43] variant was used as implemented in LAMMPS [44]. The AIREBO potential was modified to reduce the range of the switching function which reduces carbon-carbon interactions to zero as suggested in earlier work [45]; the switching function is converted from a cosine form to a step function at 2.0 Å.

The other reactive potential considered here is ReaxFF [9]. This potential is available in both LAMMPS and GULP with a number of different parametrisations. Both packages were used but as their parameter files are not directly convertible it is difficult to make comparisons between the two implementations. As such both packages were used with the default parameter files that are distributed with the software.

Finally, density functional tight binding (DFTB) was used as implemented in DFTB+ [46]. This method comes in three main variants: non-self-consistent-charge (non-SCC-DFTB) [47, 48], self-consistent-charge (SCC-DFTB) [49] and third order (DFTB3) [50]. The non-SCC variant does not take account of charge transfer between the atoms whereas SCC-DFTB includes charge transfer by way of a second order approximation of DFT using Mulliken charges. DFTB3 includes third-order corrections by allowing atomic hardness to vary as a function of the Mulliken charge on each atom. DFTB relies on parameter sets based on DFT calculations using artificially constrained electron densities to provide two-centre Fock and overlap matrix elements over a range of internuclear distances. Once these matrix entries are determined a repulsive potential is fitted by calculating the dif-

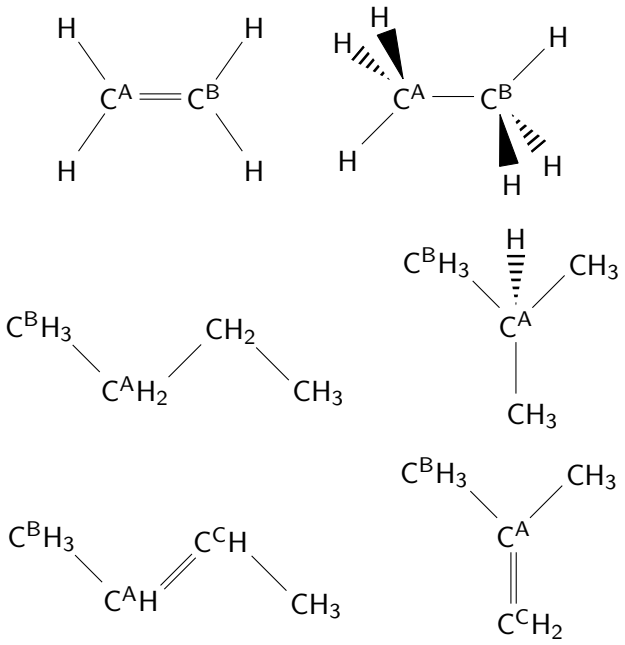

Figure 4.2: The structures of ethene, ethane, butane, isobutane, trans-β-butene and isobutene. The superscripts A,B and C indicate carbon atoms that were manipulated in the bond length scans.

ference between between the DFTB calculation and higher order calculations for various test molecules. Charge self-consistency is determined by including an internuclear partial charge term using atomic hardness parameters. Third order DFTB extends the SCC correction using the gradient of the atomic hardness. The method has also been extended to include unrestricted spin calculations which requires additional parameters. There are three main parameter sets available for DFTB each of which reflects a different stage of the development of the method. The oldest set is referred to here as pbc, the next is mio and the most recent set 3ob. The pbc and mio sets are both usable for SCC calculations but the 3ob set is described by its authors as only suitable for DFTB3 type calculations [51]. These all contain parameters for hydrogen, carbon, nitrogen and oxygen.

4.2.2 Procedures for small molecules

Potential energy curves were generated for a range of small hydrocarbon molecules. The internuclear distance for a bonded pair of carbon atoms was increased in steps of 0.01 Å allowing all other atoms to relax at each step. The total energy and atomic forces were calculated and plotted as a function of internuclear distance. The peak restorative force was determined as the maximum absolute force on one of the carbon atoms at a bond length greater than the relaxed bond length. The magnitude of the peak restorative force is equal to the maximum constant force that can be applied to the atom before molecular fragmentation and dissociation. Restorative forces may still be present at bond lengths greater than that at which the peak occurs but these would be overcome by an external

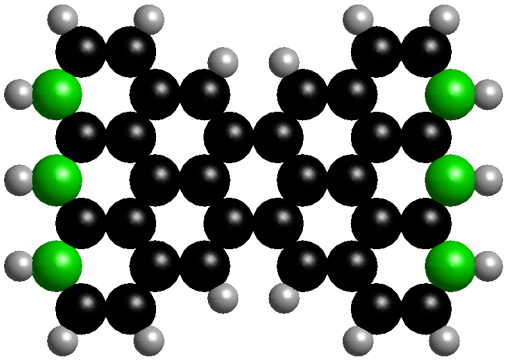

Figure 4.3: The structure of 'Clar's goblet' with carbon atoms in black and hydrogen in white. The green atoms are carbon atoms constrained such that the atoms either side form straight lines which would remain parallel during structural relaxations. The distance between the two sides was increased by 0.01 Å after each relaxation.

force which exceeds the peak value. The values of the peak restorative force and the corresponding internuclear distance from the different methods are then compared.
Ethene, ethane, butane, trans-β-butene (henceforth referred to as butene), isobutane and isobutene, are investigated in this work (figure 4.2). These structures were selected as they include both single and double carbon bonds and allow for examination of the effect of the local environment on the properties of interest. Single carbon-carbon bonds connecting atoms indicated by the superscripts A and B in figure 4.2 were extended to failure. Double bonds connecting atoms marked by the superscripts A and C were tested independently from the single bond tests.

4.2.3 Procedures for larger hydrocarbon structures

Graphene and nanostructures made of graphene are held together by conjugated π-bonds. To investigate this type of bond two larger polycyclic aromatic hydrocarbon molecules were tested by performing pseudostatic tensile tests. This is akin to simulating externally applied loads and is a commonly used theoretical method for investigating the mechanical properties of nanostructures [52, 53, 11]. To obtain the response to applied external loading the distance between atoms at the edges of the structures are constrained while allowing the rest of the structure to relax. The distance between the atoms on either side, marked in green in figures 4.3 and 4.4, was increased in a step wise manner to introduce strain. These atoms were simultaneously constrained to lie in the same plane to prevent twisting of the molecules. The distance between the edges was increased until the molecule fragmented. This is an application of the COGEF [21] method discussed earlier. The total energy of the structure and the magnitude of the force vector are calculated at each step such that the peak restorative force could then be determined.

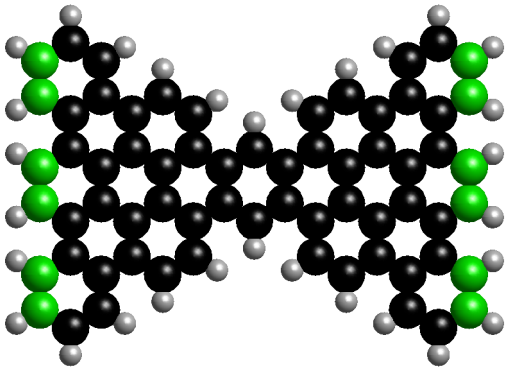

Figure 4.4: The fully benzenoid fragment with carbon atoms shown in black, hydrogen in white and the constrained carbon atoms shown in green.

The broken bonds were determined by visual inspection of the structures so that the correct interatomic distances could be recorded for the entire simulation.
To obtain values for the peak force and bond failure distance for conjugated π-bonds two bow-tie shaped fragments were tested using the method described above. The bow-tie shape was chosen because shifting the outermost atoms strains the molecule with the greatest strain occurring in the narrowest section. This produces failure at the narrowest portion of the fragment with as few bonds undergoing scission as possible. The first bow-tie molecule considered, referred to as 'Clar's goblet' and shown in figure 4.3, exhibits magnetic behaviour with the ground state predicted to consist of the two sides of the molecule to be antiferromagnetically coupled due to the superexchange mechanism [54]. The second bow-tie fragment, shown in figure 4.4 is fully benzenoid, unlike Clar's Goblet, and thus similar to many graphene nanostructures, such as graphene and certain graphene nanoribbons.
For the DFTB calculations of Clar's Goblet the initial atomic spins must be set such that the initial state is ferromagnetic (FM), antiferromagnetic (AFM) or non-magnetic (NM) (i.e. closed shell). The FM and AFM states are caused by two spatially-separated singly-occupied orbitals. The electrons in these orbitals have parallel or anti-parallel spins. The NM state is formed by allowing the calculation to find a spin paired configuration. DFTB3 spin density plots for the AFM and FM states are shown in figures 4.5 and 4.6 respectively. The AFM state was enforced during the DFTB scans by setting the initial spin values at the start of each structural optimisation step. The FM and NM states were simulated by setting the number of unpaired electrons to two and zero respectively. It was found that as the strain across the molecule increases the wavefunction would adopt a NM spin-paired configuration. This was not an issue for the FM state as it can be generated using the method described above and fixing the total spin. However, as the total spin for the AFM and NM states were both zero it was not possible to prevent the

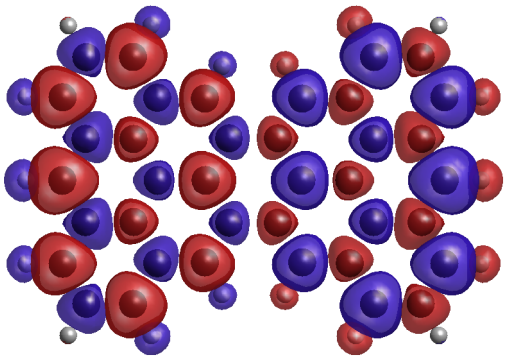

Figure 4.5: Spin density at an isovalue of 0.0004 for Clar's goblet for the AFM coupled configuration calculated using DFTB3 with spin-up shown in blue and spin-down in red. The carbon atoms are shown in black and hydrogen atoms in white. The AFM coupling is shown by the greater spin-down density on the left and greater spin-up on the right hand side of the molecule.

applied AFM state from converting to a NM state during an optimisation.
Simulations of both the AFM and FM state of the Clar's goblet structure were also performed using DFT with the PBE functional. The FM state is readily calculated by setting the number of unpaired electrons to two. Obtaining the AFM ground state required performing a spin restricted calculation and then checking the stability of the resulting wavefunction using the keyword 'stable' in the Gaussian program. The stability check relaxes constraints on the wavefunction, finds the instability and generates the lower energy antiferromagnetic eigenstate. This can then be re-optimised and used as an initial guess for the following pseudo static tensile simulation.
Not all methods were applied to every structure investigated due to computational cost. Specifically, the bow-tie fragment simulations were performed using based DFT. CASSCF was used for calculations of ethane and ethene only.

4.3 Results and discussion

4.3.1 Single bonds

The predicted peak restorative forces for the carbon-carbon single bonds studied are presented in table 4.1 and the corresponding bond lengths listed in table 4.2. The DFT and MP2 calculations produced fairly consistent predictions for the failure bond length ≈ 1.95 Å but the difference in peak force is about 12% between the PBE and MP2 results. Both MP2 and B2PLYPD3 methods incorporate similar terms for the correlation energy and results from both of these show higher restorative forces than those from PBE and B3LYP. The CASSCF calculation was performed using fourteen electrons and fourteen orbitals such that all valence electrons and bonding and corresponding antibonding or-

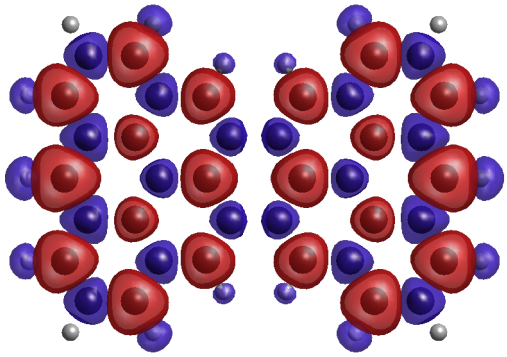

Figure 4.6: Spin density at an isovalue of 0.0004 for Clar's goblet with FM coupling calculated using DFTB3 with spin-up shown in blue and spin-down in red.

Table 4.1: Peak restoring forces for carbon-carbon single bond simulations (nN).

Method	Ethane	Butane	Isobutane	Butene	Isobutene
REBO	43.09	38.58	36.52	48.39	50.59
AIREBO	4.90	4.89	4.88	5.24	5.36
ReaxFF	11.05	16.05	33.34	12.20	16.08
DFTB3	6.70	6.35	5.94	6.85	6.56
PBE	5.89	5.71	5.50	6.38	6.08
B3LYP	6.05	5.90	5.70	6.57	6.30
B2PLYPD3	6.20	6.04	5.87	6.74	6.51
MP2	6.59	6.43	6.30	7.09	6.86
CASSCF(14,14)	5.83	-	-	-	-

bitals were included. The CASSCF result is remarkably similar to that calculated using the PBE functional but with a significantly lower peak force than the MP2 calculation. This suggests that the dynamic correlation recovered by MP2 is of less importance for the peak force value compared to the static correlation recovered by CASSCF.

The orthogonal electronic structure methods also show the same trends based on the number of carbon atoms bonded to the two atoms involved in the bond extension. For molecules involving single order carbon-carbon bonds the two primary carbon atoms in ethane generate the strongest restorative force, followed by the primary-secondary bond in butane and then the primary-tertiary bond in isobutane. The same pattern is seen with butene and isobutene but the double bond in these molecules seems to increase the maximum restorative force.

The peak forces were also compared against bond dissociation energies (BDEs) calculated at the MP2/CC-PVTZ level of theory. The BDEs mostly followed the same trends as the peak forces except for ethane having a marginally lower BDE than butane ($\approx 0.004eV$). These trends are displayed graphically in figure 4.7.

Table 4.2: Bond length at peak force for carbon-carbon single bond simulations in (Å).

Method	Ethane	Butane	Isobutane	Butene	Isobutene
REBO	1.84	1.84	1.82	1.84	1.84
AIREBO	1.88	1.88	1.89	1.85	1.85
ReaxFF	1.98	2.07	2.07	1.83	1.89
DFTB3	1.96	1.96	1.96	1.93	1.94
PBE	1.97	1.96	1.96	1.94	1.94
B3LYP	1.98	1.97	1.97	1.95	1.95
B2PLYPD3	1.96	1.94	1.94	1.93	1.93
MP2	1.98	1.97	1.97	1.94	1.94
CASSCF(14,14)	1.98	-	-	-	-

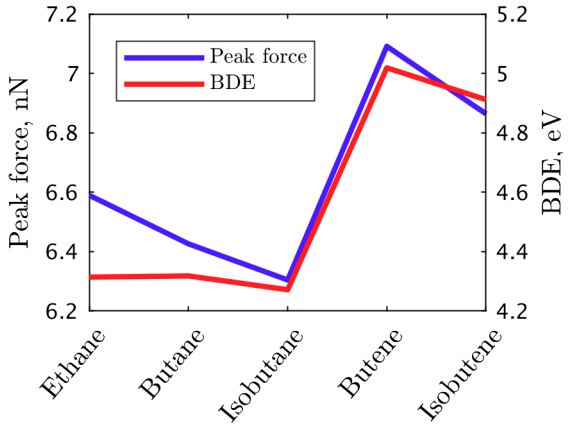

Figure 4.7: The peak force and the BDE for the single bond dissociations as calculated using MP2/CC-PVTZ.

The REBO values are taken from the unmodified REBO potential where the energy cutoff function introduces spurious overbinding. The onset of this is evident from the graph in figure 4.8 where the energy contribution of the carbon-carbon bond is forced to zero from 1.7 Å to 2.0 Å. The switching mechanism used to provide a smooth cutoff for the energy results in a non-physical gradient. The alternative method, AIREBO, has the cutoff function removed, which results in a discontinuity of the energy at 2.0 Å, see figure 4.8(a). The AIREBO data does show a weaker restorative force than the electronic structure methods but it appears to vary with the environment of the stretched bond in a similar manner to the higher-order methods. The peak force for the single bonds in butene and isobutene as calculated by AIREBO is clearly greater than the other molecules. This is in agreement with the results calculated using electronic structure methods but these show a larger increase in peak force for these molecules compared with AIREBO. ReaxFF generates very poor forces in comparison to the *ab initio* methods and indeed struggles to produce reasonable energy curves as can be seen in figure 4.9. The cause of the erroneous peak in the force at approximately 1.25 Å for ethane is the bond order calculation used

in ReaxFF. The double π-bond term in the total bond order formula used in ReaxFF is forced to zero in this region which produces a sharp peak in the negative gradient of the bond order. After the minimum energy at 1.59 Å in figure 4.9, the magnitude of the force rises steadily before reaching a plateau followed by a peak at 2.0 Å. This non-physical behaviour appears due to the bond order switching function as first the π-bond term and then the σ-bond terms are forced to zero. The switching of these terms occurs over a longer range of bond distances than the double π-bond term and so the peaks in the force caused by these terms are less pronounced.
Only results for DFTB3 are given due to erroneous forces present in the SCC-DFTB results which can be seen in figure 4.10. The earlier parameter sets used in non-DFTB3 calculations produce misshapen force displacement plots with a double peak characteristic. The cause of this behaviour is the repulsive potential, a sum of pairwise interaction terms which includes ionic repulsion and exchange-correlation contributions among others, used within the DFTB parameter sets. This can be considered the DFTB analogue for the exchange correlation functional of DFT [55]. The repulsive potential is calculated as the difference between the sum of the tight-binding band structure and Coulomb energies and a total energy calculated from higher accuracy calculations. This potential is then represented as an exponential function at short range, then a series of cubic splines at intermediate distances and finally a fifth order spline at larger separations. The role of the fifth order spline is to provide continuous first and second derivatives with the preceding cubic spline and to force the potential and its first and second derivatives to zero at some cut off distance. The fifth order spline used in earlier DFTB parameter sets cause erroneous, albeit continuous, force curves. The DFTB3 results do show slightly higher restorative forces than the higher order electronic structure methods but the location of the peaks are in good agreement. The environment of the bond appears to influence the restorative forces calculated using DFTB3 in a similar manner to the higher order electronic structure calculations. All the results show some environment-dependent variation of the failure bond length for single bonds and there is a similar variation across the different methods.

4.3.2 Double bonds

The predicted peak restorative forces for doubly bonded carbon atoms are presented in table 4.3 and the corresponding bond lengths at which they occur are in table 4.4. DFT and MP2 calculations predict fairly consistent bond failure lengths of $\approx$ 1.73 Å for the double bonds. PBE and B3LYP results indicate a longer failure bond length for the double bond simulations than MP2 and B2PLYPD3. The peak forces of B3LYP are consistently greater than the other DFT functional and MP2 calculations. The CASSCF calculation of ethene shows a lower peak force than all the other electronic structure methods investigated here. The results show that single reference methods may overestimate peak restorative forces but will predict the corresponding bond lengths

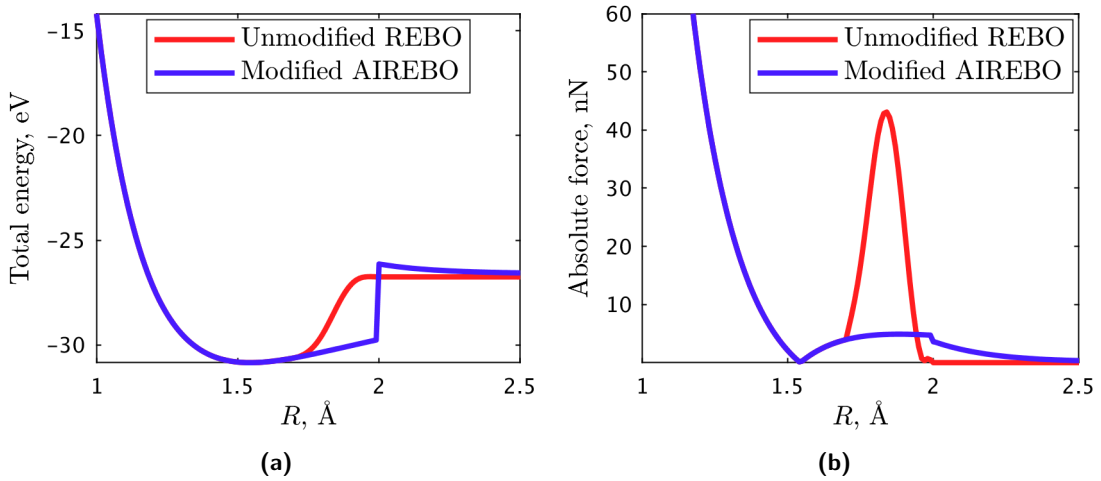

Figure 4.8: Energy (a) and force (b) plotted as functions of internuclear separation for the carbon-carbon bond in ethane calculated using both the original and modified REBO potentials. The overbinding caused by the energy cutoff function can be seen in the REBO result and the discontinuous energy can be seen in the AIREBO result.

Table 4.3: Peak restoring forces for carbon-carbon double bond simulations (nN).

Method	Ethene	Butene	Isobutene
REBO	55.62	32.31	36.31
AIREBO	9.52	9.66	9.72
ReaxFF	30.07	24.37	25.48
DFTB3	13.90	12.98	12.92
PBE	13.04	12.35	12.23
B3LYP	13.80	13.19	13.10
B2PLYPD3	13.17	12.69	12.68
MP2	12.83	12.29	12.64
CASSCF(12,12)	12.03	-	-

correctly to within a few percent.

The BDEs follow a similar trend to the peak force calculations, as shown in figure 4.11. The peak forces and BDEs are both larger than the those for single bonds.

The AIREBO results underestimate the bond strength and failure bond lengths for double bonds, as it did for the single bonds. The other potentials massively overestimate the restorative forces and fail to reproduce the failure bond lengths seen in DFT or MP2.

4.3.3 Larger hydrocarbon molecules

The restoring force between a pair of central carbon atoms was calculated by projecting the applied force on to the vector connecting the two carbon nuclei, then taking half of its magnitude. The applied force was determined as the vector sum of the forces on the constrained atoms on one side of the molecule and the factor of a half is due to the force

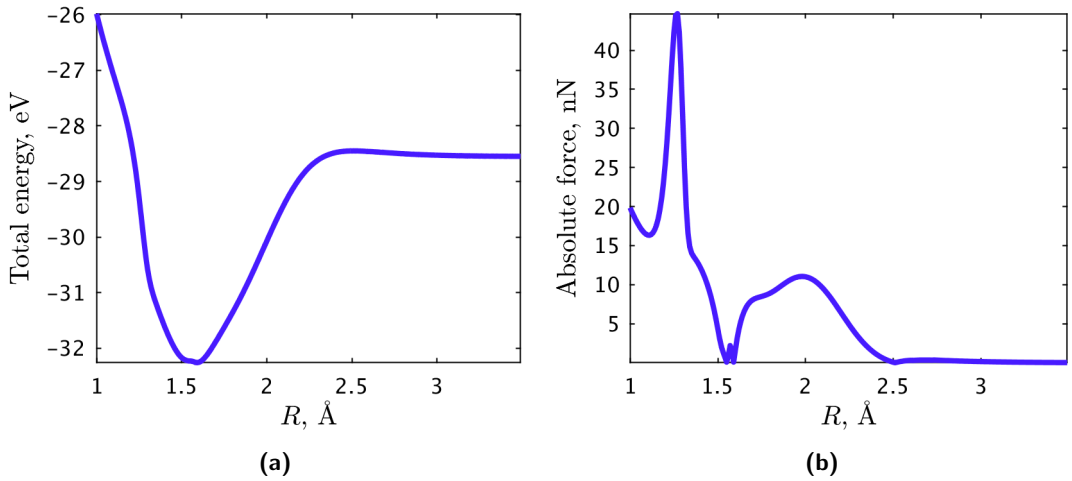

Figure 4.9: Energy and force plotted as functions of internuclear separation for the carbon-carbon bond in ethane calculated using ReaxFF. The poor approximation of the energy curve results in an even worse approximation of the forces.

Table 4.4: Bond length at peak force for carbon-carbon double bond simulations (Å).

Method	Ethene	Butene	Isobutene
REBO	1.83	1.78	1.79
AIREBO	1.60	1.59	1.59
ReaxFF	1.59	1.60	1.61
DFTB3	1.71	1.72	1.73
PBE	1.75	1.74	1.75
B3LYP	1.75	1.74	1.74
B2PLYPD3	1.72	1.72	1.73
MP2	1.71	1.71	1.75
CASSCF(12,12)	1.73	-	-

being transmitted by two bonds at the centre of the molecule.

The simulations of Clar's Goblet found almost identical peak restorative force values and failure bond lengths for both the AFM and FM states as calculated using PBE based DFT. The ground state for this molecule was found to be the AFM state with an energy difference between the AFM and FM states to be 20 meV using PBE, which is in agreement with other work [56]. The energy of the NM state was found to be $\approx$ 150 meV higher than the magnetic states for PBE based calculations. DFTB3 did correctly predict the ground state to be AFM but only by 3 meV compared to the FM state and by $\approx$ 80 meV compared to the NM state. The peak restorative force in the FM state was 0.04 nN lower than the AFM state and the failure bond length was a negligible 0.004 Å longer. Since the differences in the calculated values for these two states are very small only the AFM result is listed. The difference in energy between the FM and AFM states decreases as the bonds are stretched and tend to zero at the point where the

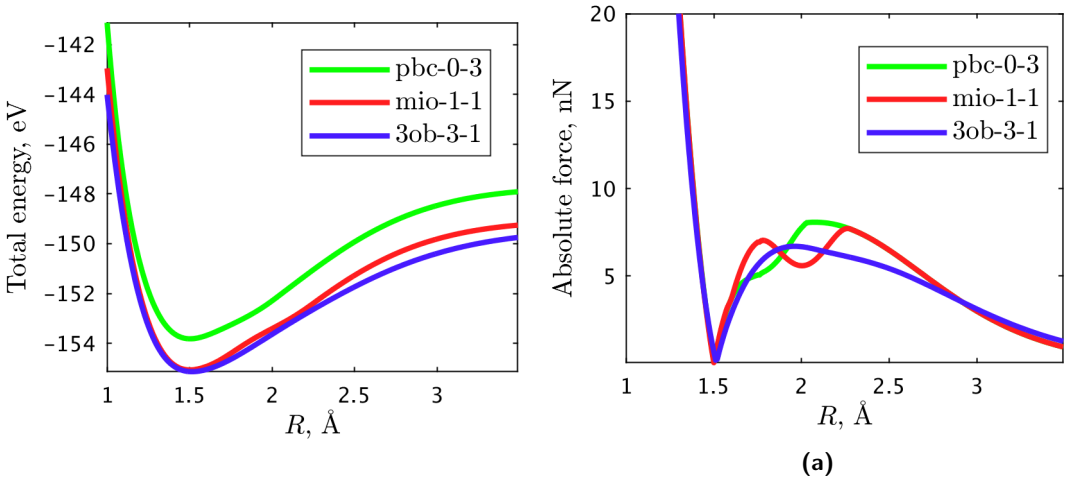

Figure 4.10: Energy and force plotted as functions of internuclear separation for the carbon-carbon bond in ethane calculated using different DFTB variants. The poor approximation of the energy curve results in an even worse approximation of the forces.

Table 4.5: Peak restorative force for conjugated π-bond simulations in nN.

Method	Clar's Goblet (AFM)	Benzenoid bow-tie
AIREBO	8.10	7.38
ReaxFF	14.22	16.40
DFTB3	7.47	7.27
PBE	7.92	-

molecule fragments.

ReaxFF fails to produce reasonable forces even though it does predict a reasonable bond length of 1.48 Å for the central carbon-carbon bonds when the molecule is in static equilibrium. However, the failure bond length was shorter than the DFTB3 and PBE results. When the central bonds fail in these calculations the two halves of the structure relaxe such that the now undercoordinated carbon atoms on each fragment moved towards each other. The potential appears to compensate for the undercoordination rather than maintain the hexagonal lattice by allowing carbon atoms to adopt a radical character. In contrast, the final structures generated using AIREBO did.

AIREBO and ReaxFF cacluations were hampered by discontinuities in the forces over the range of bond lengths investigated in the simulations. To combat this the stepwise COGEF method was adapted by shifting all the atoms on one side of the centre of the molecule in a step wise manner and then allowing the structure to relax. Furthermore, the *fire* [57] damped dynamics minimiser method was employed as it located minima that the conjugate gradient method did not. The relaxed structure generated with AIREBO predicted the optimised bond length at equilibrium of the central bonds as 1.413 Å which is not in agreement with the other methods; both PBE and DFTB3 geometries predicted

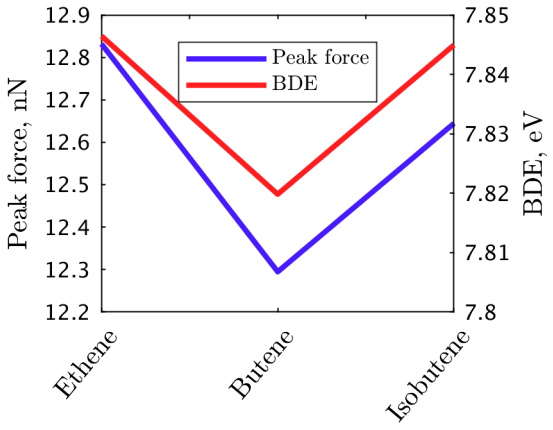

Figure 4.11: The peak force and the BDE for the double bond dissociations calculated using MP2/CC-PVTZ.

Table 4.6: Bond length at peak force for conjugated π-bond simulations in Å.

Method	Clar's Goblet (AFM)	Benzenoid bow-tie
AIREBO	1.688	1.685
ReaxFF	1.845	1.885
DFTB3	1.862	1.840
PBE	1.860	-

bond lengths of $\approx$ 1.475 Å. This introduces a bias when comparing the results from different methods which can be removed by considering the strain to failure, i.e. the increase of the bond length at failure divided by the relaxed bond length. The strains to failure for AIREBO, PBE and DFTB3 are 0.207, 0.261 and 0.262 respectively. The AIREBO peak restorative force was lower than the DFT and DFTB3 calculated values but not as severely as in the single and double bond calculations.

AIREBO and DFTB3 show a weakening of the central bonds between the benzenoid bow tie fragment and Clar's goblet. This is most likely due to the central bonds of Clar's Goblet being parallel to the direction of the applied force whereas the benzenoid bowtie's central bonds are not.

The DFTB3 results show a marginally lower peak force than the PBE based calculations. The difference between the results for the AFM and FM states was, as for the PBE results, negligible. It is worth noting that the DFTB3 parametrisation relies on both PBE based DFT and coupled cluster CCSD(T) calculations. Such higher order calculations capture significant electron correlation and it may be that the DFTB3 parametrisation produces more accurate values than PBE. Testing this possibility lies beyond the scope of this work.

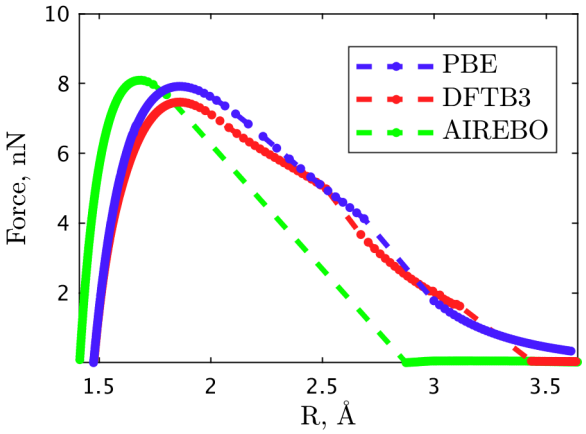

Figure 4.12: The magnitude of the force as a function of the mean central carbon-carbon bond length, i.e. the bonds that break, for the Clar's goblet structure. The individual data points are represented by filled circles with the dashed lines connecting the points becoming visible when the bond length has changed significantly during an optimisation step. This is particularly obvious with the AIREBO results due to the potentials hard cutoff that removes all restorative forces beyond the cutoff distance.

4.4 Conclusions

This work has provided some benchmark data for predictions of bond dissociation and investigated molecular properties relevant to structural property prediction. Peak restorative forces, an analogue for mechanical strength, and the bond lengths at which they occur have been calculated for a range of carbon-carbon bonds occurring in a variety of different molecules. The type and environment of the bond effects the peak restorative force and the bond failure length.

Single bonds between two carbon atoms, where one of these atoms is doubly bonded to a third atom, show greater restorative forces and slightly shorter bond failure lengths compared to carbon atoms involved in only single bonds. There was some indication that the peak restorative forces of single bonds involving a primary carbon atom decreased as the number of carbon-carbon bonds for the other atom increased. The peak restorative forces increased and the failure bond lengths decreased with the bond order. The BDE did vary in the same way as peak force in most instances but by itself does not appear to provide a method to determine the peak restorative force.

The unmodified REBO and the ReaxFF force displacement curves show significant errors and cannot be relied upon for simulations of nanostructures under stretch to failure type conditions. The modified AIREBO results show lower peak restorative forces and shorter failure bond lengths compared to the electronic structure methods for all bond types considered. Although the modified potential may not provide accurate quantitative results the qualitative behaviour seen in this work was superior to ReaxFF. The main issue with AIREBO is that inclusion of the switching function produces erroneous results but its removal creates discontinuous energies and forces. By setting the restorative force

to zero at an arbitrary cutoff the potential will struggle to produce reliable behaviour in situations where a bond might break but the atoms involved in the bond are still held relatively close together. Although ReaxFF failed to produce reasonable force displacement curves it did manage to reproduce relaxed structures that were comparable to the electronic structure methods. Overall the results show DFTB3 and the higher order electronic structure methods are in reasonable agreement, producing qualitatively similar variations of the measured properties due to bond type and environment.
Prediction of the forces between atomic nuclei is extremely difficult. Molecular mechanics potentials, which are computationally cheap enough for reasonably sized nanostructures, can suffer from non-physical behaviour either due to discontinuous energies and gradients or due to poor choice of switching functions. Even complex and computationally expensive electronic structure calculations struggle to agree with each other over large ranges of internuclear separation. Parametrised methods such as DFTB3 can produce reasonable results in comparison to higher order methods but only if the parametrisation is performed with care.
This work has shown that there are many methods that can be used for the prediction of the mechanical strength of hydrocarbon molecules and nanostructures. Through comparison of different methods applied to different molecules it has been shown that an acceptable prediction of a molecules mechanical strength can be made at a reasonable computational cost.

Bibliography

[1] M. Tolladay, N. Allan, D. Ivanov, and F. Scarpa. Atomistic modelling of hydrocarbon nanostructure failure. In P. Ribeiro, L. Stefano, and S. Adhikari, editors, *Proceedings of EUROMECH Colloquium 603: Dynamics of micro and nano electromechanical systems, Porto, Portugal, September 5-7, 2018.*, pages "28–31". Universidade do Porto. Reitoria, 2018.

[2] J. D. Baran, C. Eames, K. Takahashi, M. Molinari, M. S. Islam, and S. C. Parker. Structural, Electronic, and Transport Properties of Hybrid SrTiO3-Graphene and Carbon Nanoribbon Interfaces. *Chemistry of Materials*, 29(17):7364–7370, 2017.

[3] J. N. Hart, S. C. Parker, and A. A. Lapkin. Energy Minimization of Single-Walled Titanium Oxide Nanotubes. *ACS Nano*, 3(11):3401–3412, 2009.

[4] D. Cohen-Tanugi and J. C. Grossman. Water Desalination across Nanoporous Graphene. *Nano Letters*, 12(7):3602–3608, 2012.

[5] H. Kim, K. Lee, S. I. Woo, and Y. Jung. On the mechanism of enhanced oxygen reduction reaction in nitrogen-doped graphene nanoribbons. *Physical Chemistry Chemical Physics*, 13(39):17505, 2011.

[6] M. A. Rafiee, W. Lu, A. V. Thomas, A. Zandiatashbar, J. Rafiee, J. M. Tour, and N. a. Koratkar. Graphene Nanoribbon Composites. *ACS Nano*, 4(12):7415–7420, 2010.

[7] J. Tersoff. New empirical approach for the structure and energy of covalent systems. *Physical Review B*, 37(12):6991–7000, 1988.

[8] D. W. Brenner. Empirical potential for hydrocarbons for use in simulating the chemical vapor deposition of diamond films. *Physical Review B*, 42(15):9458–9471, 1990.

[9] A. C. T. van Duin, S. Dasgupta, F. Lorant, and W. A. Goddard. ReaxFF: A Reactive Force Field for Hydrocarbons. *The Journal of Physical Chemistry A*, 105(41):9396–9409, 2001.

[10] H. Zhao, K. Min, and N. R. Aluru. Size and Chirality Dependent Elastic Properties of Graphene Nanoribbons under Uniaxial Tension. *Nano Letters*, 9(8):3012–3015, 2009.

[11] Q. Lu, W. Gao, and R. Huang. Atomistic simulation and continuum modeling of graphene nanoribbons under uniaxial tension. *Modelling and Simulation in Materials Science and Engineering*, 19(5):054006, 2011.

[12] R. Bizao, T. Botari, E. Perim, N. Pugno, and D. Galvao. Mechanical properties and fracture patterns of graphene (graphitic) nanowiggles. *Carbon*, 119:431–437, 2017.

[13] H. Zhao and N. R. Aluru. Temperature and strain-rate dependent fracture strength of graphene. *Journal of Applied Physics*, 108(6):064321, 2010.

[14] K. Kim, V. I. Artyukhov, W. Regan, Y. Liu, M. F. Crommie, B. I. Yakobson, and A. Zettl. Ripping Graphene: Preferred Directions. *Nano Letters*, 12(1):293–297, 2012.

[15] T. Zhang, X. Li, S. Kadkhodaei, and H. Gao. Flaw Insensitive Fracture in Nanocrystalline Graphene. *Nano Letters*, 12(9):4605–4610, 2012.

[16] A. Dutta and C. D. Sherrill. Full configuration interaction potential energy curves for breaking bonds to hydrogen: An assessment of single-reference correlation methods. *The Journal of Chemical Physics*, 118(4):1610–1619, 2003.

[17] M. F. Iozzi, T. Helgaker, and E. Uggerud. Assessment of theoretical methods for the determination of the mechanochemical strength of covalent bonds. *Molecular Physics*, 107(23-24):2537–2546, 2009.

[18] G. S. Kochhar, A. Bailey, and N. J. Mosey. Competition between Orbitals and Stress in Mechanochemistry. *Angewandte Chemie International Edition*, 49(41):7452–7455, 2010.

[19] G. S. Kedziora, S. A. Barr, R. Berry, J. C. Moller, and T. D. Breitzman. Bond breaking in stretched molecules: multi-reference methods versus density functional theory. *Theoretical Chemistry Accounts*, 135(3):79, 2016.

[20] M. Grandbois, M. Beyer, M. Rief, H. Clausen-Schaumann, and H. E. Gaub. How strong is a covalent bond? *Science (New York, N.Y.)*, 283(5408):1727–30, 1999.

[21] M. K. Beyer. The mechanical strength of a covalent bond calculated by density functional theory. *The Journal of Chemical Physics*, 112(17):7307–7312, 2000.

[22] S. Zou, H. Schönherr, and G. J. Vancso. Stretching and rupturing individual supramolecular polymer-chains by AFM. *Angewandte Chemie - International Edition*, 44(6):956–959, 2005.

[23] C. R. Hickenboth, J. S. Moore, S. R. White, N. R. Sottos, J. Baudry, and S. R. Wilson. Biasing reaction pathways with mechanical force. *Nature*, 446(7134):423–427, 2007.

[24] S. L. Potisek, D. A. Davis, N. R. Sottos, S. R. White, and J. S. Moore. Mechanophore-Linked Addition Polymers. *Journal of the American Chemical Society*, 129(45):13808–13809, 2007.

[25] D. A. Davis, A. Hamilton, J. Yang, L. D. Cremar, D. Van Gough, S. L. Potisek, M. T. Ong, P. V. Braun, T. J. Martínez, S. R. White, J. S. Moore, and N. R. Sottos. Force-induced activation of covalent bonds in mechanoresponsive polymeric materials. *Nature*, 459(7243):68–72, 2009.

[26] J. Ribas-Arino, M. Shiga, and D. Marx. Understanding Covalent Mechanochemistry. *Angewandte Chemie International Edition*, 48(23):4190–4193, 2009.

[27] H. S. Smalø and E. Uggerud. Breaking covalent bonds using mechanical force, which bond breaks? *Molecular Physics*, 111(9-11):1563–1573, 2013.

[28] T. Stauch and A. Dreuw. A quantitative quantum-chemical analysis tool for the distribution of mechanical force in molecules. *The Journal of Chemical Physics*, 140(13):134107, 2014.

[29] S. M. Avdoshenko and D. E. Makarov. Finding mechanochemical pathways and barriers without transition state search. *The Journal of Chemical Physics*, 142(17):174106, 2015.

[30] J. P. Perdew, K. Burke, and M. Ernzerhof. Generalized Gradient Approximation Made Simple. *Physical Review Letters*, 77(18):3865–3868, 1996.

[31] C. Lee, W. Yang, and R. G. Parr. Development of the Colle-Salvetti correlation-energy formula into a functional of the electron density. *Physical Review B*, 37(2):785–789, 1988.

[32] A. D. Becke. Density-functional thermochemistry. III. The role of exact exchange. *The Journal of Chemical Physics*, 98(7):5648–5652, 1993.

[33] S. Grimme. Semiempirical hybrid density functional with perturbative second-order correlation. *The Journal of Chemical Physics*, 124(3):034108, 2006.

[34] C. Møller and M. S. Plesset. Note on an Approximation Treatment for Many-Electron Systems. *Physical Review*, 46(7):618–622, 1934.

[35] M. J. Frisch, G. W. Trucks, H. B. Schlegel, G. E. Scuseria, M. A. Robb, J. R. Cheeseman, G. Scalmani, V. Barone, B. Mennucci, G. A. Petersson, H. Nakatsuji, M. Caricato, X. Li, H. P. Hratchian, A. F. Izmaylov, J. Bloino, G. Zheng, J. L. Sonnenberg, M. Hada, M. Ehara, K. Toyota, R. Fukuda, J. Hasegawa, M. Ishida, T. Nakajima, Y. Honda, O. Kitao, H. Nakai, T. Vreven, J. A. Montgomery, Jr., J. E. Peralta, F. Ogliaro, M. Bearpark, J. J. Heyd, E. Brothers, K. N. Kudin, V. N. Staroverov, T. Keith, R. Kobayashi, J. Normand, K. Raghavachari, A. Rendell, J. C. Burant, S. S. Iyengar, J. Tomasi, M. Cossi, N. Rega, J. M. Millam, M. Klene, J. E. Knox, J. B. Cross, V. Bakken, C. Adamo, J. Jaramillo, R. Gomperts, R. E. Stratmann, O. Yazyev, A. J. Austin, R. Cammi, C. Pomelli, J. W. Ochterski, R. L. Martin, K. Morokuma, V. G. Zakrzewski, G. A. Voth, P. Salvador, J. J. Dannenberg, S. Dapprich, A. D. Daniels, O. Farkas, J. B. Foresman, J. V. Ortiz, J. Cioslowski, , and D. J. Fox. Gaussian 09, Revision D.01, 2013. Gaussian Inc. Wallingford CT.

[36] T. H. Dunning. Gaussian basis sets for use in correlated molecular calculations. I. The atoms boron through neon and hydrogen. *The Journal of Chemical Physics*, 90(2):1007–1023, 1989.

[37] C. Cornwell and L. Wille. Elastic properties of single-walled carbon nanotubes in compression. *Solid State Communications*, 101(8):555–558, 1997.

[38] Y. Liu and X. Chen. Mechanical properties of nanoporous graphene membrane. *Journal of Applied Physics*, 115(3):034303, 2014.

[39] V. Verma, V. K. Jindal, and K. Dharamvir. Elastic moduli of a boron nitride nanotube. *Nanotechnology*, 18(43):435711, 2007.

[40] N. M. Anoop Krishnan and D. Ghosh. Chirality dependent elastic properties of single-walled boron nitride nanotubes under uniaxial and torsional loading. *Journal of Applied Physics*, 115(6):064303, 2014.

[41] D. W. Brenner, O. A. Shenderova, J. A. Harrison, S. J. Stuart, B. Ni, and S. B. Sinnott. A second-generation reactive empirical bond order (REBO) potential energy expression for hydrocarbons. *Journal of Physics: Condensed Matter*, 14(4):783–802, 2002.

[42] J. D. Gale. GULP: A computer program for the symmetry-adapted simulation of solids. *Journal of the Chemical Society, Faraday Transactions*, 93(4):629–637, 1997.

[43] S. J. Stuart, A. B. Tutein, and J. A. Harrison. A reactive potential for hydrocarbons with intermolecular interactions. *The Journal of Chemical Physics*, 112(2000):6472–6486, 2000.

[44] S. Plimpton. Fast Parallel Algorithms for Short-Range Molecular Dynamics. *Journal of Computational Physics*, 117(1):1–19, 1995.

[45] O. A. Shenderova, D. W. Brenner, A. Omeltchenko, X. Su, and L. H. Yang. Atomistic modeling of the fracture of polycrystalline diamond. *Physical Review B*, 61(6):3877–3888, 2000.

[46] B. Aradi, B. Hourahine, and T. Frauenheim. DFTB+, a sparse matrix-based implementation of the DFTB method. *Journal of Physical Chemistry A*, 111(26):5678–5684, 2007.

[47] D. Porezag, T. Frauenheim, T. Köhler, G. Seifert, and R. Kaschner. Construction of tight-binding-like potentials on the basis of density-functional theory: Application to carbon. *Physical Review B*, 51(19):12947–12957, 1995.

[48] G. Seifert, D. Porezag, and T. Frauenheim. Calculations of molecules, clusters, and solids with a simplified LCAO-DFT-LDA scheme. *International Journal of Quantum Chemistry*, 58(2):185–192, 1996.

[49] M. Elstner, D. Porezag, G. Jungnickel, J. Elsner, M. Haugk, T. Frauenheim, S. Suhai, and G. Seifert. Self-consistent-charge density-functional tight-binding method for simulations of complex materials properties. *Physical Review B*, 58(11):7260–7268, 1998.

[50] Y. Yang, H. Yu, D. York, Q. Cui, and M. Elstner. Extension of the self-consistent-charge density-functional tight-binding method: Third-order expansion of the density functional theory total energy and introduction of a modified effective coulomb interaction. *Journal of Physical Chemistry A*, 111(42):10861–10873, 2007.

[51] M. Gaus, A. Goez, and M. Elstner. Parametrization and Benchmark of DFTB3 for Organic Molecules. *Journal of Chemical Theory and Computation*, 9(1):338–354, 2013.

[52] R. Faccio, P. a. Denis, H. Pardo, C. Goyenola, and Á. W. Mombrú. Mechanical properties of graphene nanoribbons. *Journal of Physics: Condensed Matter*, 21(28):285304, 2009.

[53] Y. Gao and P. Hao. Mechanical properties of monolayer graphene under tensile and compressive loading. *Physica E: Low-Dimensional Systems and Nanostructures*, 41(8):1561–1566, 2009.

[54] O. V. Yazyev. Emergence of magnetism in graphene materials and nanostructures. *Reports on Progress in Physics*, 73(5):056501, 2010.

[55] P. Koskinen and V. Mäkinen. Density-functional tight-binding for beginners. *Computational Materials Science*, 47(1):237–253, 2009.

[56] W. L. Wang, O. V. Yazyev, S. Meng, and E. Kaxiras. Topological Frustration in Graphene Nanoflakes: Magnetic Order and Spin Logic Devices. *Physical Review Letters*, 102(15):157201, 2009.

[57] E. Bitzek, P. Koskinen, F. Gähler, M. Moseler, and P. Gumbsch. Structural Relaxation Made Simple. *Physical Review Letters*, 97(17):170201, 2006.

Chapter 5

Mechanical properties of graphene nanoribbons

5.1 Introduction

Two of the most remarkable features of graphene nanoribbons are their exceptionally high stiffness and tensile strength. Testing these properties experimentally is challenging but not impossible [1]. However, reliable simulation methods provide a fast and relatively straightforward method for determining these quantities. If such simulations can be shown to provide reliable results for pre-existing structures then they can also be used for exploring the design space for any novel nanostructure that can be imagined. These computational tools also provide the ability to examine the effect of defects which can allow for further characterisation of experimentally derived structures.

Chapter 4 investigated and benchmarked simulation tools that would be suitable for performing simulations of nanostructures, containing large numbers of atoms, undergoing tensile failure. This work has found two applicable methods: the modified AIREBO potential and DFTB3. Both of these methods are inexact but the nature of material failure is extremely problematic even for very costly electronic structure methods. AIREBO is computationally cheap and can provide reasonable qualitative results. It does underestimate the bond strength and strain at failure of carbon-carbon bonds but the structures break in a manner consistent with electronic structure methods. DFTB3 provides quantitative results that are closer to the more computationally costly methods than AIREBO but it does so at greater computational expense.

Other investigations into the mechanical properties of graphene nanoribbons and other nanostructures have relied heavily on the REBO and AIREBO potentials for their simulations [2, 3, 4, 5, 6, 7]. These calculations invariably use dynamically applied strain with periodic boundaries to simulate an infinite nanostructure undergoing extension at some predefined strain rate. Such molecular dynamics simulations require very short time steps which in turn places constraints on the possible applicable strain rates. It is

not uncommon to see strain rates of 10^{-3} $ps^{-1} \equiv 10^{9}$ s^{-1} [6] or greater [4, 8] which is well beyond what is experimentally accessible [9]. However, it is possible to use quasi-static simulations [5] where the structure is allowed to relax after each application of strain. Electronic structure calculations have been used to calculate elastic moduli and Poisson's ratios [10] of nanoribbons as well as determining mechanical strengths [11, 12, 13].

Nanoribbons are generally divided in to two main categories, 'armchair' and 'zig-zag', where 'armchair' and 'zig-zag' describe the edge shape of the ribbon. These types of nanoribbons are further described by an index which describes the numbers of carbon-carbon dimer pairs across the width of the ribbon, as shown in figure 5.1. Other nanoribbon types have also been defined such as 'chiral', which involves a complex edge that alternates between zig-zag and armchair edges, and several experimentally derived forms known as 'chevron-type, 'cove-type' and 'para-armchair'. Although the zig-zag and armchair ribbons have been studied extensively theoretically it is not possible to confirm the results experimentally as the dependence of the calculated quantities, such as bandgaps, are highly sensitive to ribbon width and edge shape [14]. Most attempts to produce GNRs relied on top down approaches that could not provide sufficient control over the width and edge geometry [15, 16, 17, 18]. The development of a bottom up production method using on surface self assembly of precursor molecules followed by a dehydrogenation step [19] has managed to produce some atomically precise GNR structures. The first reported results [19] demonstrated the successful production of an armchair ribbon of constant width and a new form of GNR referred to as chevron-type graphene nanoribbons (CT-GNRs). The technique that yielded these structures has been explored experimentally by employing different precursors in order to generate different types of nanoribbon. These studies have managed to produce a zig-zag nanoribbon [20], several more armchair ribbons and also several other experimentally derived nanoribbon structures called cove-type [21] and para-armchair [22] ribbons.

The purpose of this chapter is to investigate the mechanical properties of various GNR structures. The computation methods used in this work and the reasons for choosing them are discussed. The influence of the size of the unit cell is investigated to ensure the simulation results are robust. A set of armchair, zig-zag and the experimentally derived GNR structures are then modelled under the effect on uniaxial tensile strain to determine their effective Young's modulus, tensile strength and strain at failure. A relationship between the index of AGNRs and their tensile modulus that contradicts earlier studies [23] is reported. The failure mechanisms for the ribbons are investigated and the post buckling progressive failure of chevron-type GNRs are studied using electronic structure methods for the first time. The effect of the nanoribbon structure on their mechanical properties are examined and comparisons between molecular mechanics and electronic structure methods are discussed.

5.2 Methods

Two different methods were chosen for modelling the nanoribbons: the adaptive intermolecular reactive bond order potential (AIREBO) [24] and density functional tight binding third order method (DFTB3) [25]. The AIREBO potential is used as it has become the most commonly applied potential for simulating graphene nanostructures. DFTB3 is employed as it offers a method for calculating the mechanical properties of the structures based on their electronic behaviour. DFTB3 uses a variety of approximations in order to make calculations of large nanostructures computationally affordable but, as shown in chapter 4, it provides performance similar to more costly electronic structure methods.

Several different nanoribbon structures are investigated: armchair, zigzag, chevron-type, cove-type and para-armchair nanoribbons. A range of different widths of armchair and zig-zag ribbons are modelled to investigate possible size effects, whereas the other three types are all based on their experimentally reported structures. The ribbons are simulated using periodic boundary conditions to create an infinitely long ribbon. Tensile strain is applied by deforming the periodic unit cell in the direction of the nanoribbon axis and then allowing the structure to relax to simulate quasi-static tensile strain.

5.2.1 AIREBO simulations

AIREBO [24], as implemented in LAMMPS [26], is used in conjunction with the *fire* damped dynamics energy minimisation routine. The potential is modified by altering the cutoff function range such that the function takes the form of a Heavyside step function. The modified cutoff function switches off interatomic interactions when a pair of atoms are more than 2 Å apart. Periodic boundary conditions are imposed along the nanoribbon axis direction with fixed boundaries in the other two directions. The fixed boundaries are set at a value of 50 Å in order to prevent atoms interacting with them before, during or after tensile failure. The length of the periodic box in the periodic direction was initially allowed to vary to ensure the nanoribbon was fully relaxed. This length is then increased by 0.02 Å and then fixed while an energy minimisation of the atomic coordinates is performed. This process is repeated for 600 steps to try and capture the complete failure of the nanoribbon. The virial stress tensor is computed for the unit cell and used to calculate the effective tensile stress and load on the ribbon. The stress is computed assuming the cross sectional area of the ribbon is equivalent to its width multiplied by the interlaminar distance of graphite, 3.35 Å. This is assumed to be the nanoribbons thickness, an assumption made by other authors which allows for quick comparison between results. The width is assumed to be the distance between the nuclei of carbon atoms on opposite edges.

5.2.2 DFTB simulations

Density functional tight binding with third order corrections (DFTB3) [25] is used as implemented in the DFTB+ package [27]. The third order corrected variant of DFTB is used as it has been shown to provide accurate dissociation behaviour compared to other DFTB variants (see chapter 4). Shell resolved electron spin is included in the simulations, using parameters provided in the DFTB+ manual, but all the nanoribbons start as closed-shell structures except the zig-zag ribbons. These are modelled as diradicals with unpaired electrons occuring in edge-localised orbitals with anti-parallel spins. A periodic calculation is performed with a unit cell containing vacuum gaps such that the simulation area had a cross-section of 200×200 Å perpendicular to the ribbon axis to prevent interaction between ribbons in neighbouring cells. A Monkhorst-Pack grid of $4 \times 1 \times 1$ k-points was chosen through a conversion procedure. An initial relaxation was performed in which the perpendicular lattice dimensions were constrained to maintain the vacuum gaps. This step was used to generate the zero-strain initial state. The length of the unit cell is then increased in steps of 0.02 Å and then constrained while the atomic positions are allowed to relax. This process is then repeated for 600 steps or until the ribbon has fragmented. This is effectively the same method as in the AIREBO calculations.

5.2.3 Mechanical properties

The purpose of the simulations is to determine the structure's strength, strain at failure, Young's modulus and examine its failure mechanisms. In this work the strain is calculated using

$$\varepsilon_{xx} = \frac{\Delta L_{xx}}{L_{xx}}, \tag{5.1}$$

where ε_{xx} is the engineering strain in the x-direction due to an applied load in the x-direction and L_{xx} the initial length in the same direction with ΔL the change in the length [28, 3]. Mechanical stress is calculated as

$$\sigma_{xx} = \frac{1}{V_0}\frac{\partial E}{\partial \varepsilon_{xx}}, \tag{5.2}$$

where σ_{xx} is the engineering stress in the x-direction due to an applied load in the x-direction, V_0 the initial volume of the structure and $\partial E/\partial \varepsilon_{xx}$ is the derivative of the energy with respect to the strain. The strength σ^*_{xx} is taken as the peak value of the stress before failure and the strain at failure as the strain at which that peak occurs. The Young's modulus is calculated as

$$Y = \frac{1}{V_0}\left.\frac{\partial^2 E}{\partial \varepsilon_{xx}^2}\right|_{\varepsilon_{xx}=0} \tag{5.3}$$

by taking numerical derivatives of the stress and taking the mean value between $\varepsilon_{xx} = 0$ and $\varepsilon_{xx} = 0.005$. It was seen that the relationship between stress and strain in this region

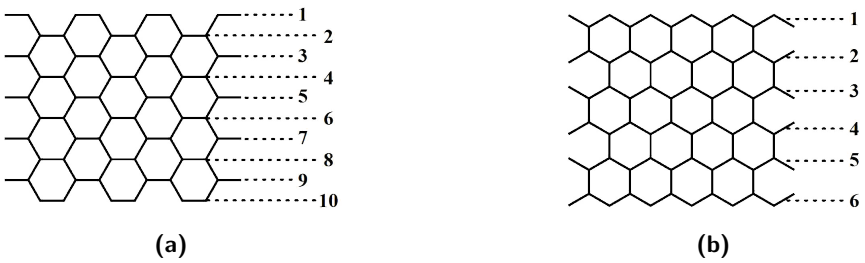

Figure 5.1: The structures of (a) armchair and (b) zig-zag nanonribbons with the bonds used for the indexing system indicated by the dashed lines and numbers. The ribbons shown are AGNR10 and ZGNR6.

was approximately linear. Normally stress, strength and Young's modulus are given in units of pressure and relate the applied load to a cross sectional area of the material. The cross sectional area for the two dimensional lattice of graphene is ill defined as there is no robust method to determine the thickness for the planar material. The thickness used here is the interplanar separation in graphite, $t = 3.35$ Å. This is used by other authors so simplifies comparison of the results presented here and other work. The peak load before failure is also examined for comparison with the results presented in chapter 4.

5.2.4 Nanoribbon structures

Five hydrogen terminated graphene nanoribbon structures are investigated: armchair, zig-zag, chevron-type, cove-type and para-armchair nanoribbons. Armchair and zig-zag nanoribbons are by far the most common nanoribbon forms used in theoretical calculations. These ribbons follow a numbering convention based on how many bonds are present across their width, shown in figure 5.1. The index N allows the structures to be identified using the labels AGNRN and ZGNRN for armchair and zig-zag ribbons respectively. The geometry of the nanoribbons varies with their index as well as their width. Figure 5.2 shows the different geometries of even and odd armchair and zig-zag type nanoribbons. Only a limited subset of these ribbons have been synthesised experimentally [29] but it is possible to investigate all of the possible structures computationally. This offers a systematic way of investigating the effect of increasing ribbon width and index on the mechanical properties of the ribbons. There are several published values for their mechanical properties based on calculations similar to those presented here and these are used for validating the procedures used in this work.

The chevron-type, cove-type and para-armchair structures can be seen in figure 5.3. These structures have all been produced experimentally but there are few or no calculations of their mechanical properties in the literature. From inspection of the shape of the chevron-type and para-armchair ribbons it is reasonable to expect some non-linearity in their force displacement behaviour due to possible out of plane deformation response to tensile loading. The cove-type nanoribbon follows the same chirality as zig-zag nanorib-

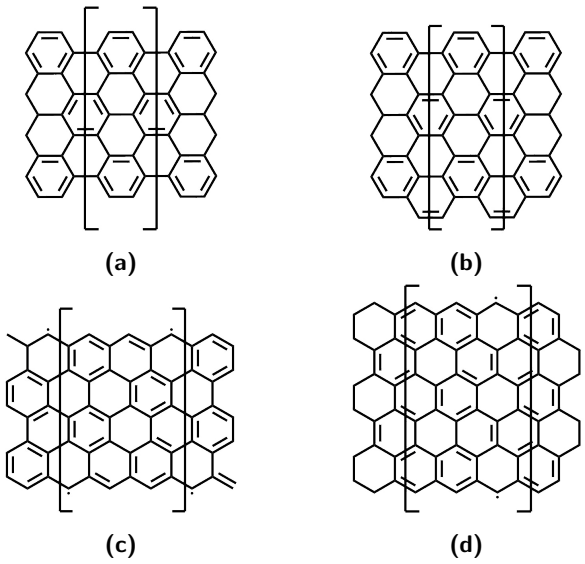

Figure 5.2: The structure of the graphene nanoribbons AGNR9, AGNR10, ZGNR5 and ZGNR6, (a) through (d) respectively, with square brackets enclosing the lengthwise repeat cell.

bons, effectively being a zig-zag ribbon that alternates between a ZGNR4 and ZGNR6 along its length.

5.2.5 Initial tests

DFTB simulations were performed using several structures with varying numbers of repeats of the lengthwise repeat cell to check for for convergence of the calculated quantities. The experimentally derived structures plus one each of even and odd indexed armchair and zig-zag ribbons were passed through the previously described test procedures with the number of repeats of the unit cell varied between one and six. The results were used to determine the size of the periodic cell for the other structures.

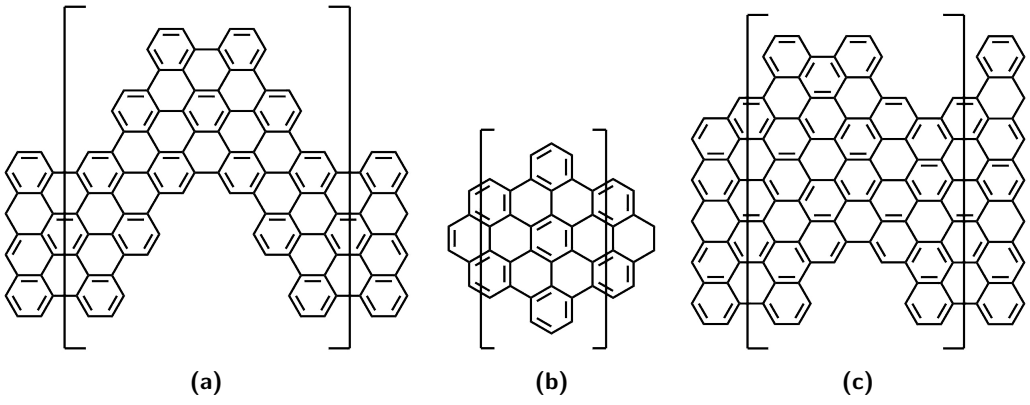

Figure 5.3: The structure of (a) chevron-type, (b) cove-type and (c) para-armchair graphene nanoribbons with the square brackets indicating the lengthwise repeat cell.

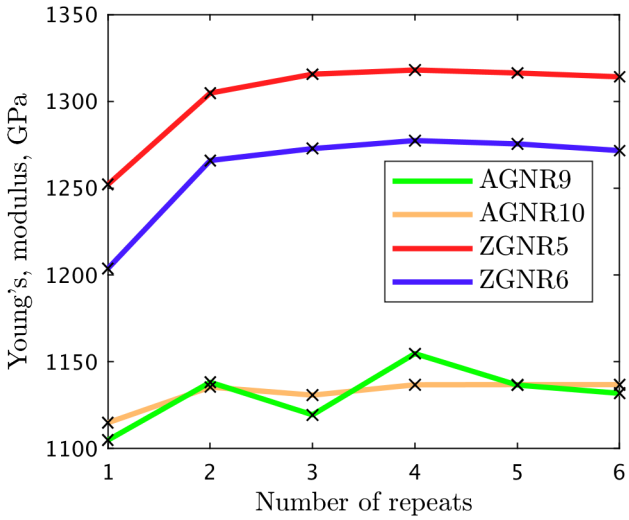

Figure 5.4: Plot of Young's modulus against the number of repeats of the unit cell used in the calculation.

5.3 Results

5.3.1 Initial test results

Several mechanical properties were calculated, Young's Modulus, mechanical strength and strain at failure, for a varying number of repeats of the basic unit cell. These properties are plotted against the number of repeats in figures 5.4 5.5 and 5.6. The plots show only marginal variation in all properties except Young's modulus as the number of repeats of the basic unit cell is increased. The Young's modulus varies by less than 0.5 % after four repeats and so is considered to be converged at this point.

5.3.2 Failure mechanisms

An AGNR9 nanoribbon was used as the test example of odd armchair nanoribbons, an AGNR10 nanoribbon for the even armchair nanoribbons and ZGNR5 and ZGNR6 for zig-zag ribbons. The failure mechanism for the ribbons varied as the number of repeats was increased.

Using a single basic unit cell produces nonphysical failure. For the AGNR9 nanoribbon this involves rings opening and strands of carbon atoms forming as shown in figure 5.7. This mechanism is not what would be intuitively predicted and disappears when a second repeat is added to the periodic cell, as shown in figure 5.8.

The even armchair nanoribbon, AGNR10, also shows different failure mechanisms depending on the number of repeats included in the periodic cell. When only a single repeat is used the structure fails by ring opening and forming chains of carbon atoms as shown if figure 5.9. When larger numbers of basic unit cells are included the failure

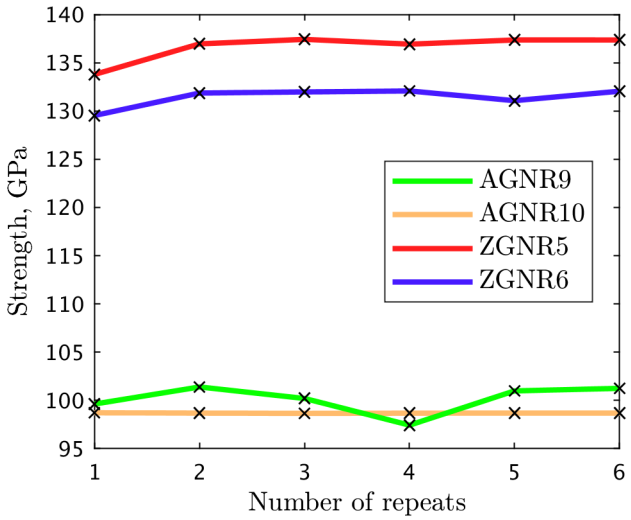

Figure 5.5: Plot of mechanical strength against the number of repeats of the unit cell used in the calculation.

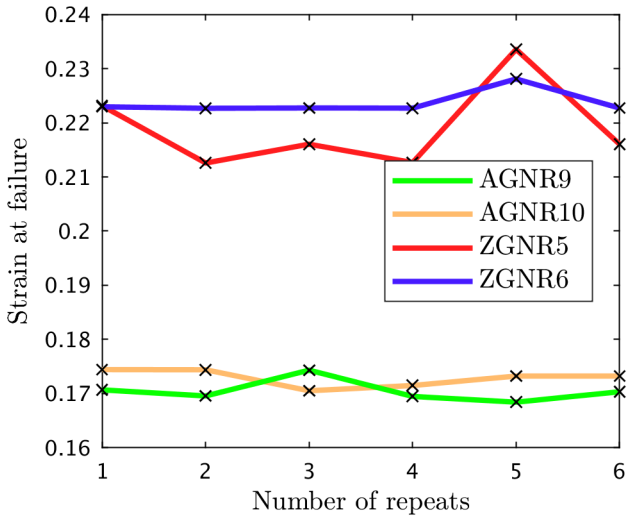

Figure 5.6: Plot of strain at failure against the number of repeats of the unit cell used in the calculation.

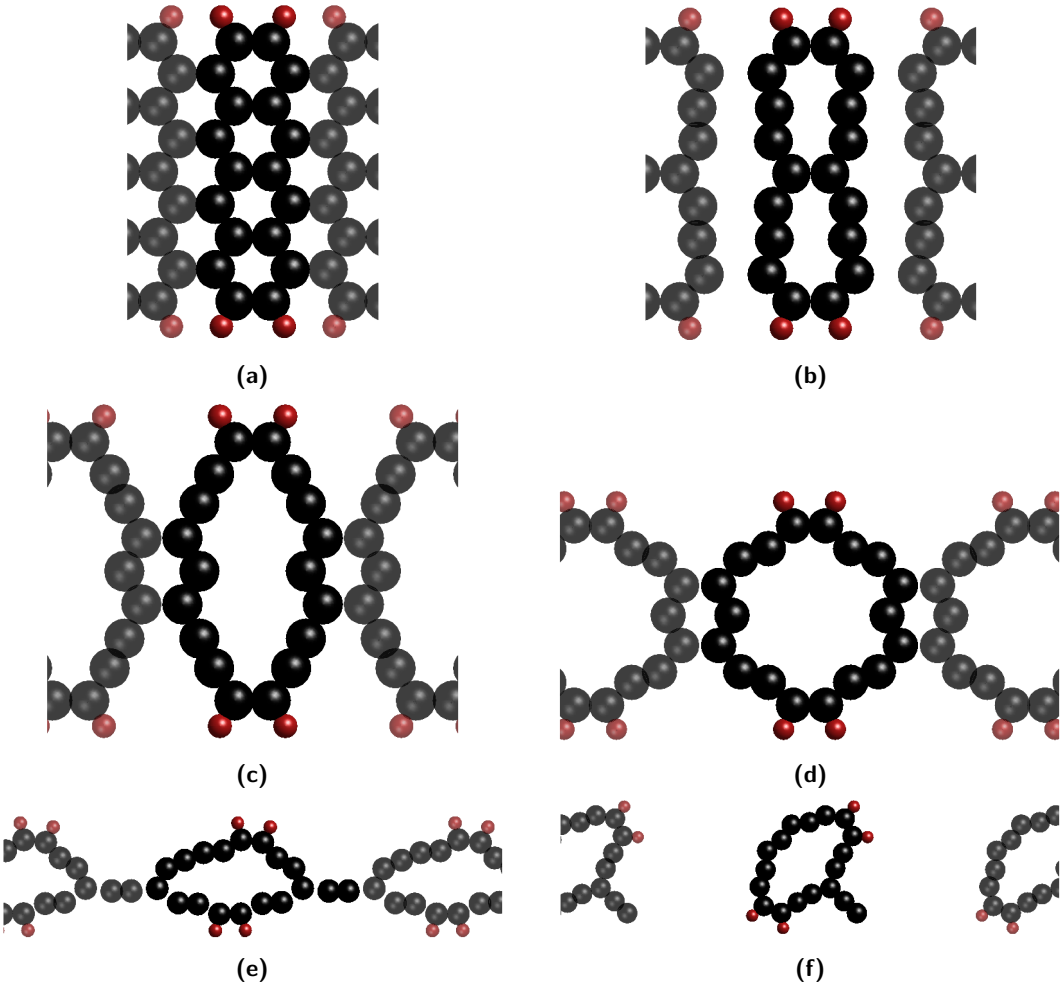

Figure 5.7: Figures (a) through (f) show the failure mechanism when using a single repeat of the basic unit cell of an AGNR9 nanoribbon. The single unit cell is shown with solid colour and its neighbouring images are shown greyed out.

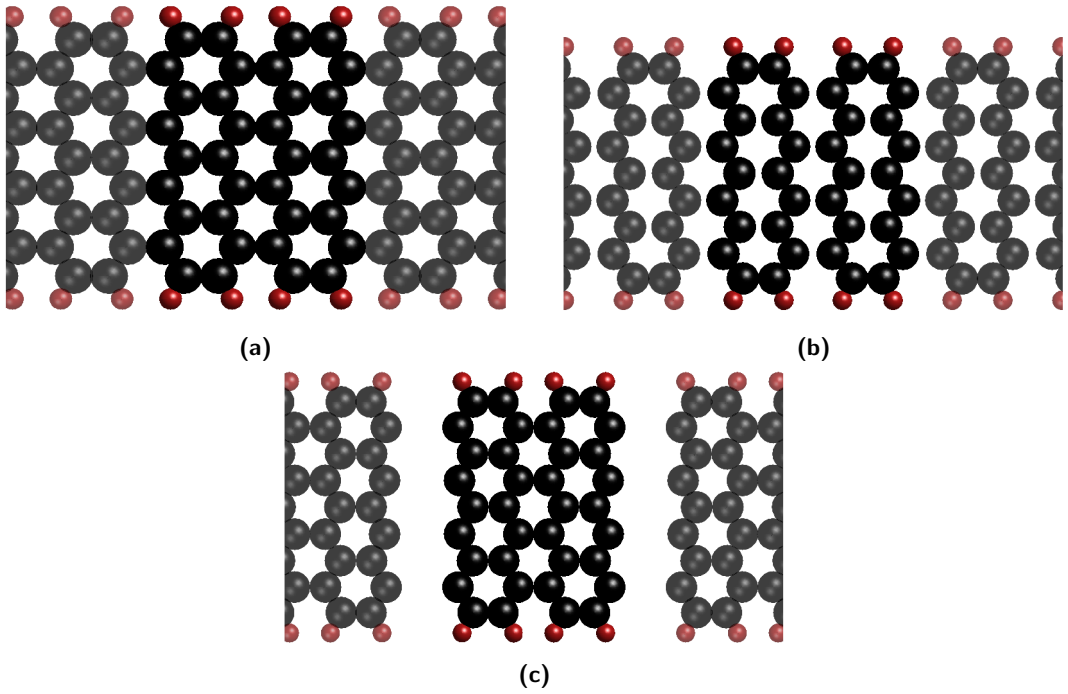

Figure 5.8: Figures (a) through (c) show the failure mechanism when using two repeats of the basic unit cell of an AGNR9 nanoribbon. The single unit cell is shown with solid colour and its neighbouring images are shown greyed out.

mechanism changes to a more intuitive cleavage type failure but the ribbon still shows some ring opening, see figure 5.10.

The failure mechanism for the odd numbered zig-zag ribbon, ZGNR5, was unphysical for periodic cells containing both one and two repeats of the basic unit cell. When failure occurred for the simulation containing a single repeat unit cell the carbon atoms formed chains containing single and triple bonds with hydrogen atoms capping both ends, see figure 5.11. The same mechanism was seen for the ZGNR6 ribbon. Adding a second repeat to the periodic cell altered the failure mechanism but still failed to show the intuitively expected cleavage of the ribbon, see figure 5.12. The primary failure of the ribbon generated sets of 5-7 ring defects followed by pairs of 5-membered rings connected by carbon chains. Similar results were seen when using larger numbers of repeats. Cleavage failure was seen for the ZGNR6 ribbon when using two basic units in the simulation, see figure 5.13. The cause of the failure mechanism for the ZGNR5 ribbon is likely to be its lack of mirror symmetry about the centre of the ribbons width, the terminal hydrogen atoms on either edge are staggered rather than directly opposite each other as for the even numbered zig-zag ribbons.

The variation in mechanical properties and failure mechanisms due to the number of repeats of the basic unit cell appears to be related to the parameters used with DFTB3. A cutoff of 6.88 Å is used for the carbon-carbon interaction parameters so for any pe-

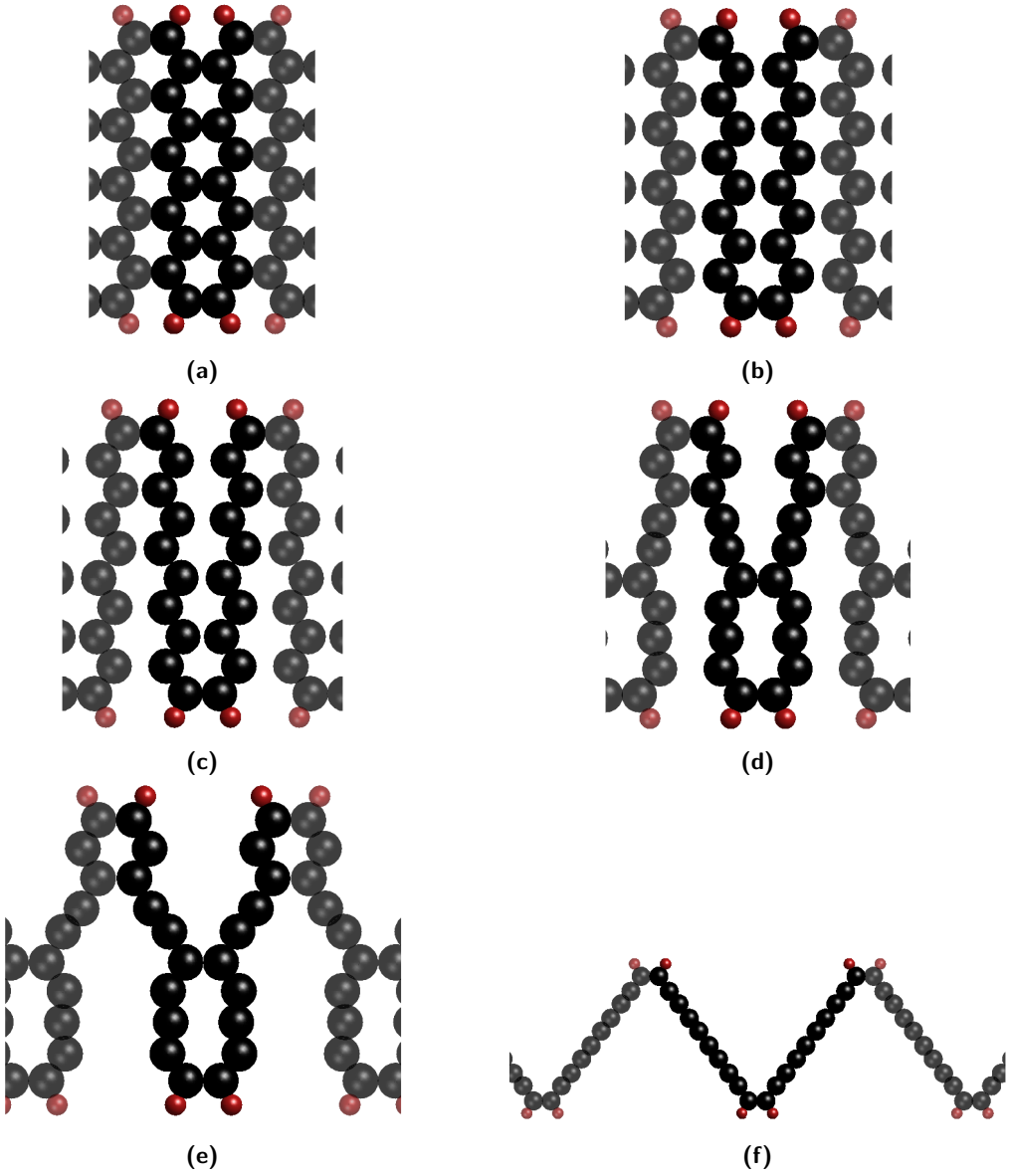

Figure 5.9: Figures (a) through (f) show the failure mechanism when using a single repeat of the basic unit cell of an AGNR10 nanoribbon. At first the ribbon strains with the lack of mirror symmetry causing the carbon-carbon bonds that are aligned with the applied strain to change length by different amounts across the width of the ribbon, figures (a) through (c). The first failure leads to the structure shown in figure (d) which can accommodate the strain by deforming as shown in figure (e). Eventually the rings on either side of the ribbon open up and the ribbon becomes a series of carbon strands as shown in figure (f).

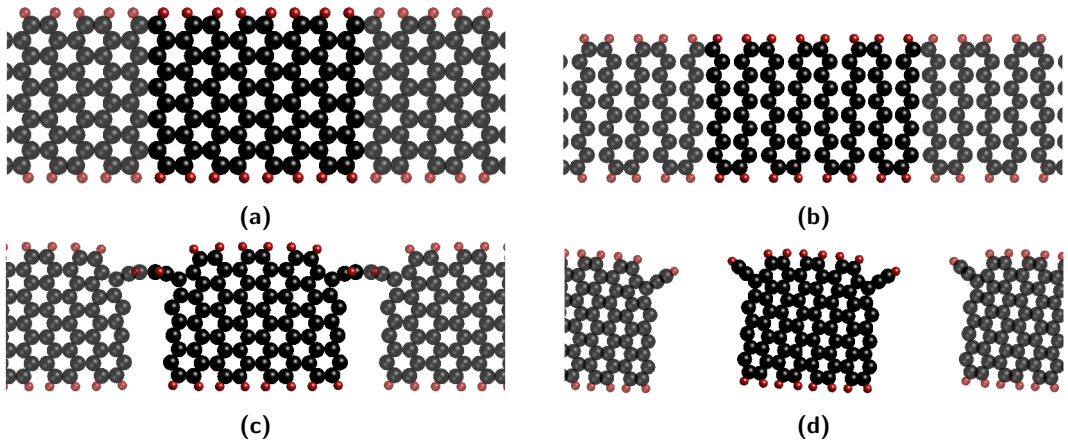

Figure 5.10: Figures (a) through (d) show the failure mechanism when using four repeats of the basic unit cell of an AGNR10 nanoribbon. The ribbon strains in a manner similar to that when using a single repeat, figures (a) and (b). The first failure leads to the structure shown in figure (c) where a pair of 5-membered rings form connected to short chains containing four carbon atoms. The carbon chains eventually fail and the ribbon breaks into individual fragments, figure (d).

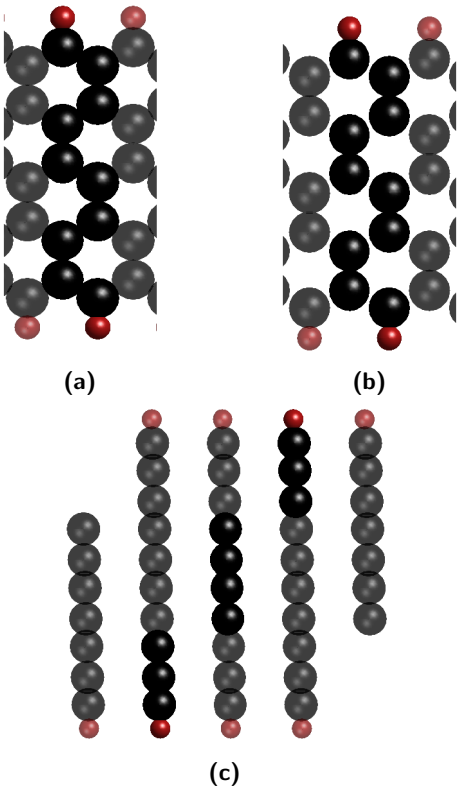

Figure 5.11: Figures (a) through(c) show the failure mechanism when using a single unit cell of a ZGNR5 nanoribbon. The single unit cell is shown with solid colour and its neighbouring images are shown greyed out. The ribbon starts out relaxed (a), then becomes strained (b) and then fails (c) forming chains of carbon atoms consisting of single and triple carbon bonds with hydrogen atoms at each end.

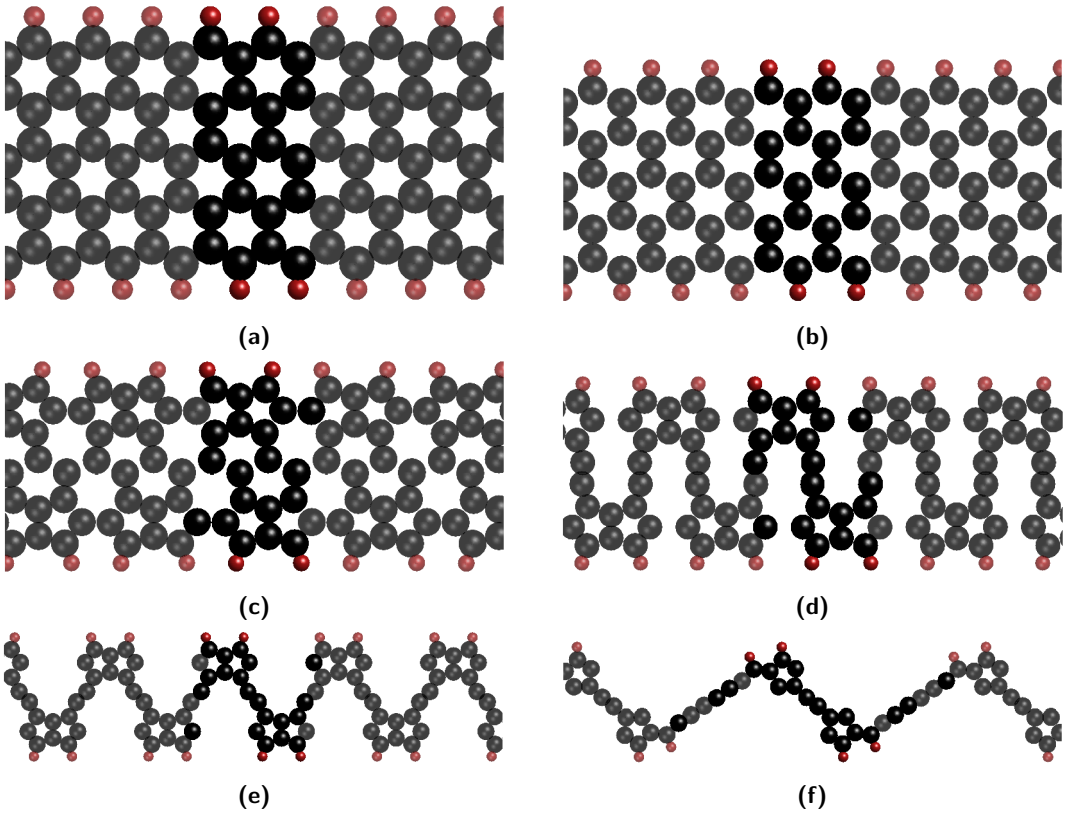

Figure 5.12: Figures (a) through (f) show the failure mechanism when using two repeats of the basic unit cell of a ZGNR5 nanoribbon. The single unit cell is shown with solid colour and its neighbouring images are shown greyed out. The ribbon starts relaxed (a), becomes strained (b), and then fails but producing a sequence of 5-7 defects (c). As the elongation is increased the ribbon forms pairs of 5-membered rings connected by chains of carbon atoms (d), which can rotate to accommodate the applied strain (e). Eventually one of the rings opens with the released carbon atoms combining with the carbon chains (f). Full failure was not observed even when the periodic cell had increased five fold at which point the simulation was stopped.

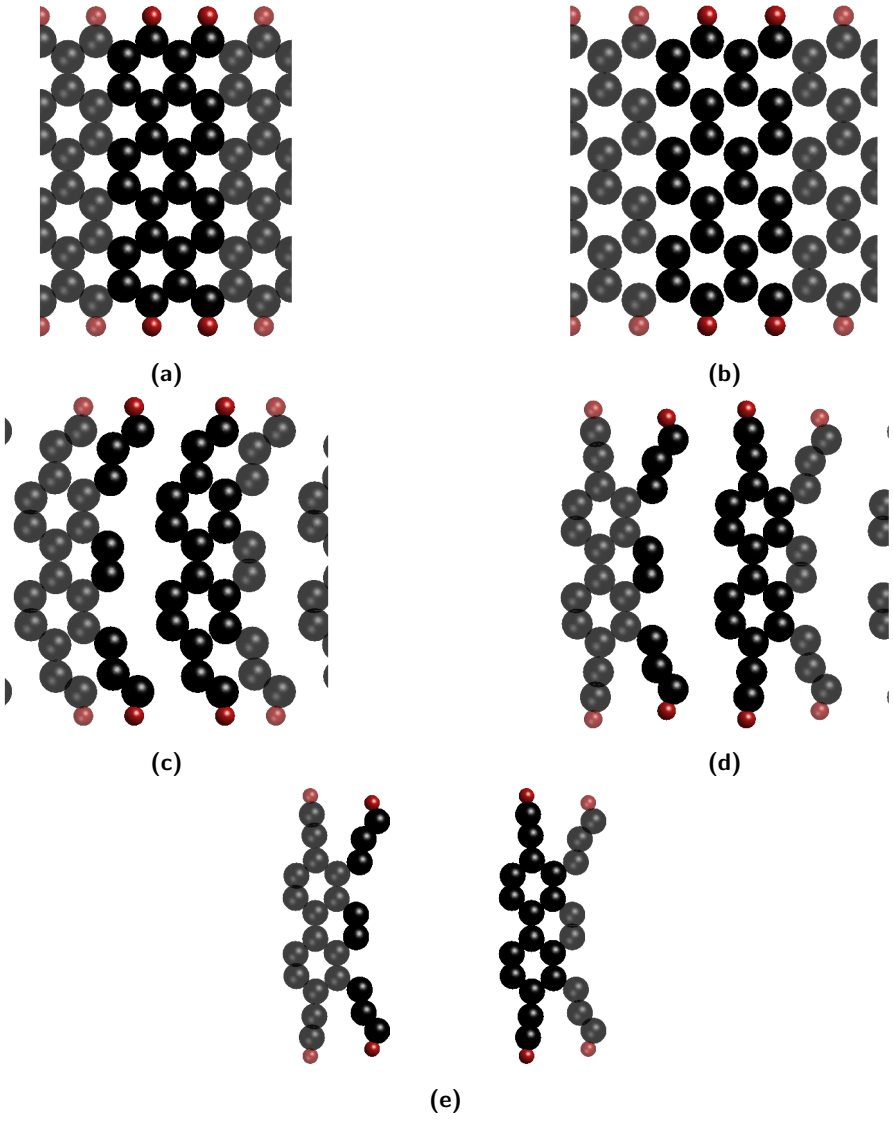

Figure 5.13: Figures (a) through (e) show the failure mechanism when using two repeats of the basic unit cell of a ZGNR6 nanoribbon. The ribbon starts relaxed (a), becomes strained (b), and then fails by cleavage (c) but continues to change shape as the periodic cell length is increased (e).

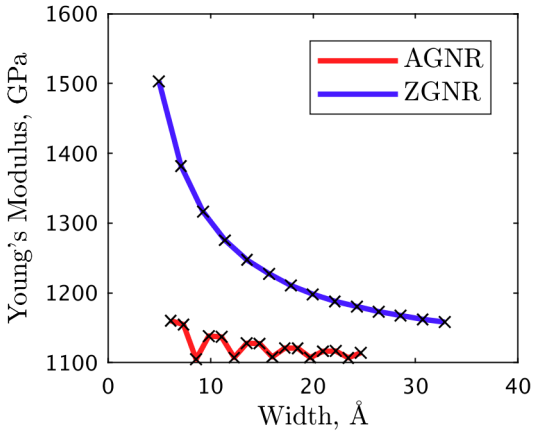

Figure 5.14: The variation of Young's modulus as a function of nanoribbon width for armchair and zig-zag type ribbons.

riodic cell with length less than twice this (13.76 Å) it will be possible for one carbon atom to interact with another carbon atom twice, once inside the cell and once in the nearest image. For periodic cells with length larger than this value the minimum image convention is enforced. The fracture of a solid normally occurs in a single location but in the periodic calculations shown here the failure mechanism produces an infinite number of identically defected crystals. These failure related defects will interact between each periodic cell unless they are sufficiently far apart by using sufficiently large periodic cells. No tests of this type were performed with AIREBO as the cut off parameter for the potential is only 2 Å so the minimum image convention is adequately enforced using the same periodic cells used for the DFTB3 simulations.

5.3.3 Mechanical properties of zig-zag and armchair nanoribbons

With a suitable size of periodic cell determined, a series of DFTB3 calculations were performed using armchair and zig-zag nanoribbons of different widths and the Young's modulus, tensile strength and strain at failure were calculated. These results are shown in figures 5.14, 5.15 and 5.16 The trends for ZGNRs are evident with modulus and strength decreasing as the ribbon width increases and the strain at failure increasing as a function of ribbon width. From continuum mechanics it would be reasonable to assume that these properties should not vary as the ribbon width is increased, but the importance of edge effects on the mechanical properties is well documented [14, 30, 31].

The trends for AGNRs are less well defined; the strength oscillates about a mean value with no obvious periodicity and the strain at failure seems to increase with ribbon width but not all the data points follow this trend. However, it is known that the bandgaps and electronic structures of armchair nanoribbons vary based on the ribbon index N [14]. Armchair nanoribbons can be divided into three families based on whether their index

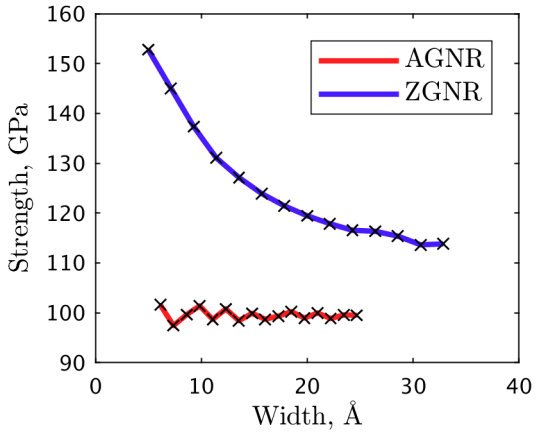

Figure 5.15: The variation of tensile strength as a function of nanoribbon width for armchair and zig-zag type ribbons.

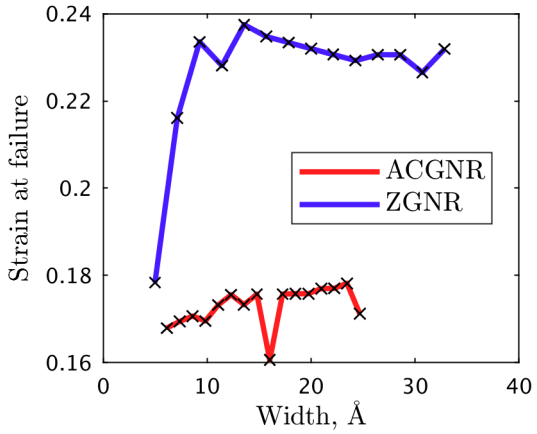

Figure 5.16: The variation of the strain at failure as a function of nanoribbon width for armchair and zig-zag type ribbons.

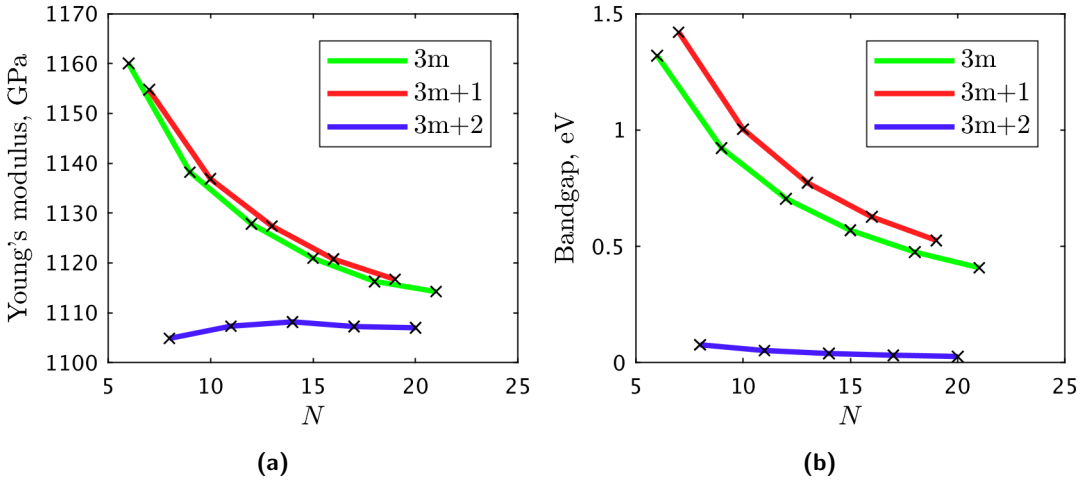

Figure 5.17: Young's modulus (a) and bandgap (b) as a function of N for armchair nanoribbons.

$N = 3m$ or $N = 3m + 1$ or $N = 3m + 2$, where m is an integer. The Young's moduli for the three families are shown graphically in figure 5.17(a). The Young's modulus is highest for the $3m+1$ family, followed by the $3m$ and then the $3m+2$ families. This relationship is similar to that seen for their bandgaps, shown in figure 5.17(b). The three different families also have a different π-orbitals structure from each other, which may explain this behaviour. To examine this a series of simulated scanning tunnelling microscope images are presented in figure 5.18. These have been produced using the Tersoff model of the scanning tunnelling microscope [32]. By applying a small bias voltage between the sample and the scanning tip it is possible to probe only the highest occupied bands of the electronic structure which correspond to the π-orbitals of the ribbons. These images are produced using

$$I(x, y, U) = A \sum_i \rho_i(x, y, d) \left[H(E_\mathrm{F} - E_i) - H\left((Ue + E_\mathrm{F}) - E_i\right) \right], \tag{5.4}$$

where I is the current, $\rho_i(x, y, d)$ the electron density of orbital i at a height d above the plane of the nuclei (assuming they lie on $z = 0$), H the Heaviside step function, U the sample bias, e the atomic unit of charge, E_F the Fermi energy, E_i the energy eigenvalue corresponding to orbital i and A is a constant. The contents of the square bracket ensures the sum only includes contributions from orbitals between the Fermi energy and the Fermi energy plus the bias. These images could be confirmed through experiment but they also provide an intuitive way to depict the π-orbitals. Figure 5.18(a) shows the π-orbitals of the fully benzenoid hydrocarbon structure AGNR21, a member of the $N = 3m$ family. Figures 5.18(b) and 5.18(c) show the π-orbitals for AGNR19 $(3m + 1)$ and AGNR20 $(3m + 2)$ respectively. One effect of the pattern seen in the AGNR19 structure is to restrict the ability of the ribbon to reduce its width. The AGNR20 structure is more

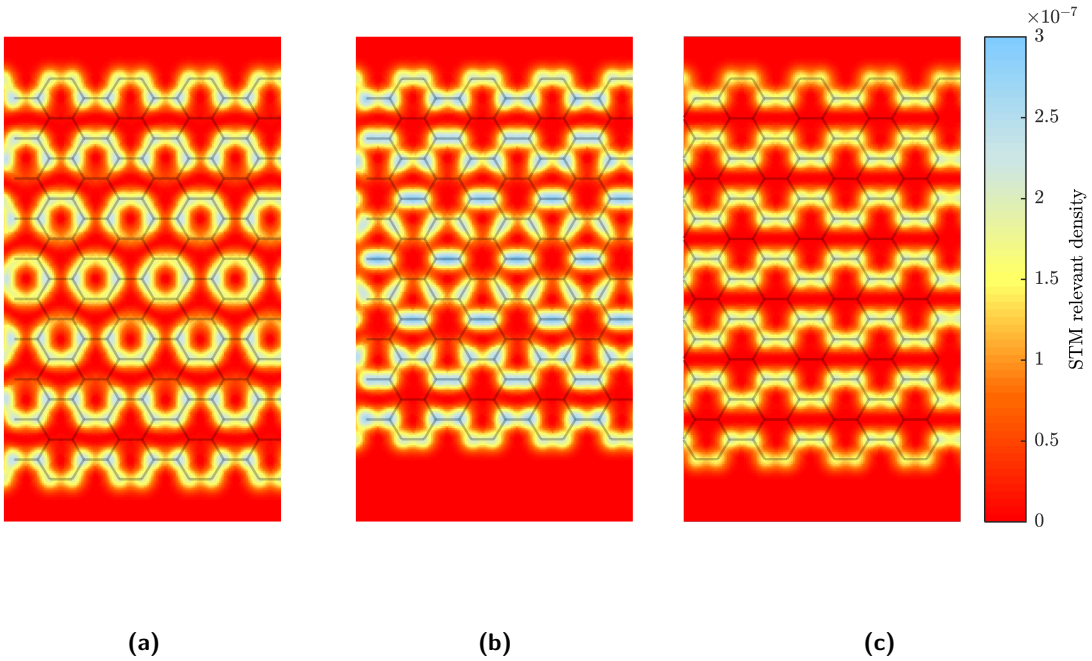

Figure 5.18: Simulated scanning tunnelling microscope images for (a) $3m$, (b) $3m+1$ and (c) $3m+2$ armchair nanoribbons, the ribbons are AGNR21, AGNR19 and AGNR20 respectively. Their molecular structures are indicated by the black lines. These were produced according to the Tersoff-Hamann theory of the scanning tunnelling microscope using a -0.5 V bias and with the tip 2.7 Å above the plane described by the nuclei. The small negative bias ensures tunnelling from the highest energy occupied states, corresponding to the π-orbitals, can occur. In the $3m$ nanoribbon π-orbitals form rings similar to the Clar structure diagrams. The $3m+1$ plot shows the π-orbitals occurring on specific carbon-carbon bonds following patterns similar to Kekulé structures. The $3m+2$ plot shows the π-orbitals aligned with the ribbon axis.

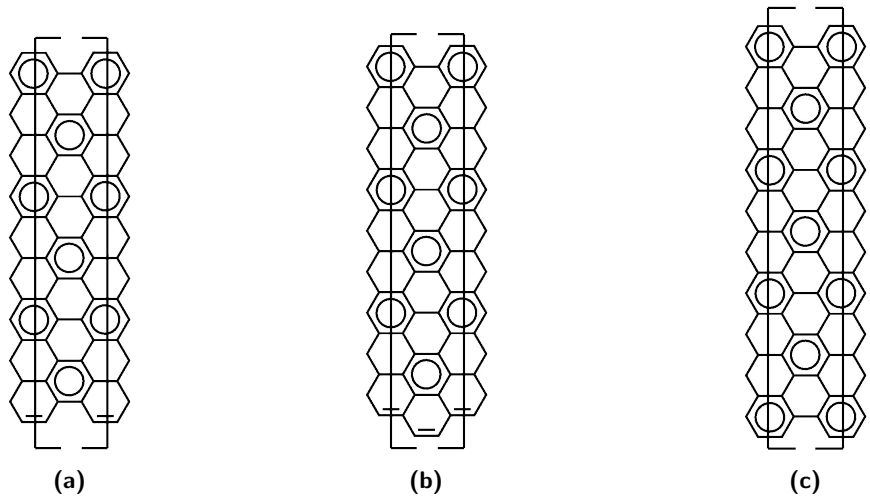

Figure 5.19: The Clar structures for (a) AGNR19, (b) AGNR20 and (c) AGNR21. AGNR21 contains only π-sextet rings or empty rings, AGNR19 contains a lone double bond and AGNR20 contains two double bonds. There is only one allowable Clar structure for AGNR21 but it is possible to draw two for the AGNR19 and many for the AGNR20. There are two Clar structures for the AGNR19 but these reduce under symmetry to a single structure.

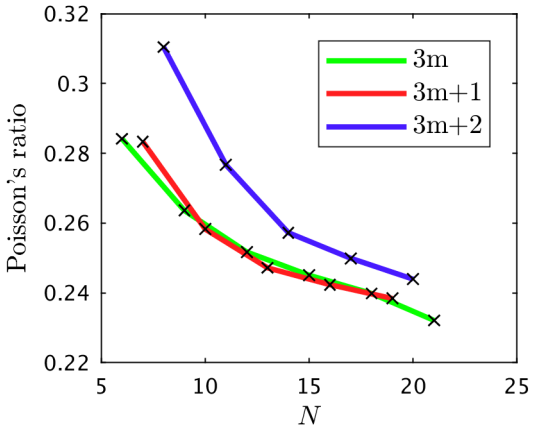

Figure 5.20: Poisson's ratio as a function of ribbon index N for armchair nanoribbons.

able to contract its width in response to tensile loading, i.e. it has a higher Poisson's ratio than the others. The Poisson's ratios for the AGNRs are displayed graphically in figure 5.20. The Clar structures for these three families are shown in figure 5.19.

The results for ribbon strength displayed no obvious trend relating to the ribbon index in either the DFTB3 or AIREBO calculations. The average strength was found to be 99.6 ± 1.1 GPa with DFTB3 compared to 98.4 ± 0.3 GPa with AIREBO. The reason for the sudden dip in the strain at failure curve for AGNRs in figure 5.15 was investigated. Inspection of the stress-strain curve for the ribbon for this data point, AGNR14, indicated the peak at a strain of ≈ 0.16 followed by a gentle negative slope upto a strain of ≈ 0.177 at which point the geometry of the ribbon altered significantly. As there appears to be no discernible reason for this behaviour it is assumed to be due to the simulation method rather than any physical effect.

Figures 5.21 and 5.22 compare the Young's modulus for AGNRs and ZGNRs of this work with those published by other authors. The results by Faccio, Li and Tabarraei [10, 23, 13], were calculated using DFT and those of Bu and Lu [33, 34] were produced using molecular mechanics potentials. The comparable DFT results shown here were produced using periodic boundaries with hydrogen terminated edges. The results from Bu used finite length ribbons modelled in a quasi-static molecular dynamics simulation at 300 K using the Tersoff potential [35]. The work by Lu was conducted using molecular mechanics energy minimisations on a periodic cell using the second generation REBO potential [36]. These three potentials are related as the Tersoff potential was improved by Brenner to make the REBO potentials which were in turn developed by Stuart to produce the AIREBO potential. Comparing the molecular mechanics results for AGNRs indicates just how approximate these methods are and that any trends indicated by their use should be treated with caution. Inspection of figure 5.22 suggests that the potentials are systematically underestimating the carbon-carbon bond stiffness. On the other hand the

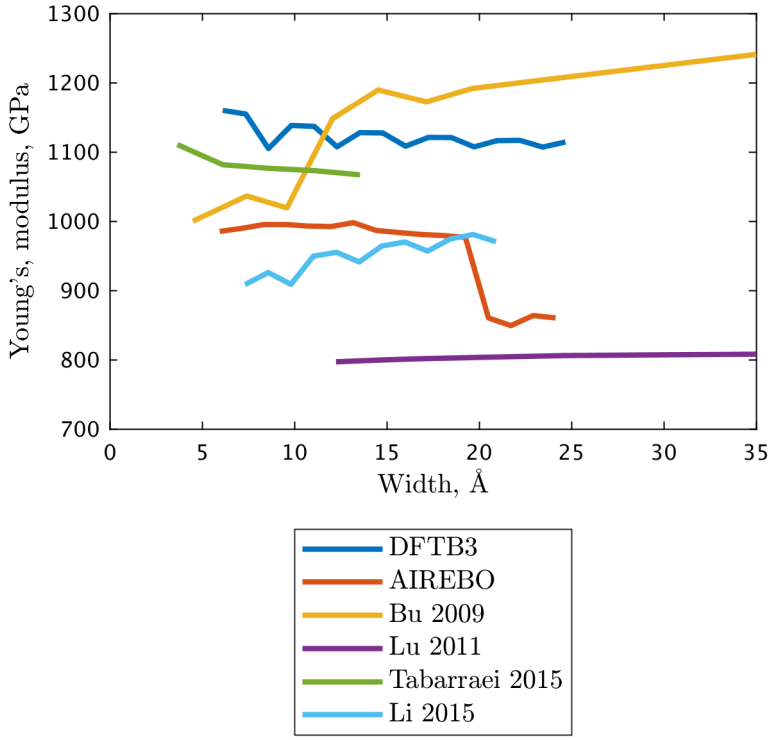

Figure 5.21: Curves for the Young's modulus of AGNRs from this work (DFTB and AIREBO) compared to other authors.

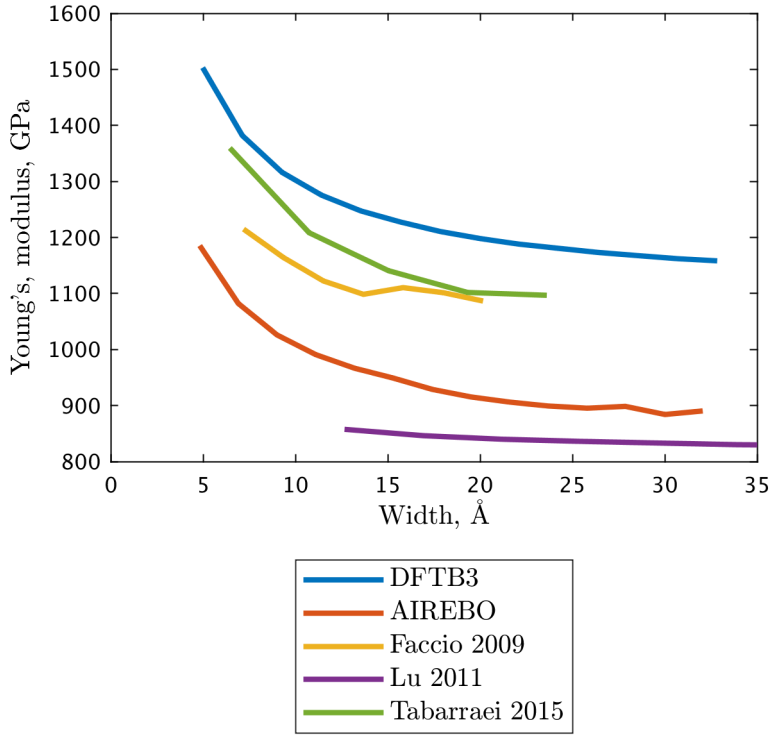

Figure 5.22: Curves for the Young's modulus of ZGNRs from this work (DFTB and AIREBO) compared to other authors.

DFTB3 results seem to overestimate the modulus of the ribbons compared to DFT based calculations. However, there are two important differences between the DFTB3 and the other *ab initio* results for the AGNRs. Firstly, the results of Tabarraei show no oscillation but do show a decrease in modulus as the width is increased. Secondly, although Li's results do show a period three oscillation the general trend is one of increasing modulus with ribbon width. Furthermore, there may be also be an error with Li's width values which appear to be incorrect for the stated AGNR indices. It is highly likely the dips in modulus in their data correspond to the dips shown on the DFTB3 data produced in this work. One possible reason for the increasing trend shown in the Li result is that their simulations considered the modulus as calculated from both compressive and tensile strains at magnitudes of upto 1%. Nanoribbons buckle readily under compressive loading even at strains below 1% [37] and the post-buckling modulus would be lower than the tensile modulus. This argument can be further supported by a separate result, generated using DFT, for AGNR9 that predicts a modulus of 1080 GPa [11], which is notable greater than the $\approx$ 950 GPa generated by Li. However, the calculations performed in this work were conducted under tensile loading only and no investigation of compression or buckling was undertaken.

The predicted failure stresses for ZGNRs calculated using DFTB3 show an obvious inverse relationship to the ribbon width. This is in agreement with results reported by Lu [34] but the relationship shown here is more extreme with thinner ribbons showing a much higher strength in comparison with Lu's results. This large decrease in strength is shown in the results of Tabarraei [13] which indicates a significant difference between the predicted behaviours of the structures when using electronic structure and potential based models. Tabarraei's results also show less variation of tensile strength for AGNRs, as shown here with the DFTB3 result. The DFTB3 strains at failure for AGNRs are similar to those calculated by both Tabarraei and Lu, ≈ 0.17. For ZGNRs the DFTB3 value of ≈ 0.23 is lower than the ≈ 0.24 value from Tabarraei but both of these are signifcantly less than the ≈ 0.29 from Lu.

The most obvious differences between the mechanical properties of armchair and zig-zag nanoribbons are the higher strength and strain at failure of the zig-zag ribbons, see figures 5.15 and 5.16. In zig-zag ribbons the bond angles change to reduce the angle between the bond direction and the direction of the applied load for all bonds except those aligned perpendicular to the ribbon axis, as can be seen in figure 5.13. The non-perpendicular bonds can resist the applied load using two separate deformation mechanisms, first by bond angle deformation and then bond elongation. This allows the ribbon to deform to a greater extent compared with armchair ribbons. By contrast, armchair ribbons resist the tensile load by bond elongation of bonds parallel to the ribbon axis as shown in figures 5.10 and 5.8. For odd numbered armchair ribbons the number of axially aligned bonds varies along the length between $(N + 1)/2$ and $(N - 1)/2$. The applied load must be transmitted through the narrower section, which means they will deform to a greater

extent and fail before the axially aligned bonds in the wider section. Zig-zag ribbons of similar width have an index equal to the $(N + 1)/2$ section and will possess the same number of bonds but they will be aligned at 30° to the ribbon axis. For example, in the AGNR9 ribbon (see figure 5.8) the number of bonds alternates between four and five, as we move along its length, compared to the ZGNR5 ribbon (see figure 5.12) which has five bonds across its width. These ribbons have similar widths, 9.83 Å for the AGNR9 and 9.26 Å for ZGNR5 yet the zig-zag ribbon is stronger and has a higher strain at failure. The even numbered armchair ribbons are generally weaker than odd numbered armchair ribbons due to their lack of mirror symmetry about the ribbon axis. This produces an uneven distribution of the load across the width of the ribbon, as can be seen in figure 5.10, with bonds at the edges carrying more load than others. Thus the higher strength and stiffness of the zig-zag ribbons is due to the presence of an additional bond compared to odd numbered armchair ribbons of similar width. As the width is increased the negative factors affecting the armchair ribbons have less impact so it is expected that the Young's modulus and tensile strength will converge towards the values for bulk graphene. However, the strain at failure for the zig-zag ribbons will always be greater than armchair ribbons due to the differences in the deformation mechanisms.

5.3.4 Mechancical properties of experimentally derived nanoribbon structures

The three experimentally derived graphene nanoribbon structures present a variety of mechanical properties and failure mechanisms. Force-strain curves for the ribbons are shown in figure 5.23. The calculation of the Young's modulus and strength are complicated by the problem of the varying widths of the nanoribbons leading to a varying cross-sectional area. Figure 5.23 indicates that the cove-type ribbon has the greatest strain at failure and that it fragments in a single event. This is not the case for the other ribbons which undergo multiple bond scission events before fragmentation and each event causes significant changes to their structures. The chevron-type ribbon has a particular interesting failure mechanism due to the occurrence out-of-plane buckling as the ribbon is stretched. The tension in the ribbon is plotted simultaneously with the bond length of the first carbon-carbon bond which undergoes scission in figure 5.24. The ribbon remains planar until just after the peak in the force-displacement curve and then it buckles producing a discontinuity in the force-strain curve. The bond closest to the ribbon edge at the inside of the corner of the ribbon is significantly strained at this point and shows a bond length greater than the predicted peak restorative force determined from the Clar's goblet structure discussed in chapter 4. Although the bond is strained beyond this point it continues to provide some counter acting force against the applied load upto a strain of 0.191. If the applied load is removed before this strain value then the structure should recover its original form. The stiffness of the ribbon is proportional to the gradient of

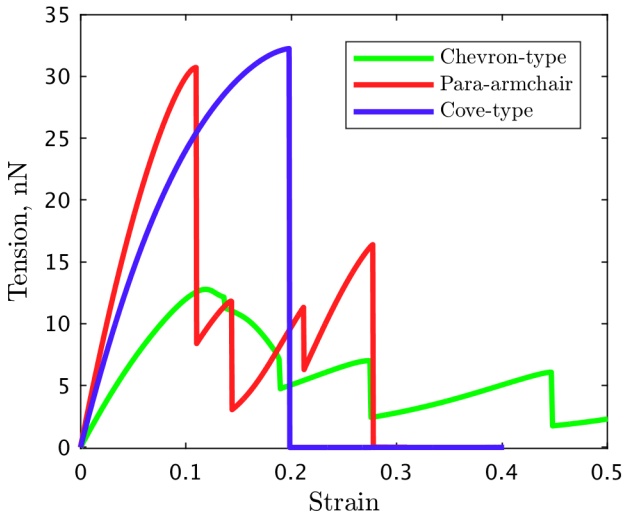

Figure 5.23: The stress-strain curves for the three experimentally derived nanoribbons. The cove-type shows the highest tensile strength followed by the para-armchair and then the chevron-type nanoribbon. The cove-type ribbon undergoes a catastrophic failure at a strain of ≈ 0.2 whereas the para- and chevron-type ribbons fail in a progressive manner with individual bonds breaking one by one causing the structures to change shape.

Table 5.1: Peaks in tension of the ribbon and the strain values at which they occur.

Structure	Peak tension (nN)	strain at failure
Cove-type	32.25	0.198
ZGNR3	24.40	0.177
ZGNR4	34.55	0.205
ZGNR5	42.65	0.216
Para-type	30.72	0.109
Chevron-type	12.78	0.119
AGNR9	33.38	0.170
AGNR15	57.41	0.176

the curve in figure 5.23 so before failure the stiffness will pass through zero and become negative. The behaviour of the ribbon is unlike most macroscopic structures in that the post-buckling behaviour is still entirely elastic: the deformation will be fully reversed once the ribbon is unloaded. This complex failure mechanism is not seen in the para-armchair nanoribbon even though its wiggling structure has some similarities to the chevron-type nanoribbon

The peak forces and strain at failure values are shown in table 5.1 alongside values for a selection of zig-zag and armchair ribbons. The cove-type ribbon can be thought of as an augmented ZGNR4 nanoribbon, see figure 5.25(a), and, similarly, the para-type ribbon as an augmented AGNR9 ribbon, see figure 5.25(b). Comparison of the values for ZGNR4 and the cove-type ribbons indicates that the cove-type is weaker than the comparable zig-zag ribbon and the same is found for the para-type and AGNR9

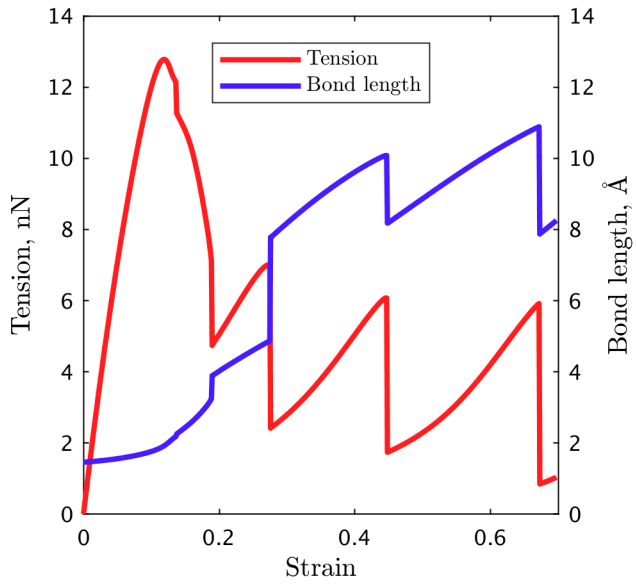

Figure 5.24: The tension in the ribbon (red) and bond length of the most stretched bond (blue) as a function of the strain in the nanoribbon. The peak in the tension corresponds to the peak restorative force for the bonds undergoing the greatest strain. Beyond that point the tension decreases and the ribbon extends finding new lower energy conformations in a step-like manner caused by the breaking of other bonds.

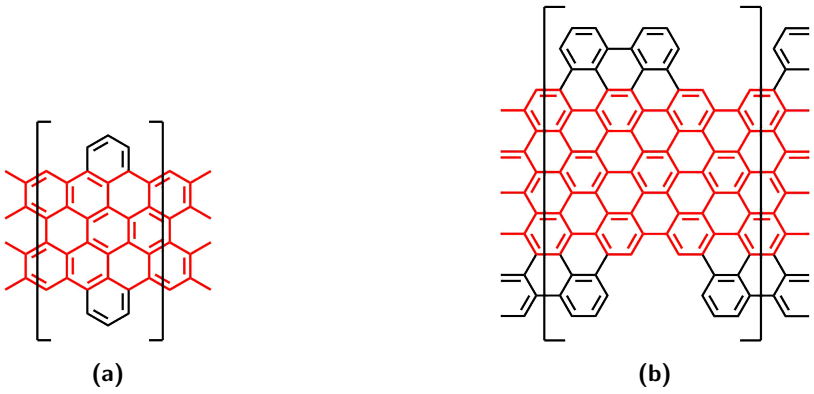

Figure 5.25: The structures of (a) para-armchair and (b) cove-type nanoribbons with the structures of ZGNR4 and AGNR9 highlighted in red.

ribbons. The difference in the strain at failure values between the standard ribbons and their augmented experimentally derived counterparts shows more variation than the peak tension values. The para-type ribbon fails at a much lower strain than the AGNR9 ribbon whereas the cove-type ribbon fractures at only slightly less strain than ZGNR4. The reasons for this have not been investigated here but it appears likely to be to do with size of the augmentations or whether the augmented structures possess mirror symmetry across the ribbon axis.

The experimentally derived nanoribbon structures show a variety of different behaviour compared with the conventional armchair and zig-zag nanoribbons. The structure of the chevron-types nanoribbon is similar to an AGNR15 ribbon but with sections cut away from the top and bottom edges in an alternating manner but at its narrowest section it is similar to an AGNR9 ribbon. Like both of these ribbons, which belong to the $N = 3m$ family, it has a fully benzenoid electronic structure as do the cove-type and para-armchair ribbons. The characteristic conjugated π-orbitals that are present in the $N = 3m$ armchair ribbons (figure 5.18(a)) can also be seen in the experimentally derived ribbons, see figure 5.26). The electronic structure of the cove-type ribbon is fundamentally different to those of the zig-zag nanoribbon family. Zig-zag nanoribbons are not fully benzenoid (see figures 5.2(c) 5.2(d)) and contain unpaired electrons whereas the cove-type does not.

5.4 Conclusions

This work has investigated the tensile mechanical properties of a variety of graphene nanoribbons. Initial tests to determine the effect of the size of the simulation cell were performed. The relationship between the π-orbitals of the ribbons and the tensile properties was investigated and the results compared.

Armchair nanoribbons were shown to possess three different orbital structures depending on their index. The impact of this on their moduli has been examined and explained. Armchair ribbons with the lowest bandgap, the $N = 3m + 2$ family, were found to have the lowest tensile stiffness and the greatest Poisson's ratio. This was explained by their π-orbitals occurring on bonds aligned parallel to the ribbon axis. The $N = 3m+1$ family of armchair ribbons was shown to have the highest stiffness and lowest Poisson's ratio due to their π-orbital structure. The fully benzenoid $N = 3m$ family was shown to posses π-orbital aromatic rings which resulted in mechanical properties similar to those seen in the $N = 3m + 1$ family. Zig-zag GNRs were shown to have higher modulus, strength and strain at failure than AGNRs which suggest they may be better for use as polymer reinforcement particles for nanocomposites. However, fewer types of ZGNR have been synthesised than AGNRs so it may be better to consider structures such as the cove-type GNR.

This work has shown that cove-type GNRs can carry loads of similar magnitude compared

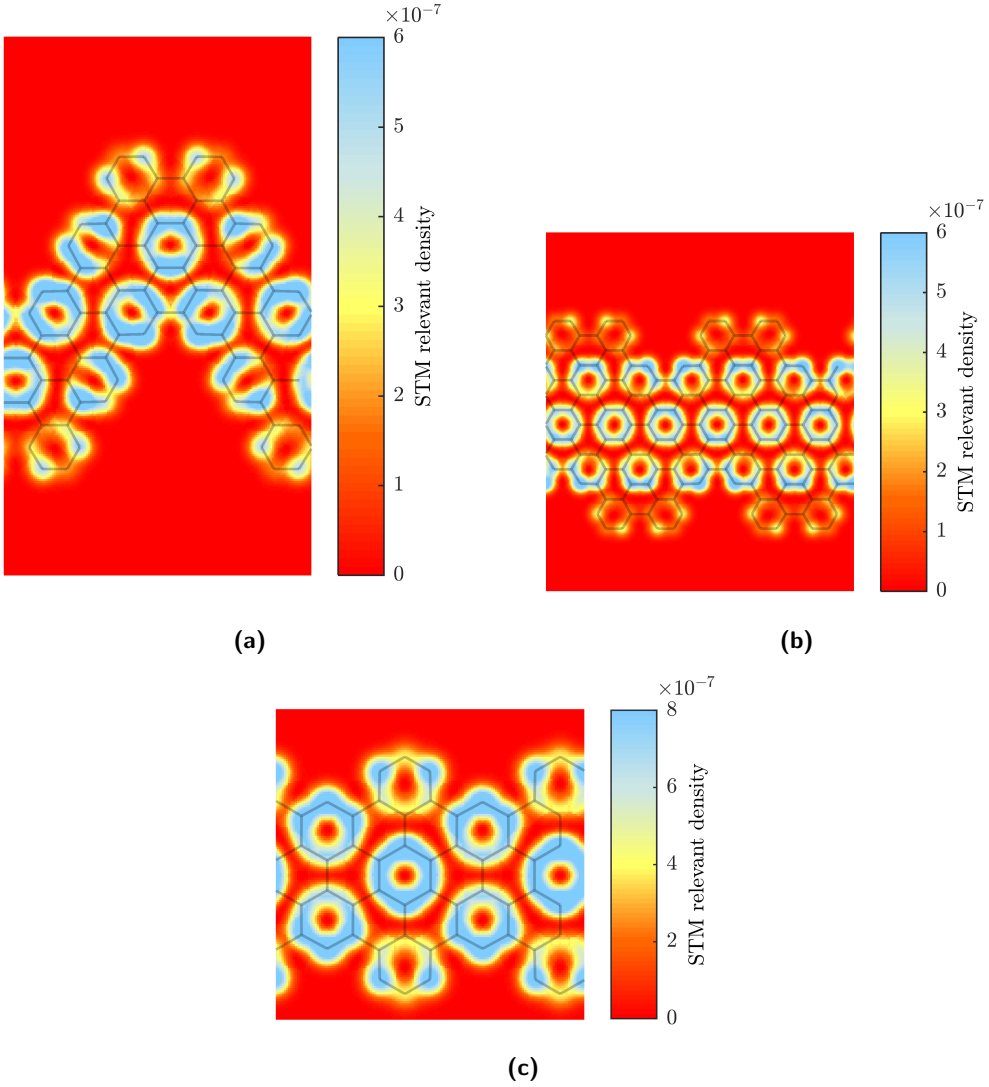

Figure 5.26: Simulated STM images for (a) chevron-type, (b) para-armchair and (c) cove-type nanoribbons created using a STM tip height of 2.7 Å above the ribbon surface with tip bias of −1.0 V for the chevron-type and −.75 V for the para-armchair and cove-type nanoribbons. The conjugated π-orbitals are shown as blue rings similar to those seen in figure 5.18(a).

to geometrically similar ZGNRs and have a comparable strain at failure. Para-type and chevron-type GNRs were shown to have worse mechanical properties than comparable AGNRs but chevron-type GNRs were shown to possess a non-linear response to applied loads and a progressive failure mechanism. All the experimentally derived GNRs were shown to possess a benzenoid structure containing aromatic rings.
The work presented here gives some insight into the mechanical behaviour of nanoribbon structures. It should help in the design of both future nanoribbon structures as well as guiding the selection of nanoribbons for use in nanocomposites.

Bibliography

[1] Z. Liao, L. M. Sandonas, T. Zhang, M. Gall, A. Dianat, R. Gutierrez, U. Mühle, J. Gluch, R. Jordan, G. Cuniberti, and E. Zschech. In-situ stretching patterned graphene nanoribbons in the transmission electron microscope. *Scientific Reports*, 7(1):1–7, 2017.

[2] L. Pastewka, P. Pou, R. Pérez, P. Gumbsch, and M. Moseler. Describing bond-breaking processes by reactive potentials: Importance of an environment-dependent interaction range. *Physical Review B - Condensed Matter and Materials Physics*, 78(16):78–81, 2008.

[3] H. Zhao, K. Min, and N. R. Aluru. Size and Chirality Dependent Elastic Properties of Graphene Nanoribbons under Uniaxial Tension. *Nano Letters*, 9(8):3012–3015, 2009.

[4] H. Zhao and N. R. Aluru. Temperature and strain-rate dependent fracture strength of graphene. *Journal of Applied Physics*, 108(6):064321, 2010.

[5] Q. Lu, W. Gao, and R. Huang. Atomistic simulation and continuum modeling of graphene nanoribbons under uniaxial tension. *Modelling and Simulation in Materials Science and Engineering*, 19(5):054006, 2011.

[6] P. Zhang, L. Ma, F. Fan, Z. Zeng, C. Peng, P. E. Loya, Z. Liu, Y. Gong, J. Zhang, X. Zhang, P. M. Ajayan, T. Zhu, and J. Lou. Fracture toughness of graphene. *Nature communications*, 5:3782, 2014.

[7] E. Zaminpayma and P. Nayebi. Mechanical and electrical properties of functionalized graphene nanoribbon: A study of reactive molecular dynamic simulation and density functional tight-binding theory. *Physica B: Condensed Matter*, 459:29–35, 2015.

[8] R. Bizao, T. Botari, E. Perim, N. Pugno, and D. Galvao. Mechanical properties and fracture patterns of graphene (graphitic) nanowiggles. *Carbon*, 119:431–437, 2017.

[9] J.-H. Lee, P. E. Loya, J. Lou, and E. L. Thomas. Dynamic mechanical behavior of multilayer graphene via supersonic projectile penetration. *Science*, 346(6213):1092–1096, 2014.

[10] R. Faccio, P. A. Denis, H. Pardo, C. Goyenola, and Á. W. Mombrú. Mechanical properties of graphene nanoribbons. *Journal of Physics: Condensed Matter*, 21(28):285304, 2009.

[11] L. Liang and V. Meunier. Electronic and thermoelectric properties of assembled graphene nanoribbons with elastic strain and structural dislocation. *Applied Physics Letters*, 102(14), 2013.

[12] R. Khare, S. L. Mielke, J. T. Paci, S. Zhang, R. Ballarini, G. C. Schatz, and T. Belytschko. Coupled quantum mechanical/molecular mechanical modeling of the fracture of defective carbon nanotubes and graphene sheets. *Physical Review B - Condensed Matter and Materials Physics*, 75(7):1–12, 2007.

[13] A. Tabarraei, S. Shadalou, and J. H. Song. Mechanical properties of graphene nanoribbons with disordered edges. *Computational Materials Science*, 96(PA):10–19, 2015.

[14] K. Nakada, M. Fujita, G. Dresselhaus, and M. S. Dresselhaus. Edge state in graphene ribbons: Nanometer size effect and edge shape dependence. *Physical Review B*, 54(24):17954–17961, 1996.

[15] C. Stampfer, J. Güttinger, S. Hellmüller, F. Molitor, K. Ensslin, and T. Ihn. Energy Gaps in Etched Graphene Nanoribbons. *Physical Review Letters*, 102(5):056403, 2009.

[16] F. Molitor, A. Jacobsen, C. Stampfer, J. Güttinger, T. Ihn, and K. Ensslin. Transport gap in side-gated graphene constrictions. *Physical Review B*, 79(7):075426, 2009.

[17] M. Y. Han, J. C. Brant, and P. Kim. Electron Transport in Disordered Graphene Nanoribbons. *Physical Review Letters*, 104(5):056801, 2010.

[18] G. Liu, Y. Wu, Y.-M. Lin, D. B. Farmer, J. A. Ott, J. Bruley, A. Grill, P. Avouris, D. Pfeiffer, A. A. Balandin, and C. Dimitrakopoulos. Epitaxial Graphene Nanoribbon Array Fabrication Using BCP-Assisted Nanolithography. *ACS Nano*, 6(8):6786–6792, 2012.

[19] J. Cai, P. Ruffieux, R. Jaafar, M. Bieri, T. Braun, S. Blankenburg, M. Muoth, A. P. Seitsonen, M. Saleh, X. Feng, K. Müllen, and R. Fasel. Atomically precise bottom-up fabrication of graphene nanoribbons. *Nature*, 466(7305):470–473, 2010.

[20] P. Ruffieux, S. Wang, B. Yang, C. Sánchez-Sánchez, J. Liu, T. Dienel, L. Talirz, P. Shinde, C. A. Pignedoli, D. Passerone, T. Dumslaff, X. Feng, K. Müllen, and R. Fasel. On-surface synthesis of graphene nanoribbons with zigzag edge topology. *Nature*, 531(7595):489–492, 2016.

[21] A. Narita, X. Feng, Y. Hernandez, S. A. Jensen, M. Bonn, H. Yang, I. A. Verzhbitskiy, C. Casiraghi, M. R. Hansen, A. H. R. Koch, G. Fytas, O. Ivasenko, B. Li, K. S. Mali, T. Balandina, S. Mahesh, S. De Feyter, and K. Müllen. Synthesis of structurally well-defined and liquid-phase-processable graphene nanoribbons. *Nature Chemistry*, 6(2):126–132, 2014.

[22] Y. Huang, Y. Mai, U. Beser, J. Teyssandier, G. Velpula, H. Van Gorp, L. A. Straasø, M. R. Hansen, D. Rizzo, C. Casiraghi, R. Yang, G. Zhang, D. Wu, F. Zhang, D. Yan, S. De Feyter, K. Müllen, and X. Feng. Poly(ethylene oxide) Functionalized Graphene Nanoribbons with Excellent Solution Processability. *Journal of the American Chemical Society*, 138(32):10136–10139, 2016.

[23] X. Li, T.-Y. Zhang, and Y. J. Su. Periodically Modulated Size-Dependent Elastic Properties of Armchair Graphene Nanoribbons. *Nano Letters*, 15(8):4883–4888, 2015.

[24] S. J. Stuart, A. B. Tutein, and J. A. Harrison. A reactive potential for hydrocarbons with intermolecular interactions. *The Journal of Chemical Physics*, 112(2000):6472–6486, 2000.

[25] Y. Yang, H. Yu, D. York, Q. Cui, and M. Elstner. Extension of the self-consistent-charge density-functional tight-binding method: Third-order expansion of the density functional theory total energy and introduction of a modified effective coulomb interaction. *Journal of Physical Chemistry A*, 111(42):10861–10873, 2007.

[26] S. Plimpton. Fast Parallel Algorithms for Short-Range Molecular Dynamics. *Journal of Computational Physics*, 117(1):1–19, 1995.

[27] B. Aradi, B. Hourahine, and T. Frauenheim. DFTB+, a sparse matrix-based implementation of the DFTB method. *Journal of Physical Chemistry A*, 111(26):5678–5684, 2007.

[28] R. Turton. *The Physics of Solids*. Oxford University Press, 2000.

[29] L. Talirz, P. Ruffieux, and R. Fasel. On-Surface Synthesis of Atomically Precise Graphene Nanoribbons. *Advanced Materials*, pages 6222–6231, 2016.

[30] L. Yang, C.-H. Park, Y.-W. Son, M. L. Cohen, and S. G. Louie. Quasiparticle Energies and Band Gaps in Graphene Nanoribbons. *Physical Review Letters*, 99(18):186801, 2007.

[31] S. M.-M. Dubois, Z. Zanolli, X. Declerck, and J.-C. Charlier. Electronic properties and quantum transport in Graphene-based nanostructures. *The European Physical Journal B*, 72(1):1–24, 2009.

[32] J. Tersoff and D. R. Hamann. Theory of the scanning tunneling microscope. *Physical Review B*, 31(2):805–813, 1985.

[33] H. Bu, Y. Chen, M. Zou, H. Yi, K. Bi, and Z. Ni. Atomistic simulations of mechanical properties of graphene nanoribbons. *Physics Letters, Section A: General, Atomic and Solid State Physics*, 373(37):3359–3362, 2009.

[34] Q. Lu, W. Gao, and R. Huang. Atomistic simulation and continuum modeling of graphene nanoribbons under uniaxial tension. *Modelling and Simulation in Materials Science and Engineering*, 19(5):054006, 2011.

[35] J. Tersoff. New empirical approach for the structure and energy of covalent systems. *Physical Review B*, 37(12):6991–7000, 1988.

[36] D. W. Brenner, O. a. Shenderova, J. a. Harrison, S. J. Stuart, B. Ni, and S. B. Sinnott. A second-generation reactive empirical bond order (REBO) potential energy expression for hydrocarbons. *Journal of Physics: Condensed Matter*, 14(4):783–802, 2002.

[37] Y. Gao and P. Hao. Mechanical properties of monolayer graphene under tensile and compressive loading. *Physica E: Low-Dimensional Systems and Nanostructures*, 41(8):1561–1566, 2009.

Chapter 6

Conclusions and Future work

The work presented in this thesis has highlighted some of the difficulties associated with atomistic material models. The most apparent problem is finding the correct balance between accuracy and computational cost. This work has also highlighted the problems associated with validating theoretically predicted values when experimentally derived values may be unavailable. It also reinforces the importance of understanding the mathematical theory behind computational tools rather than just using them as a 'black box.' Careful consideration of the theory must be followed by applying the model to simple systems before closely examining the results to validate the model. This work has shown that several methods that produce reasonable quantitative values for certain properties often struggle to reproduce accurate physical behaviour. The most important lesson that can be learnt from this work is to use caution when applying atomistic simulations when trying to calculate mechanical properties of solids. There are a number of specific results and conclusions from chapters 3, 4 and 5 that are given consideration individually in the following sections.

Atomistic finite element method

In chapter 3 a number of boron nitride nanotubes were modelled using a molecular mechanics force field, the universal force field (UFF), and an atomistic finite element method (AFEM). The AFEM method represents the BNNT with a beam model to describe the interatomic forces between bonded atoms using parameters derived from the UFF. A simple method for calculating the piezoelectric tensor entries was introduced that used atomic polarisabilities and partial atomic charges calculated using an electronegativity equalisation scheme. Results for the AFEM model were calculated using both Euler-Bernoulli and Timoshenko deep shear beams to describe the interatomic forces. Calculated values for the tensile Young's modulus and the shear modulus for the BNNTs showed that the Timoshenko beam model underestimated these properties by factors of 3 and 5 respectively. The Euler-Bernoulli beam model performed better than the Tim-

oshenko model but it also underestimated the moduli compared to the values calculated using standard molecular mechanics methods in this and other work [1, 2, 3, 4]. However, these mechanical properties are calculated based on atomic displacements so the work in chapter 3 also analysed these to study the differences between the two models. This indicated that the two methods modelled the reaction to the applied strains in significantly different ways. The piezoelectric tensor coefficients calculated with these methods varied quantitatively and the trend relating them to the chiral angle of the BNNTs when applying tensional loading was qualitatively different. These differences were shown to be related to the differences in atomic displacements between the AFEM and molecular mechanics models.

Both the mechanical and piezoelectric properties were compared against data from available literature and the UFF results compared favourably. It reproduced the mechanical properties of BNNTs seen in other work and qualitatively reproduced the trends for the piezoelectric coefficients. The coefficients showed a stronger piezoelectric effect compared to results produced using more accurate DFT calculations. This may have been due to the method used for calculating the tensor entries or it may have been due to inaccurate atomic displacements generated by the force field.

This work has shown the value of traditional molecular mechanics over the AFEM models. It has also shown that molecular mechanics can be used to predict piezoelectric properties with reasonable accuracy at a much lower computational cost compared to DFT.

Tensile mechanical bond strength

Chapter 4 examined different methods for calculating the interatomic forces between carbon atoms that are being pulled apart by an externally applied mechanical force. A variety of different methods were used to simulate the extension of carbon-carbon bonds in a selection of small hydrocarbon molecules. The methods included reactive molecular mechanics potentials (AIREBO, ReaxFF), density-functional tight-binding (DFTB3), a selection of DFT functionals (PBE, B3LYP, B2PLYPD3) and a couple of post-Hartree-Fock methods (MP2, CASSCF). Carbon-carbon bond extensions in ethene, ethane, trans-β-butene, butane, isobutene and isobutane were considered using a relaxed scanning approach. This involved changing the bond length between two carbons in a stepwise manner and freezing their nuclear coordinates, while allowing the rest of the molecule to relax at each step. From this the peak restorative force between the two carbon atoms, effectively the peak tension in the bond, and the bond length at which the peak occurred was determined. A similar process was also used to investigate fragmentation of the Clar's goblet structure in order to study these properties in polycyclic aromatic hydrocarbon molecules.

The results showed several trends. Firstly, the measured quantities were related with the bond order. Double bonds have a higher peak tension than the resonant bonds of

the Clar's goblet structure which in turn have a larger peak tension than those of single bonds. The bond lengths at which these peaks occurred showed the opposite trend with single bonds having the longest lengths at peak tension and double bonds the shortest. The peak tension values did vary from one molecule to the other regardless of bond order. The electronic structure calculations were in broad agreement on the peak tension values showing similar variations across the simulated structures. Although the set of structures was very small there was some indication that bonds involving tertiary carbon atoms are weaker than those involving secondary carbon atoms. One interesting point is that the bond lengths that correspond to the peaks were all within about 2% of each other when calculated using electronic structure methods.

The molecular mechanics results were less impressive. The ReaxFF potential predicted values for the peak tension that were at least twice the size of the electronic structure calculations. It also showed significant variation in the corresponding bond lengths for the single bonds. The mean value with this method was 1.97 ± 0.11 Å where the electronic structure methods had predicted a mean value of 1.95 ± 0.02 Å. The AIREBO potential did show consistency in the results but it did predict peak tensions $\approx 15\%$ lower than the electronic structure methods and shorter corresponding bond lengths.

The density-functional tight-binding method was applied using three different parametrisations. It was found that only one of the parameter sets was able to reproduce physically sensible behaviour over the range of bond lengths considered. This method reproduced the trends for peak tension seen in the density-functional theory and perturbation theory results and the corresponding bond lengths were also in agreement to within 2.3 %.

Overall this work highlights the difficulty in finding accurate ways to simulate bond breaking in a computationally efficient manner. Here the conclusion is that the DFTB3 method, with the appropriate parameter set (3ob), is appropriate for further investigations involving graphene nanoribbons.

Mechanical properties of graphene nanoribbons

The work in chapter 5 built upon the work in chapter 4 by using its findings regarding the applicability of computational methods to larger structures. Two methods, AIREBO and DFTB3 were used to simulate the extension to failure of a number of different graphene nanoribbon structures. The ribbons were modelled using periodic boundary conditions and were stretched by increasing the dimensions of the periodic cell. The cell length was increased in a stepwise fashion with relaxation of the nuclear coordinates at each step. The forces and stresses on the periodic cell were then used to calculate the stress in the ribbon. The simulations were performed over a large range of tensile strain values to try and capture the fragmentation of the ribbon. The importance on the length of the periodic cell was investigated to ensure that the failure mechanism of the ribbon was not affected by the number of repeats used in the cell.

Most of the ribbons failed in a catastrophic manner, breaking into two or more fragments either at or shortly after the peak stress except for the even numbered armchair nanoribbons. These ribbons generally failed in a progressive manner such that a fracture is bridged by a string of carbon atoms which grows by pulling an atom off the lattice of the larger fragment. This is associated with this type of ribbon's lack of mirror symmetry about the ribbon axis unlike the other ribbons studied. Zig-zag ribbons were shown to be stronger than armchair ribbons and also to have a greater strain at failure. The tensile mechanical strength of zig-zag ribbons was also shown to be inversely proportional to their width whereas the strength of armchair ribbons did not. An interesting result was found in the behaviour of the Young's modulus of armchair graphene nanoribbons. The ribbons can be divided into three families based on their index number and these families show different trends in their tensile moduli. These families are well known to have different band gaps. Although a relationship between the families and their moduli has been previously reported [5] the trends shown here indicate an inverse relationship between the width and the modulus, instead of the previously reported proportional relationship. This behaviour was explained by examining the electronic structure of the three families using simulated scanning tunnelling microscope images and Clar structures.
Three experimentally derived nanoribbon structures were also investigated: Chevron-type, cove-type and para-armchair graphene nanoribbons. The cove-type ribbon has a tensile strength close to that of armchair ribbons but a greater strain at failure. It is difficult to define a width for these ribbons due to the oscillating nature of the edges, which makes it difficult to define the dimensions needed to calculate strengths and moduli. However, the cove-type ribbon shows behaviour similar to zig-zag ribbons.
The failure mechanism of the chevron-type ribbon was also examined in some detail as it fails in a piecewise manner and undergoes out-of-plane buckling during this process. This leads to a highly non-linear stress-strain response albeit with a much reduced strength and initial stiffness. This behaviour could make them useful for reinforcing rubbers and some thermoplastics. The cove-type ribbons show excellent mechanical properties that could make them exceptional nanoreinforcement for most polymers.

Future work

A most important aspect of developing graphene nanoribbons for use in nanocomposites is finding strategies to disperse the ribbons evenly throughout the matrix during manufacture and to consider how the ribbons interact with the polymer matrix. Adding functional groups to the ribbons before mixing them into the polymer would improve dispersability and increase the load transfer between a polymer matrix and the ribbons. Some initial work was performed on adding functional groups to the edges on chevron-type ribbons but there was insufficient time to conclude this study. This work should be expanded to try and predict the structures that are likely to be produced during stochas-

tic functionalisation of nanoribbons. Different functional groups could be studied and the tensile strength of the bonds connecting the ribbons to the polymer determined. This would allow large and realistic models of nanocomposite materials made of nanoribbons covalently bonded into polymer networks. These models would then be able to provide insight into how to improve the design of nanocomposite materials.

Another interesting problem relates to how experimentally produced ribbons form and, most importantly, what causes them to stop growing. Most of the ribbons that have been produced using the on-surface synthesis method have finite lengths of about 30 nm. Understanding what causes the growth of these chains to stop would be highly valuable as it could provide information on how to control ribbon length. Such computational investigations could examine possible catalysts and chemical control of the environment around the ribbons with the aim of increasing ribbon length. Better theoretical understanding of the chemical reactions that occur in this process might also help in the search for better precursor molecules or molecules that could create novel shaped ribbons or nanostructures.

The mechanical strength of molecular bonds also requires further investigation. The work shown here only considered changes to bond lengths of carbon-carbon bonds and only internuclear distance was considered. This could be extended by considering different elements and by examining the effect on the mechanical strength of bonds when bond angles and dihedral torsions are also restricted. Investigating this effect may help find useful mechanically activated reaction pathways.

There is an unanswered question about the behaviour of graphene nanoribbons that is also worthy of investigation. It is widely reported, and has been seen in the results in chapter 5, that as the width of GNRs is increased their properties tend towards those of an infinite sheet of graphene. It would be interesting to investigate the transition behaviour from nanoribbon to infinite sheet given the importance of the edge shape to the electronic and mechanical properties. The length scales over which this transition occurs could be probed and the effect on the electronic properties as the ribbon index is increased to ever larger values investigated.

Finally, it would be useful to investigate bending of nanoribbons or the mechanical properties of ribbons while in a buckled state. Any long thin nanostructure is likely to become bent when mixed into a polymer and is likely to be subject to out-of-plane loads. The response of ribbons in these situations would be necessary to help predict and explain the properties of GNR reinforced polymer nanocomposites.

Closing remarks

This work has investigated the mechanical properties of nanostructures using theoretical methods. It has provided insight into the reliability of the computational methods for calculating such properties, and produced a number of new insights and predictions.

There are still many unanswered questions about these structures and their behaviour that are of interest from the view point of basic science. There is also a lot of work to be done to understand how to achieve the most efficient use of nanostructures in polymer based nanocomposites. Hopefully this work has shown the potential of graphene nanoribbons to act as a reinforcement particle in composite materials and to highlight the difficulties and limits associated with the modelling methods which can be used to simulate their behaviour.

Bibliography

[1] E. Hernández, C. Goze, P. Bernier, and A. Rubio. Elastic Properties of C and $B_xC_yN_z$ Composite Nanotubes. *Physical Review Letters*, 80(20):4502–4505, 1998.

[2] K. N. Kudin, G. E. Scuseria, and B. I. Yakobson. C_2F, BN, and C nanoshell elasticity from *ab initio* computations. *Physical Review B*, 64(23):235406, 2001.

[3] C. Li and T.-W. Chou. Static and dynamic properties of single-walled boron nitride nanotubes. *Journal of nanoscience and nanotechnology*, 6(1):54–60, 2006.

[4] V. Verma, V. K. Jindal, and K. Dharamvir. Elastic moduli of a boron nitride nanotube. *Nanotechnology*, 18(43):435711, 2007.

[5] X. Li, T.-Y. Zhang, and Y. J. Su. Periodically Modulated Size-Dependent Elastic Properties of Armchair Graphene Nanoribbons. *Nano Letters*, 15(8):4883–4888, 2015.